



**POLITECNICO**  
MILANO 1863

SCUOLA DI INGEGNERIA INDUSTRIALE  
E DELL'INFORMAZIONE

# Prompt gamma imaging with a slit camera for range monitoring in carbon ion radiation therapy: A Monte Carlo feasibility study.

TESI DI LAUREA MAGISTRALE IN  
NUCLEAR ENGINEERING - INGEGNERIA NUCLEARE

Author: **Andrea Missaglia**

Student ID: 953137

Advisor: Prof. Carlo Ettore Fiorini

Co-advisors: Aicha Bourkadi Idrissi, Francesco Casamichiela

Academic Year: 2021-22



# Abstract

Today, particle therapy (PT) has become a widely accepted and promising option for tumor treatments, next to surgery, chemotherapy, conventional radiotherapy and emerging immunotherapy.

The characteristic dose distribution, culminating at the Bragg peak, is the main advantage of charged particles over photons. However, the intrinsic precision of charged hadrons can be a double-edged sword, as particle range is not exempted from uncertainties, which are closely related to the imperfect knowledge on the patient morphology. For this reason, if the beam is not well localized, it can result in a non-effective treatment of the pathology, putting in danger nearby normal tissues, therefore making the advantageous feature of hadrontherapy not fully exploitable.

Due to range uncertainties, safety margins are taken in the treatment planning and this limits the full benefits of PT. To improve the precision and restrain the irradiation of normal tissues, range uncertainties must be reduced. Thus, efforts have been made to develop instruments with the aim to verify the particle range *in-vivo* with an ideal precision of few millimeters. Different approaches have been investigated to reduce range uncertainty through *in-vivo* range verification. They can be distinguished in direct methods, based on direct measurement of the depth-dose distribution, and indirect methods, which take advantage of the secondary emission from the patient during treatment.

There exists a correlation between the secondary emission and the depth-dose distribution, so that different techniques have been developed in order to monitor the particle range. Prompt emission of high-energy gamma-rays provides a direct and instantaneous signature of the beam range in matter. The use of prompt-gamma (PG) detection to monitor proton range has been already experimentally verified. A prompt gamma imaging (PGI) knife-edge camera, developed by IBA in collaboration with Politecnico di Milano and XGLab, has been applied for the first time clinically for a treatment of a head and neck, with measured inter-fractional global range variations in the order of  $\pm 2$  mm.

In the recent years, there has been a substantial progress in the application of PGI mostly for what concerns proton therapy. On the other hand, fewer studies have been made in the use of PGI verification within carbon ion radiation therapy (CIRT). Indeed, even if there are undoubted advantages of C-ion over proton and photon therapy, it is also true that the very same factors that make C-ions such interesting may hinder the application of PGI monitoring. For example, although C-ions have a higher yield of prompt gamma production with respect to protons, they also have a higher neutron yield. In addition to this, for ions heavier than protons, the number of incident projectiles needed to provide a given physical dose is smaller than for protons, due to the  $\frac{1}{Z^2}$  dependence of the energy loss ( $Z$  being the atomic number) and the lower multiple scattering angle of heavier ions. Moreover, the Relative Biological Effectiveness (RBE) leads to a further reduction

of the number of ions necessary to deliver the desired biological dose with higher- $Z$  ions. Therefore, the total number of generated PGs for a given pencil beam spot is lower when considering heavier ions. This strongly affects the counting statistics of PGs.

In the present work, a numerical study was conducted to explore the feasibility of using a knife-edge slit prompt-gamma camera with a beam of C-ions at clinical energies. The main goal of this work was to investigate and quantify the PG fall-off retrieval capability in CIRT with a well-established slit camera configuration, already tested clinically with proton irradiation.

The current thesis is divided in five main chapters.

Chapter 1 discusses the current state-art-of-the-art of particle therapy, considering the currently adopted particles in treatments and the ones which are supposed to have a bright future, according to literature. Moreover, the main technologies for ion acceleration are presented. Lastly, the Physics models on the interaction between charged hadrons and matter are revised, along with a section concerning radiation detection.

Chapter 2 includes more specific topics to the problem faced in this thesis work. A review of the most promising range verification methods are outlined, giving the preference to the family of techniques to which the one chosen for this work belongs. From the sources of range uncertainty, which is first cause moving this thesis, I will come to needs and challenges in prompt gamma monitoring.

Chapter 3, the heart of the present work, includes, based on Monte Carlo simulations, a preliminary study on secondary emission from an irradiated target and a detailed study on the feasibility to apply the prompt gamma imaging technique in carbon ion radiation therapy.

Chapter 4 will briefly describe the electronics design of a platform that will be part of the experimental set-up, trying to prove the results obtained in chapter three. Finally, Chapter 5 includes conclusions and future developments for the topics treated in this thesis.

**Keywords:** Prompt gamma imaging, carbon ions, feasibility study, Monte Carlo simulations, slit camera, electronics readout

## Abstract in lingua italiana

Negli ultimi decenni, la terapia particellare è diventata un'opzione ampiamente accettata e promettente per trattamenti tumorali, accanto alla chirurgia, alla chemioterapia, alla radioterapia convenzionale e all'emergente immunoterapia.

La caratteristica distribuzione di dose, che culmina con il picco di Bragg, è il principale vantaggio delle particelle cariche rispetto ai fotoni. Tuttavia, la precisione intrinseca degli adroni carichi può essere un'arma a doppio taglio, poiché il range delle particelle usate nei trattamenti non è esente da incertezze, strettamente correlate alla conoscenza imperfetta della morfologia del paziente. Per questo motivo, se il fascio non è ben localizzato, il trattamento potrebbe non essere efficace, mettendo in pericolo i tessuti sani vicini alla zona tumorale perdendo, dunque, la caratteristica vantaggiosa degli adroni carichi.

A causa delle incertezze sul range, tipici margini di sicurezza sono considerati nella pianificazione del trattamento, limitando i benefici della terapia. Per migliorare la precisione e ridurre l'irraggiamento dei tessuti sani, numerose sforzi sono stati compiuti nel sviluppare strumenti con l'obiettivo di verificare *in-vivo* il range delle particelle di trattamento con una precisione ideale di pochi millimetri. I diversi approcci studiati possono essere distinti in metodi diretti, basati sulla misura della distribuzione della curva profondità-dose, e metodi indiretti, che sfruttano l'emissione secondaria dal paziente durante il trattamento. Esiste una correlazione tra l'emissione gamma secondaria e la distribuzione profondità-dose, che ha dato il via allo sviluppo di diverse tecniche per monitorare il range. L'emissione di raggi gamma ad alta energia fornisce una firma diretta e istantanea sulla profondità raggiunta dal fascio nella materia. L'uso della rivelazione di gamma pronti per monitorare il range di protoni è già stato verificato sperimentalmente. Un camera a knife-edge, sviluppata da IBA in collaborazione con il Politecnico di Milano e XGLab, è stata applicata per la prima volta in sede clinica per il trattamento di un tumore alla testa e al collo, con variazioni del range globale per un frazione di dose nell'ordine di 2mm.

Negli ultimi anni si è registrato un notevole progresso nell'applicazione del prompt gamma imaging soprattutto per quanto riguarda la terapia protonica. D'altra parte, sono stati effettuati meno studi nell'uso della stessa tecnica nell'ambito della radioterapia con ioni carbonio (CIRT). Infatti, anche se ci sono indubbi vantaggi di questi ioni rispetto a protoni e fotoni, è anche vero che gli stessi fattori che rendono gli ioni carbonio così interessanti ostacolano l'applicazione del monitoraggio attraverso imaging di gamma pronti. Ad esempio, anche se gli ioni C hanno un resa di produzione gamma più elevata rispetto ai protoni, hanno anche un resa neutronica più elevata. Inoltre, per ioni pesanti, il numero di particelle incidenti necessari per fornire una data dose è più piccolo che per protoni, a causa della dipendenza  $\frac{1}{Z^2}$  della perdita di energia (dove Z è il numero atomico) e dell'angolo di scattering multiplo inferiore per ioni più pesanti. Inoltre, all'aumentare del numero atomico, l'efficacia biologica relativa (RBE) porta ad un'ulteriore riduzione del numero

di ioni necessari a rilasciare la dose biologica desiderata. Pertanto, il numero totale di gamma pronti generati per un dato pencil beam spot è inferiore se si considera ioni più pesanti. Ciò influisce fortemente sulla statistica di conteggio dei gamma pronti.

In questo lavoro di tesi, uno studio numerico è stato condotto per esplorare la possibilità di usare una camera per la rivelazione di gamma pronti a seguito dell'irraggiamento con ioni carbonio ad energie cliniche. L'obiettivo principale era investigare la capacità di ricavare e quantificare variazione del range nella CIRT, utilizzando una camera a configurazione knife-edge, simile a quella già testata clinicamente per protoni.

La seguente tesi è divisa in cinque capitoli.

Il primo capitolo illustra l'attuale stato dell'arte della terapia particellare, considerando le particelle attualmente adottate nei trattamenti e quelle che si suppone abbiano un futuro brillante, secondo la letteratura scientifica. Vengono inoltre presentate le principali tecnologie per l'accelerazione di ioni. Infine, i modelli di fisici sull'interazione tra adroni carichi e materia sono riportati, insieme ad una sezione riguardante la rivelazione di radiazioni.

Il capitolo include argomenti più specifici sul problema affrontato in questo lavoro di tesi. Viene delineata una rassegna dei più promettenti metodi di verifica del range, dando la precedenza alla famiglia di tecniche a cui appartiene quella scelta per questo lavoro. Dalle sorgenti di incertezza, che è la prima causa che muove questa tesi, si considerano le esigenze e le sfide nel monitoraggio di gamma pronti.

Il capitolo 3, cuore di questo lavoro, comprende, sulla base delle simulazioni Monte Carlo, uno studio preliminare sull'emissione secondaria a seguito dell'irraggiamento di un target e uno studio dettagliato sulla fattibilità di applicare la tecnica di prompt gamma imaging nella radioterapia con ioni carbonio.

Il capitolo 4 descriverà brevemente la progettazione di una piattaforma elettronica che farà parte del set-up sperimentale per dimostrare i risultati ottenuti nel terzo capitolo. Infine, il capitolo 5 include conclusioni dei risultati ottenuti e sviluppi futuri che sono il naturale continuo di questo lavoro di tesi.

**Parole chiave:** Prompt gamma imaging, ioni carbonio, studio di fattibilità, simulazioni Monte Carlo, gamma camera, elettronica di lettura

# Contents

<b>Abstract</b>	<b>i</b>
<b>Abstract in lingua italiana</b>	<b>v</b>
<b>Contents</b>	<b>ix</b>
<b>1 Particle therapy</b>	<b>1</b>
1.1 Introduction . . . . .	1
1.1.1 Cancer and the role of particle therapy . . . . .	1
1.1.2 From Bragg discovery to therapy centers: Historic excursus . . . . .	4
1.1.3 Carbon ion radiation therapy . . . . .	5
1.2 From therapy particles to beam delivery systems . . . . .	8
1.2.1 Particles used in therapy . . . . .	8
1.2.2 Particle acceleration . . . . .	11
1.3 Beam delivery system . . . . .	17
1.4 Physics of the interaction between particles and matter . . . . .	18
1.4.1 Interaction of charged hadrons . . . . .	19
1.4.2 The origin of prompt gamma rays . . . . .	24
1.4.3 Interaction of electromagnetic radiation with matter . . . . .	32
1.5 Radiation detection . . . . .	35
1.5.1 Inorganic scintillators: LYSO . . . . .	36
1.5.2 Silicon photomultipliers . . . . .	38
<b>2 Range uncertainties in particle therapy</b>	<b>43</b>
2.1 Introduction . . . . .	43
2.1.1 Definition of range . . . . .	44
2.1.2 Sources of uncertainty . . . . .	44
2.1.3 Range uncertainty influence on particle therapy . . . . .	45
2.2 Range Verification methods . . . . .	47

2.2.1	Pre-treatment reduction of uncertainties . . . . .	47
2.2.2	Real-time treatment monitoring methods . . . . .	49
2.2.3	Post treatment verification methods . . . . .	53
2.3	Prompt-gamma monitoring in charged particle therapy . . . . .	56
2.3.1	Prompt gamma techniques . . . . .	56
2.3.2	Detection camera prototypes . . . . .	62
2.3.3	Needs and challenges . . . . .	66
<b>3</b>	<b>Monte Carlo feasibility study of a prompt gamma slit camera in carbon ion therapy</b>	<b>69</b>
3.1	Introduction . . . . .	69
3.1.1	The transport problem . . . . .	69
3.1.2	Steps in Monte Carlo methods . . . . .	70
3.2	Secondary emission from an irradiated phantom: A preliminary study . . .	71
3.2.1	Methods and materials . . . . .	71
3.2.2	Results and Discussion . . . . .	72
3.3	Feasibility study on the application of PGI technique in CIRT . . . . .	75
3.3.1	Reasons . . . . .	78
3.3.2	Methods . . . . .	79
3.3.3	Results . . . . .	88
<b>4</b>	<b>Proposal of an experimental set-up for future measurements</b>	<b>99</b>
4.1	The experimental set-up . . . . .	99
4.1.1	The architecture of the detection system . . . . .	100
4.2	Design of the front end PCB . . . . .	103
4.2.1	Analog signal path . . . . .	104
4.2.2	Trigger lines . . . . .	109
<b>5</b>	<b>Conclusions and future developments</b>	<b>111</b>
5.1	Conclusions . . . . .	111
5.1.1	Summary . . . . .	111
5.1.2	Final discussion on the obtained results . . . . .	112
5.2	Future developments . . . . .	113
	<b>Bibliography</b>	<b>115</b>

<b>List of Figures</b>	<b>129</b>
<b>List of Tables</b>	<b>137</b>
<b>Acknowledgements</b>	<b>139</b>



# 1 | Particle therapy

*Chapter One will start from the cause which started the workflow of particle therapy: the burden of cancer. The historic reasons that brought to the present status of particle therapy will be discussed. This thesis will focus on carbon ions and how to reduce their range uncertainties; hence, carbon ion radiation therapy (CIRT) will be treated in detail. I will introduce the main challenges in particle therapy and the state-of-the-art in CIRT.*

*The next section will be devoted to already used and most promising particles used in hadrontherapy: I will distinguish them from a physical, radio-biological standpoint, comparing the protons and carbon ions to the new ions under investigation.*

*Then, the acceleration of ions will be considered: requirements and different types of accelerators will be treated.*

*I will also face the Physics of the interaction between particles and matter. The main model describing the behaviour of charged hadrons in materials will be presented. I will direct the discussion on how prompt gammas are born in matter and how this is correlated to particle therapy. There will be also a small introduction to interaction of electromagnetic radiation, which is of great important when considering a detection system.*

*The last section will be focused on radiation detection. In particular, I will generally consider the scintillation detectors and, then, I will describe cerium-doped lutetium orthosilicate  $\text{Lu}_{2-x}\text{Y}_x\text{SiO}_5:\text{Ce}$  (LYSO:Ce), which is an important part of the feasibility study conducted in this thesis. For the same reason, the silicon photomultipliers will be introduced, and the main figure of merits described.*

## 1.1. Introduction

### 1.1.1. Cancer and the role of particle therapy

Cancer is a disease in which some of the body's cells grow uncontrollably and spread to other regions of the human body. Ordinarily, human cells grow and multiply through a process called "cell division". When cells grow old or become damaged, they die, and new cells take their place. Anyway, sometimes, this orderly process breaks down, and

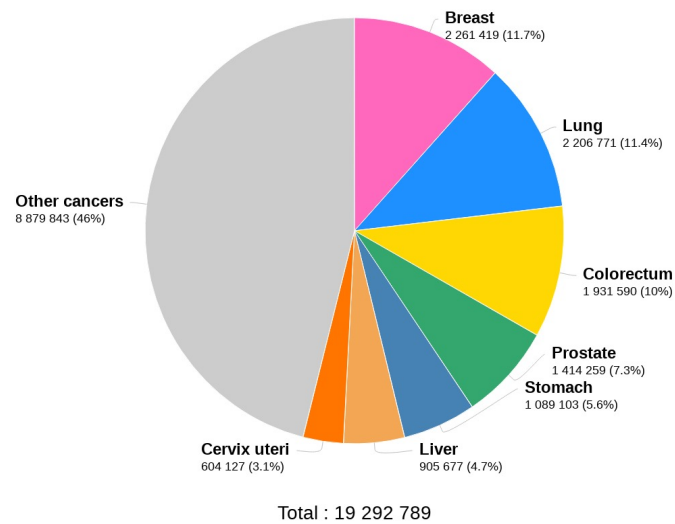
abnormal or damaged cells grow and multiply. This may happen almost anywhere in the human body and may form tumors, which are lumps of tissue that can be cancerous or not cancerous (also said "benign"). Cancerous tumors spread into, or invade, nearby tissues, travelling to distant places in the body to form new cancerous sites, following a process called "metastasis".

Today, cancer is a leading cause of death worldwide, accounting for nearly 10 million deaths in 2020, or nearly one in six deaths. The most common types are breast, lung, colon and rectum and prostate cancers; among them, lung cancer is the most dangerous one (see Figure 1.1(b)).

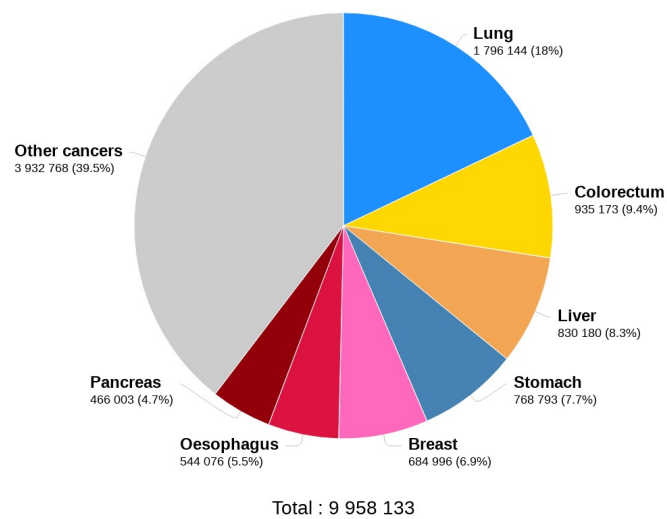
Among the different techniques that can be adopted to fight cancer back, radiotherapy is an essential component next to surgery, chemotherapy, and the emerging immunotherapy. Radiation oncologists can use either photons (X-rays) produced by means of linear electron accelerators (linacs), or charged particles, which include protons and heavy ions (typically carbon ions). Approximately, out of the two-thirds of patients affected by cancer, under treatment with radiotherapy, more than 80% receive X-rays and only about 0.8% undergo radiation from high-energy charged particles [24]. Anyway, interest in new radiotherapeutic techniques has recently risen to minimize dose deposition in proximal normal structures of the target, with the goal of reducing acute and late adverse effects of treatment: particle therapy with protons and heavy ions meets such criteria.

The dose deposition of carbon-ion beam, for instance, is low in the proximal region where the normal tissue is exposed, but greatly enhanced at the end of their range where the tumor is located and drops to near zero abruptly thereafter. The greater ionizing density of charged hadrons induces within the targeted neoplasm a higher degree of irreversible DNA lesions, which overwhelms cancer cells' repair capacity. The relative biologic effectiveness (RBE) concept has been introduced to account for this increased efficiency of cell killing over photon therapy. At clinical institutions, an RBE value of 1.1 to 1.2 has been documented for proton therapy, while the RBE distribution for the heavier carbon ions in the targeted tissues varies between 2 and 5. The direct-killing effect of heavy ions maintains their ability to kill malignant cells irrespective of oxygen concentration. Therefore, even hypoxic tumor tissues are significantly sensitive to carbon ion therapy [71].

To sum up, charged particle therapy (CPT) is a radiotherapy modality showing promising results, which could be a powerful weapon to tackle the burden of cancer.



(a)



(b)

Figure 1.1: (a) Estimated number of new cases in 2020, worldwide, both sexes, all ages.;  
 (b) Estimated number of deaths in 2020, worldwide, both sexes, all ages.

### 1.1.2. From Bragg discovery to therapy centers: Historic excursus

It all began when Sir William Henry Bragg discovered a phenomenon in which a charged particle released most of the energy at the end of its range, producing, in the depth-dose curve along the beam direction in a medium, a prominent peak, which was then called the "Bragg peak" (BP) [11]. Some years later, in 1946, Robert R. Wilson identified the clinical significance of the BP for the treatment of cancer: custom dose distributions could be generated to locate energy depositions within the tumor volume while sparing normal tissues. He suggested the clinical use of protons and heavy ions for cancer treatment, also proposing a method to cover the entire volume of tumors by stacking multiple pristine Bragg peaks, what today is called "spread-out Bragg peak" (SOBP) [131]. Prior to Wilson's proposal, Ernest O. Lawrence developed the first cyclotron at the University of California Lawrence Berkeley Laboratory (LBL) in 1930. Later, Cornelius A. Tobias and John H. Lawrence carried out the first use of proton beams for the treatment of human patients and obtained favorable results in 1954, validating Wilson's proposal by using the 184-inch cyclotron [113].

In the late 1950s, Larsson and Leksell developed radio surgical techniques using proton beams to treat brain tumors from the Gustaf Werner Institute cyclotron (Uppsala, Sweden) [65]. Not only that, but they were also the first to adopt range modulation along the beam direction to generate SOBP and to use beam scanning to cover the tumor volumes in the lateral direction. Having shown the superior characteristics for clinical radiation therapy of protons, which resulted to be good candidates of oncology's historic search for an optimum dose distribution, a complete facility for clinical proton radiation therapy was designed for and built at Loma Linda University Medical Center, which began clinical operations in October 1990.

The LBL group started a heavy-ion therapy program with the BEVELAC accelerator in 1975 [15] and the first helium-ion radiotherapy, carbon-ion radiotherapy (CIRT), neon-ion radiotherapy, argon-ion radiotherapy, and silicon-ion radiotherapy were carried out in 1975, 1977, 1977, 1979, and 1982, respectively [101] [12].

In 1994, the first dedicated medical facility for heavy-ion radiotherapy in the world was established in Japan, which was the Heavy Ion Medical Accelerator in Chiba (HIMAC) at the National Institute of Radiological Sciences (NIRS), which is now called the National Institute for Quantum and Radiological Science and Technology (QST/NIRS) [80] [50]. Based on extensive studies to optimize the ion species for heavy-ion radiotherapy, the NIRS chose carbon ions, because showed optimal RBE and optimal oxygen enhancement ratio (OER) [50]. For effective radiotherapy, high RBE and close to one OER are typically

preferred [122]. Heavier ions have higher linear energy transfers (LETs) across the BP than lighter ions [62]. However, for very large particles, such as argon, the increase in LET occurs in the plateau region of the beam path, not only at the BP, which results in excessive normal-tissue damage. Carbon ions, instead, show a favorable peak-to-plateau ratio showing the maximum RBE at the Bragg peak region [1].

After the HIMAC, the Hyogo Ion Beam Medical Center (HIBMC) adopted CIRT as well as PBT in Japan in 2002 [122]. In 2003, CIRT was approved as an advanced medical technology by the Japanese government; therefore, carbon ion facilities have received reimbursement since 2003 [80]. In 2010, the NIRS collaborated with Gunma University to develop a compact synchrotron with a diameter approximately half that of the synchrotron of the HIMAC ( $\approx 20m$  vs.  $\approx 40m$ ) [80]. By reducing the building size, the cost of establishing a CIRT facility could be reduced significantly. In 2013, the SAGA Heavy Ion Medical Accelerator in Tosu (SAGA-HIMAT) decided to start CIRT, and in 2015, the same was done by the Kanagawa Cancer Center in Japan [122].

In Europe, the Gesellschaft für Schwerionenforschung (GSI) in Germany adopted CIRT in 1997. In contrast to the NIRS, the GSI developed and employed the pencil-beam scanning technique, instead of the passive beam irradiation with SOBPs for beam delivery [61]. In 2009, the clinical service with carbon-ion beams provided by the GSI was succeeded by the Heidelberg Ion-Beam Therapy Center (HIT), which is the first hospital-based particle-therapy facility in the world treating patients with proton and carbon-ion beams, using the pencil-beam scanning technique [17]. In 2012, the Centro Nazionale di Adronterapia Oncologica (CNAO) in Italy started patient treatment with carbon-ion beams [122]. Since 2012, many other CIRT therapy centers have been started: up to now, more than a hundred facilities all over the world can provide beams of protons, carbon, or other ions for clinical treatments [90] and tens of therapy centers are under construction [89].

### 1.1.3. Carbon ion radiation therapy

#### Challenges in charged particle therapy

CPT has an essential prospective role in fighting the growing burden of cancer on a global scale, and its impact could be significant [10]. Anyway, its full potential is yet to be realized and improvements are needed following two main drivers: enhancement of efficacy and decrease of costs.

CPT offers benefits over and above standard radiotherapy for palliative or curative treatments, offering not just physical dose escalation but also biological advantage. Yet in terms of efficacy, it is not possible to capitalize fully on increased radiobiological effectiveness of charged particles at present, primarily due to limitations in knowledge. To fill this

gap, existing programmes of research are investigating the underlying mechanisms of CPT in terms of fundamental chemical, biological and cellular processes to try to understand the roles of these processes in determining clinical outcomes. A second reason the efficacy of CPT is not yet fully exploited is due to technological limitations. Advanced techniques and technological improvements for CPT seek to deliver higher quality treatments with increased conformity as these translate to long-term benefits. However, some of these improvements would increase the cost of the treatment [138].

In terms of cost (or efficiency) the gap between conventional X-ray photon radiotherapy and CPT still exists due to the many challenges to be addressed: affordability, complexity and limitations with current technology all restrict the utility of CPT. Developments in accelerators and related technologies, beam delivery methods, verification tools, and increased clinical experience have seen growth in the number of facilities. Although availability has surged in recent years with several vendors offering competitive and commercial turn-key solutions, high capital and operational costs are still a primary issue [138].

To conclude, the primary hurdle with CPT remains a question of cost; its availability and accessibility is still driven by the balance between cost and benefit: progressive improvements will contribute to decrease the cost, but future growth will depend on the extent of benefit [69] [138].

## State of the art

Radiation therapy is one of the most widely used therapies for malignancies. The therapeutic use of heavy ions, such as carbon ions, has gained significant interest due to advantageous physical and radiobiologic properties compared to photon-based therapy. The National Institute of Radiologic Sciences (NIRS) opened the first heavy ion accelerator for clinical use in Chiba, Japan, in 1994 [49]. Since that time, over 20,000 patients have been treated with CIRT [66]. Today, there are a total of 13 centers treating with CIRT from all around the world distributed in five countries [90]. At NIRS, 22% of patients treated have had localized prostate cancer, with other common sites including bone and soft tissue (13%) and head and neck (11%) [50]. To date, carbon ion radiotherapy has been studied for almost every type of malignancy, including intracranial malignancies, head and neck malignancies, primary and metastatic lung cancers, tumors of the gastrointestinal tract, prostate and genitourinary cancers, sarcomas, cutaneous malignancies, breast cancer, gynecologic malignancies, and pediatric cancers. Additionally, carbon ion radiotherapy has been studied extensively in the setting of recurrent disease. Malouff *et al.* provided a comprehensive review of the studies of each of these disease sites, with a focus on the current trials using carbon ion radiotherapy [74].

Nowadays, centers treating with CIRT can take advantage of two types of treatment techniques to help conform the dose distribution to minimize dose to OARs. Like proton therapy, CIRT can be delivered either through passive scattering, using a collimator to shape the beam in the lateral direction and a range compensator to shape the beam distally; or through active scanning, using a narrow “pencil beam” avoiding the use of a collimator or compensator [123]. Notably, use of active scanning, along with the physical properties of the Bragg Peak and a slower treatment time, may lead to higher uncertainty due to physiologic motion.

This introduces the first crucial point: one of the major concerns regarding CIRT, and heavy ion radiotherapy in general, is dose uncertainty. With the Bragg-Peak and sharp lateral penumbra, there is a higher susceptibility to intrafraction motion compared to photon-based therapy, where the effect of motion can be mitigated due to the “dose bath.” Further, there is higher likelihood that the Bragg-Peak may be in normal tissues with intrafraction motion. Additionally, CIRT exhibits a fragmentation tail, where nuclear fragments contribute to an unwanted dose distal to the target, bringing to a greater degree of uncertainty. The second main drawback is the cost of developing and maintaining a heavy-ion center. For instance, Pompos *et al.* estimates that the cost of developing a center with capacity of 1,000 patients per year is roughly twice as expensive as a proton center of the same size [98]. The estimated cost for multiple room centers treating with multiple ions is around 200 million dollars [24]. Much of this cost comes from the complexity of the system, such as the need for a synchrotron and additional shielding. Due to the size and expense associated to CIRT, most of centers are treating exploiting fixed-beam gantries, to limit the treatment positions available. Currently, there are two centers adopting rotating gantries with the ability to irradiate from all angles [100].

Finally, based on the present state-of-the-art, heavy ion therapy is at a sensitive point: it has an enormous potential due to physical and biological properties, but its clinical advantage compared with protons and X-rays, which are both cheaper and smaller technologies, remains to be demonstrated. However, outstanding results have been found in gastrointestinal cancers, sarcomas, and nasopharyngeal carcinomas, but randomized clinical trials are ongoing. At the same time, research must continue to make the therapy cheaper and more effective. From a technological standpoint, it is particularly important to build smaller and cheaper accelerators and beam delivery systems, exploiting superconducting magnets and gantry-less systems. For what concern Biology, it is essential to assess the combination of heavy ions with molecular therapy and immunotherapy, in comparison with X-rays and protons. In clinical research, it is necessary to test hypofractionated regimes, combined protocols and to fully exploit the putative advantages by increasing the LET in the tumor, which can require multi-ion irradiation. Therefore, rather than

a single silver bullet, in the future, a combination of projectiles may become common to sterilize aggressive, radioresistant malignancies.

## 1.2. From therapy particles to beam delivery systems

### 1.2.1. Particles used in therapy

Since the early days of radiation therapy, a fundamental research driver has been the achievement of improved dose distributions (i.e., high dose to target volume, dose as low as possible to healthy tissues), enhancing at the same time, as much as possible, the selectivity in biological effectiveness, hence boosting the therapeutic ratio. The idea of Robert Wilson to use charged particles for cancer treatment presented accelerated ion beams as natural candidates to improve dose conformity through the BP. Not only that, but it was also soon evident that the physics of radiation-matter interaction would have offered the possibility of coupling the spatial selectivity of charged particles with enhanced biological effectiveness. Indeed, after preliminary radiobiological experiments had confirmed these hypotheses, the development and diffusion of CPT started. According to recently published statistics, there has been a continuous increase in the number of patients treated with charged particles, as shown in Figure 1.2. By the end of 2020 more than 290000 patients have been treated worldwide with Particle Therapy, close to 250.000 with protons, close to 40000 with C-ions and about 3.500 with He, pions and with other ions.

So far, proton has been the most frequently used charged particle, so that proton therapy has acquired the largest clinical experience. This is not casual. Infact, despite the physical properties offered by heavier ions, the biological effectiveness of, for instance, carbon ions is offset by large uncertainties and this is a serious concern for clinicians.

### New ions

In recent years, an intense discussion about the possibility of optimizing the clinical potential of CPT by extending the spectrum of therapeutic ions beyond protons and carbon ions has arisen in the literature. While this was hindered in the past by technical issues, it is now possible to study and better exploit the peculiarities of different ion species [121]. For instance, helium and lithium ions have been proposed considering their improved lateral dose distributions compared with protons; at the same time, they have a lower RBE than that of carbon, and thus, they are easier to be adopted for clinical use.

The possible use of helium ions in hadrontherapy has recently gained more attention. Due

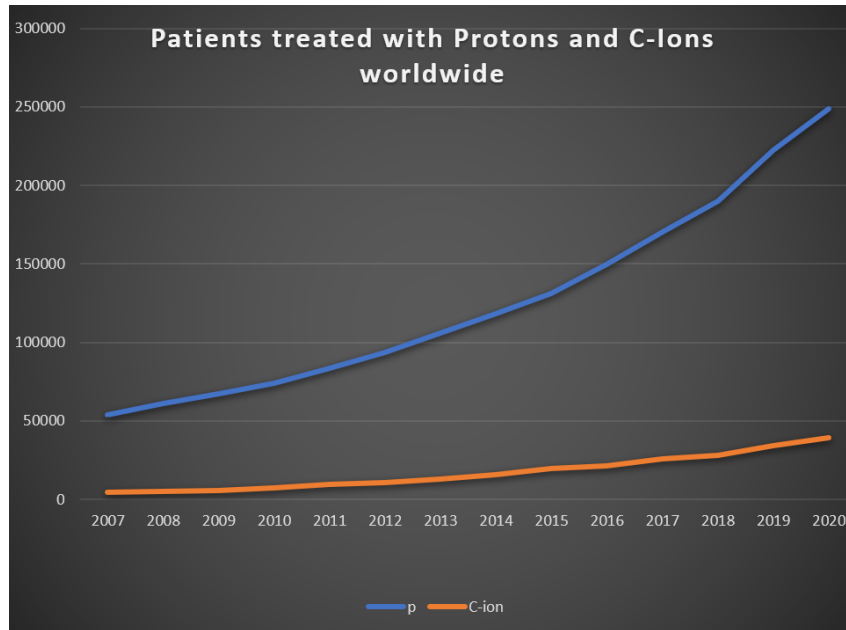


Figure 1.2: Statistics of patients treated in particle therapy facilities worldwide: in 2020, around 250.000 patients were treated with protons and close to 40000 with C-ions.

to its intermediate physical and radio-biological properties between proton and carbon ion beams [117], helium ions may provide a streamlined economic steppingstone towards an era of widespread use of different particle approaches to light and heavy ion therapy. With respect to the clinical proton beams, helium ions exhibit superior physical properties such as reduced lateral scattering and range straggling with higher RBE and LET ranging from  $\sim 4 \frac{\text{keV}}{\mu\text{m}}$  to  $\sim 40 \frac{\text{keV}}{\mu\text{m}}$ . In the frame of heavy ion therapy using carbon, oxygen or neon ions, where LET increases beyond  $100 \frac{\text{keV}}{\mu\text{m}}$ , helium ions exhibit similar physical attributes such as a sharp lateral penumbra, however, with reduced biological uncertainties and without potentially spoiling dose distributions due to excess fragmentation of heavier ion beams, particularly for higher penetration depths. This could make easier to adopt helium ions for clinical use. For a complete roadmap which presents an overview of the current state-of-the-art and future directions of helium ion therapy see Ref. [73].

Oxygen is also considered a good candidate [109] [3]: compared to carbon ions, oxygen ions offer a further reduced lateral scattering, which contributes favorably to the tumor conformity, and a higher linear energy transfer, which might be of special interest for the treatment of radio-resistant tumors, like Osteosarcomas. The high LET of oxygen ions, associated with higher RBE than carbon ions, translates to better treatment effectiveness when treating hypoxic tumors [108] [3]. On the other hand, nuclear fragmentation is more pronounced for oxygen ions due to the overall higher inelastic cross sections in nuclear interactions, bringing to a deeper decrease of the ion fluence and an enhanced

fragmentation dose beyond the Bragg peak in comparison to carbon ions [106].

Kurz *et al.* published the results of the first experimental-based study of an oxygen ion beam in 2012. They measured the depth-dose distributions of oxygen ions beams at the HIT. Their work contributed to the development of a pre-clinical oxygen ion-beam experimental database, which is already used in research purpose treatment planning systems to support radiobiological experiments with oxygen ion beams at HIT [139].

## Comparison studies of therapy particles

Many comparison studies were conducted about about different types of particles that can be considered for CPT.

Yu-Shen Lin *et al.* showed that  $^{12}\text{C}$  beam had the narrowest longitudinal and lateral dose profiles and the highest RBE values, followed by  $^4\text{He}$  and  $^1\text{H}$  beams. It was also found that smaller differences in these comparisons were found between  $^4\text{He}$  and  $^{12}\text{C}$  than those between  $^1\text{H}$  and  $^4\text{He}$ , which indicates that  $^4\text{He}$  beam is also a promising option for cancer therapy [68].

Mattei *et al.* studied the prompt gamma-ray emission by the interaction of helium, carbon, and oxygen ion beams from a polymethyl methacrylate phantom (PMMA) [75]. In their work, it is found that  $^4\text{He}$  and  $^{16}\text{O}$  beams, whose prompt-gamma production was measured for the first time, were particularly relevant for future CPT applications: results proved non-negligible prompt photon production in the interactions of  $^4\text{He}$  and  $^{16}\text{O}$  beams of therapeutic energy with a PMMA target. Moreover, the measured yields were used to compute the expected resolution in the beam range of a typical treatment scenario, assuming the performance of the IBA slit camera documented in Smeets *et al.* [112]. Resolutions below  $2\div 3$  mm were obtained in all the different scenarios, supporting the feasibility of a PG-based range monitoring approach using  $^4\text{He}$ ,  $^{12}\text{C}$  or  $^{16}\text{O}$  particle beams. Lastly, Burigo *et al.* compared the dose distributions and cell survival fractions for different ion beams, using Monte Carlo simulations and the Microdosimetric Kinetic model. One of the main challenges of ion therapy is the limitation of side effects related to damage of healthy tissues surrounding cancer volume. The comparison of the impact of  $^1\text{H}$ ,  $^4\text{He}$ ,  $^{12}\text{C}$  and  $^{16}\text{O}$  SOBPs on healthy tissues in front of and behind the tumor in all these cases led the authors to multiple conclusions that can be summarized in: the optimal ion beam depends on the location of the tumor and on the radio-sensitivity of tissues under irradiation [14].

## Multi-ion treatment

Even using ions heavier than carbon, it is challenging to deliver a high-LET treatment to the entire tumor volume and only a relatively little tumor fraction is exposed to high LET radiation.

Approaches to extend the high-LET regions with a single ion are hindered by increasing toxicity. However, when multiple ions (from light to heavy) are used, it is possible to increase the LET in the target region while maintaining a low toxicity in the normal tissue [25]. A combination of proton, helium, carbon, and oxygen beams, produced from a single synchrotron, may be provided to reach the goal LET distribution to the tumor volume, exploiting the method known as "intensity-modulated composite particle therapy". This method requires a multi-ion source synchrotron, like those available at the HIT or NIRS. In addition, it would be necessary to implement a careful multi-angle dose simulation and verification system, along with a fast switching among the different ion sources. For applications to hypoxic tumors, multi-ion therapy could be a useful weapon, since it can optimally increase the LET (decreasing the OER), or the dose in the low-oxygen sub-volumes, resulting in highly effective treatments.

Finally, multi-ion therapy has several technical challenges which will be faced in future, but the goal of increasing the LET in the tumor volume makes it a possible optimization of heavy ion therapy.

### 1.2.2. Particle acceleration

In the last decades, hadrontherapy has made great advances passing from a stage of pure research to a well-established treatment modality for solid tumors. The history of hadrontherapy accelerators is strictly related to the development of therapy itself, starting from the first cyclotrons used in the thirties for neutron therapy, moving to more modern and flexible machines used nowadays (for an exhaustive review, see Ref. [21]).

## Requirements

Introducing the problem of acceleration of particles, there are requirements dictated by clinical treatment. Heavier ions and other species such as pions can give rise to a greater RBE due in part to their higher LET. But their higher mass and charge means that substantially higher incident energies are required for the same treatment depths in patients, necessitating larger accelerator equipment. Moreover, the planning treatment volume (PTV) into which the dose must be administered places an additional requirement on the accelerator: the larger the volume, the larger the number of particles that must be

delivered. If the depth range of the PTV is, for instance, 10÷20 cm then it may be covered by varying the incident particle energy such that the Bragg peaks for each energy occur at different depths. This is the concept of the SOBP and may be achieved either by interposing a suitable varying-thickness modulator wheel [58], or by adjusting the particle energy in discrete steps by some other means. The latter method constitutes the burgeoning method of spot scanning which is replacing the previous passive spreading methods for a more efficient coverage of PTV.

As well as the current and energy requirements one must also consider the requirements on the transverse beam size and energy spread. As any heavy charged species such as a proton traverses a solid material, it scatters and loses energy with statistical fluctuations. The primary ionisation energy loss gives rise to a straggling of the range; the Bragg peak has a finite width which to a good approximation is about 1.1% of the range, in other words about 1÷2 mm [86]. There is little point therefore in having a very small initial energy spread as it will be smeared out by the straggling, and so a 0.4% energy spread is generally adequate. Similarly, multiple Coulomb scattering will spread the protons out transversely, and again an initial incident spot size of a few millimeters is adequate. These beam specifications are readily achieved by conventional accelerator technology [16] [31]. The final requirement is to be able to vary the direction from which the administered dose is delivered to the patient. In a very limited set of cases, patients themselves may be moved somewhat, but in most treatments the patient is supine, and the incident particles must be directed from a variety of angles; this is done primarily to avoid dose to critical structures but also to spread out the proximal dose. In this regard, the gantries used in charged particle therapy serve a similar purpose to the smaller rotating electron linacs that deliver photons for intensity-modulated radiotherapy. The most-used method of achieving a varying field angle is to utilise a so-called "isocentric gantry", where the beam is rotated around a stationary patient; this is shown schematically in Figure 1.3. Whilst a full 360° of rotation means the patient would not have to rotate, recently it has also been proposed to combine a narrower range of gantry rotation angles (around 180°) with patient table rotation; the rationale for this is to restrict the floor area required for each treatment room.

Gantries may be used for heavier ions than protons, but, as those species become heavier, the magnetic fields required to deflect them increase accordingly. The stiffness of the ion beam is described by its magnetic rigidity,  $B\rho = \frac{p}{q}$ , where the particle momentum,  $p$ , and charge,  $q$ , determine the trade-off between magnetic field,  $B$ , and resultant bending radius  $\rho$ . It is worth to notice that 1.8T is about the largest field available from a resistive (normal conducting) magnet, leading to a bending radius of 1.35m.

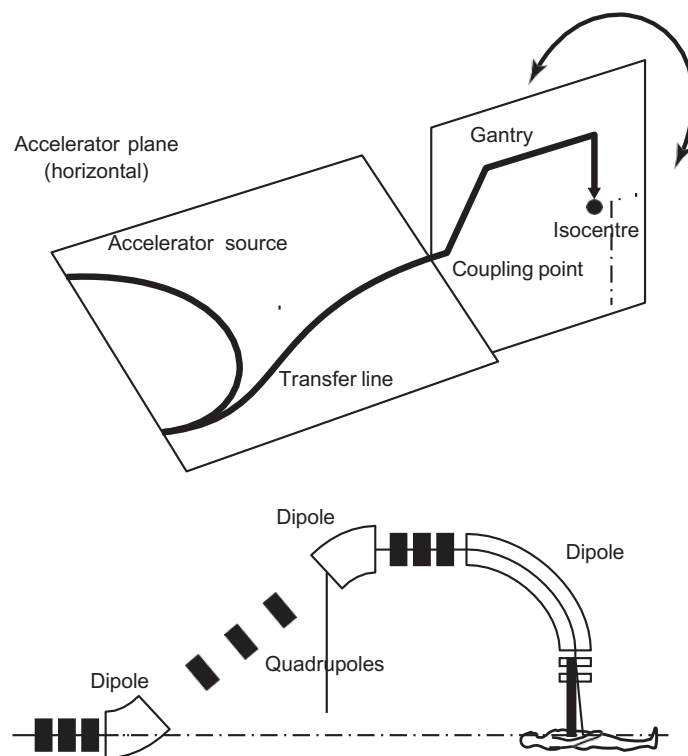


Figure 1.3: Schematic illustration of a charged particle therapy facility with isocentric gantry. The gantry consists of a number of dipole and quadrupole magnets that all rotate around the patient; in this example the magnets that scan the spots across the treatment field are located downstream of the final dipole, which is often but not always what is implemented. Figure from Ref. [86].

The only carbon-ion gantry currently in operation is at the Heidelberg Ion Beam Therapy Center (HIT), where the maximum carbon-ion energy of  $425 \frac{\text{MeV}}{u}$  corresponds to a magnetic rigidity of 6.57 Tm; the bend radius in their normal-conducting magnets is thus nearly three times as large (3.65m), and to make it smaller requires the use of superconducting magnets that may deliver a larger magnetic field [86]. To conclude, a treatment facility consists of an accelerator source and at least one treatment room, and in most implementations today several treatment rooms are fed from a single accelerator source, physically connected by a beam transport system that can direct the protons or heavier ions into each treatment room. Since a treatment room only need take beam for a small fraction of the time the patient is there (most of the time is spent for patient positioning and verification) it is suitably efficient to switch a single accelerator into multiple treatment rooms.

## The cyclotron

Despite being the first cyclic accelerator (invented in the early 1930s), the cyclotron remains the efficient workhorse of many accelerator applications including proton therapy. At lower kinetic energies than 20MeV, the classical Lawrence cyclotron principle may be used: an alternating dee voltage progressively accelerates the protons to a desired extraction energy (see Figure 1.4). At higher kinetic energies needed for proton therapy, the revolution frequency sufficiently varies so that it must be compensated either by increasing the field with radius (isochronous cyclotron) or by changing the dee frequency (synchrocyclotron, which is feasible because of the low requirement on average current). Cyclotrons become progressively more complex as their extraction energy is increased and are generally designed to deliver a single extracted energy, which is fixed and must be degraded before impinging on the patient. This is usually performed with a pair of absorbing wedges (typically graphite) that reduce the energy without undue scattering and straggling [124]. Most existing treatment facilities utilise a single energy selection system and then adjust the downstream beam transport system magnet.

Albeit 250 MeV proton energy is accessible from cyclotrons at ever-decreasing cost, they struggle to achieve energies more than this. Experimental (nuclear physics-led) cyclotrons like those at PSI and Gatchina have achieved higher energies than 250 MeV, but these accelerators are by no means compact and are unlikely to be suitable for widespread hospital use. Anyway, higher energies are interesting because they can find use for diagnostic applications such as proton computed tomography.

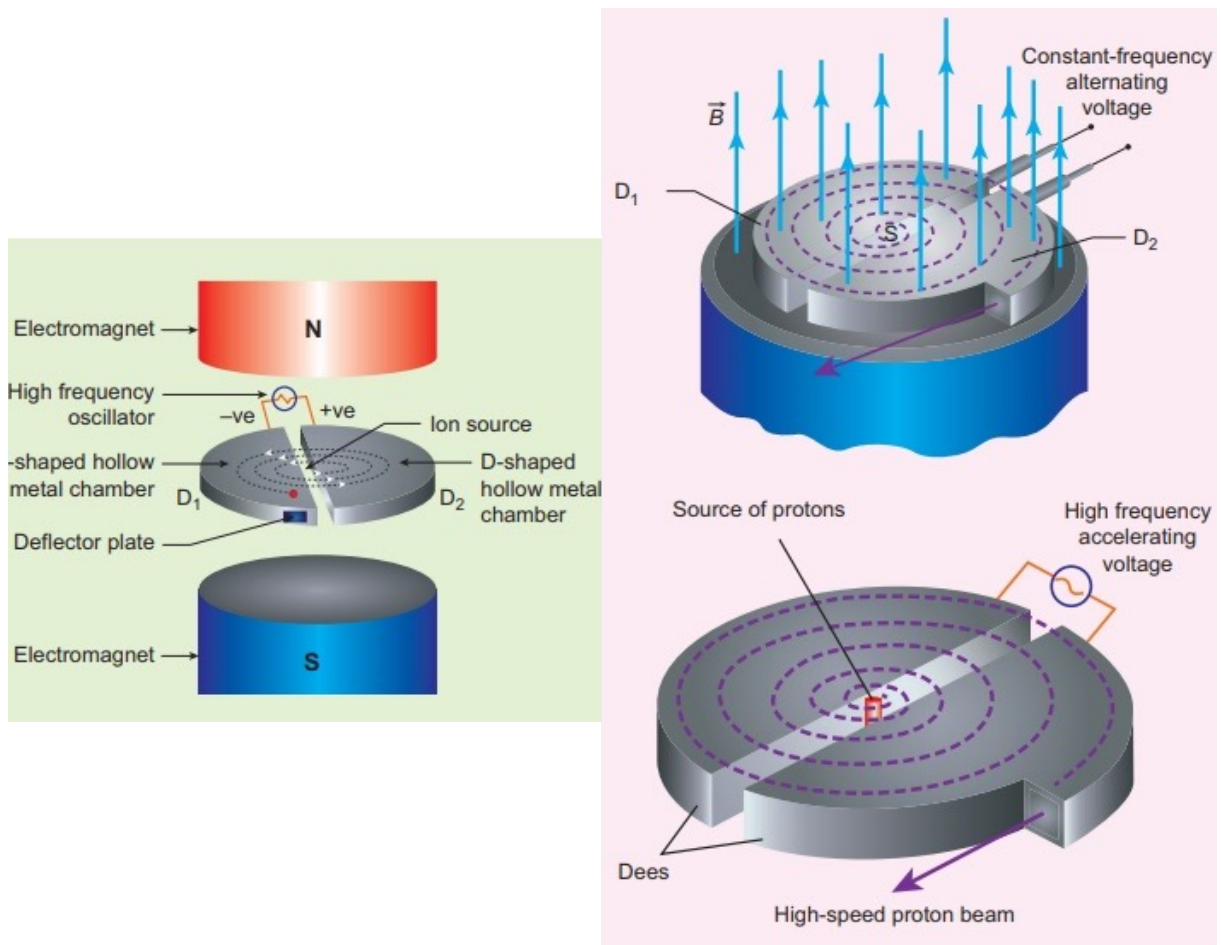


Figure 1.4: Illustration of the operation of a classical cyclotron. The generated dipole field  $B$  is static, and within it the protons are gradually accelerated (after injection from an ion source) within the vacuum vessel due to the alternating voltage applied across the gap between the dees, which may be as much as 100 kV per turn or more.

## The synchrotron

The synchrotron is the other widely used technology for charged particle therapy.

In contrast with cyclotrons, the magnetic guide field varies as the particles are accelerated such that the bend radius, hence the overall path, of the particles remains constant; moreover, the revolution frequency and the accelerating cavity frequency also increase through the acceleration cycle. This results in smaller magnets than in a cyclotron and in their larger number (in particular, quadrupoles) to provide the necessary periodic strong focusing. Since the magnetic field varies there can only be one pulse of protons circulating in each acceleration cycle, differently from the isochronous cyclotron where many different bunches are simultaneously present with different energies. To overcome this limit many more protons are placed in each accelerated bunch, as much as 10 nC or more.

The principal advantage of the synchrotron is that the energy may be varied in each acceleration cycle avoiding the need for an energy degrader, which greatly reduces the average current requirement. Coupling this with the higher proton bunch charge, it results in a clinical treatment time which is much the same as from a cyclotron, about a minute. Another advantage is that synchrotrons accelerate particles with larger magnetic rigidities than is readily achieved from a cyclotron; so, at present, synchrotrons are the only accelerators used for carbon therapy (for instance, at HIT, CNAO, MedAustron and NIRS). Even though some significant design work has been performed to construct a superconducting cyclotron suitable for carbon therapy, there is no commercial product available yet [48]. For synchrotrons, it is rather difficult to adopt superconducting technology: the challenge is the rapid field variation of a superconducting magnet. Consequently, it is troublesome to significantly reduce the footprint of a synchrotron other than to reduce the number of magnetic cells as much as possible.

Other technology developments are today considered like fixed-field alternating-gradient accelerator (FFAG), linacs, dielectric wall accelerators, or Laser proton acceleration (for more details see Ref. [86]). In the future, it seems highly likely that superconducting cyclotrons will become much more widespread. Several companies are developing high-field cyclotron solutions, and the marketplace is likely to benefit from the possible cost reductions from the diminution in physical mass of such systems. Since cyclotrons give an inherently stable, quasi-continuous output, they are favoured despite the relatively large losses which must be incurred in their energy selection systems. Reducing their cost will make it more challenging for new technology entrants such as linear accelerators to compete: the market appears to be driven by the desire to reduce the treatment costs rather than to introduce higher-capability technology.

### 1.3. Beam delivery system

New proton therapy centers all deliver the beam using pencil beam scanning (PBS), in which the whole tumor volume is scanned in 3D using a narrow pencil beam [23]. PBS is also used in most of C-ion centers, with only a few centers in Japan still using the old passive modulation systems. PBS provides an unsurpassed conformity, but is problematic for moving targets, especially thoracic and abdominal tumors that move with breathing. Accelerator beam distribution is vertically and horizontally scanned by magnets (Figure 1.5), while the beam range is controlled by modifying the beam energy. The time to change the beam energy is around 2 seconds, or less, and the time to deliver the volumetric dose is of the order of a minute.

A typical target volume is divided by the treatment planning system into 30÷100 slices

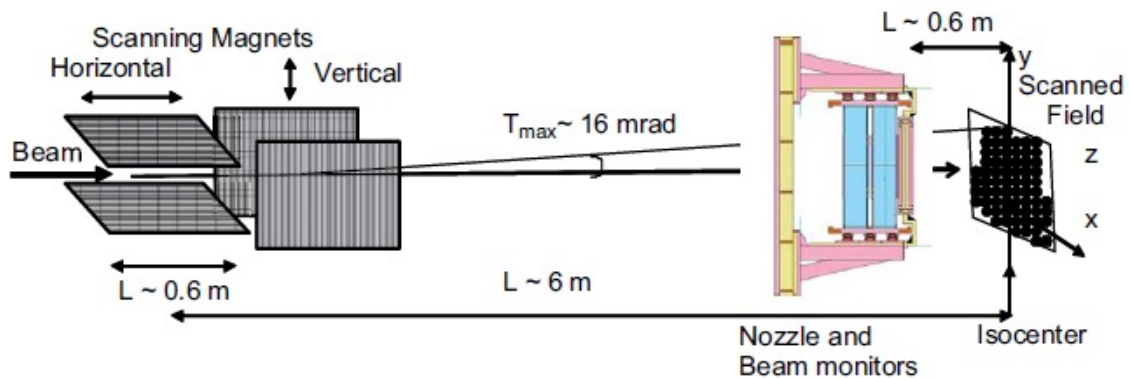


Figure 1.5: The CNAO horizontal beam line setup. The beam is deflected by horizontal and vertical scanning magnets to reach the desired spatial coordinates. Downstream the magnets, a set of monitor chambers are used to measure the beam fluence and position. Figure from Ref. [35].

along the beam axis; I will refer to these slices as "energy layers", as each layer is irradiated by a corresponding beam energy. Each slice is then characterized by a sequence of spots (typically, 1÷1000), which are bunches of particles; in turn, each spot is characterized by a certain energy, flux (in terms of number of particles), displacement of the beam ( $\Delta x$ ,  $\Delta y$ ) from the isocenter. When the required dose is reached on one spot, the beam is quickly moved to the next spot without being turned off.

There are different types of scanning, as shown in Figure 1.6. In spot scanning, the beam is online just in the represented dots, thus offline between them. This is the main difference with respect to the raster scanning, in which the structure of spots is the same, but the beam remains "on" during the whole treatment delivery. A different concept applies to continuous line scanning, where the dose is delivered across a linear path, rather than as

spots, and the beam may be turned off when moving to subsequent lines [138].

A cyclotron produces a high intensity, continuous beam, whose energy is fixed and can be

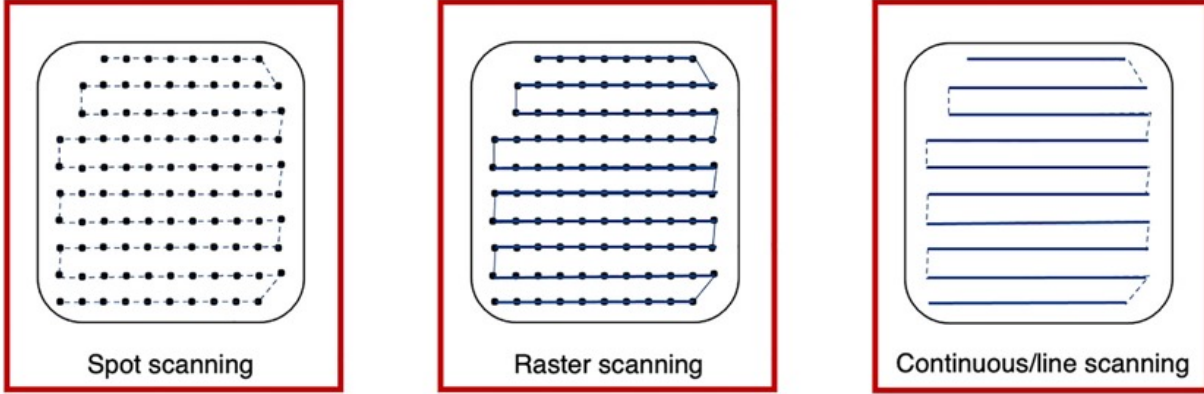


Figure 1.6: Schematic representation of spot, raster and continuous line scanning patterns for PBS delivery. Spots and solid lines indicate beam-on irradiation and dashed lines indicate movement with beam-off. For spot scanning, the beam is turned off between movement to the next spot but remains on for the whole delivery in raster scanning. For continuous line scanning, the dose is delivered across a linear path (rather than as spots) and may be turned off between movement to subsequent lines. Figure from Ref. [138].

degraded with passive absorbers in the energy selection system. Instead, in synchrotrons, particles' extraction happens in cycles, spills, that last about 1 second each, while, in 2 seconds, beam energy can be varied from spill to spill without passive elements (Figure 1.7). A spill can cover an energy layer with different number of spots.

Typically, the energy of a therapeutic proton beam ranges between  $60 \div 250$  MeV, for a particle number per spill lower than  $10^{10} \frac{p}{spill}$ , which corresponds to a current of about 2nA. For carbon ions, the energy range used in therapeutic treatments is  $120 \div 400 \frac{MeV}{u}$ , with an amount of particle lower than  $4 \times 10^8 \frac{C-ions}{spill}$ , to which a current of about 0.4nA is associated.

## 1.4. Physics of the interaction between particles and matter

In this section, electromagnetic and nuclear interactions of charged ions in matter are reviewed. We will focus on particle types and energies currently used in hadrontherapy centers, worldwide. This means to consider interactions of protons up to about 250 MeV and carbon ions up to about  $450 \frac{MeV}{u}$ , i.e., penetrating into the human body up to about 40 cm.

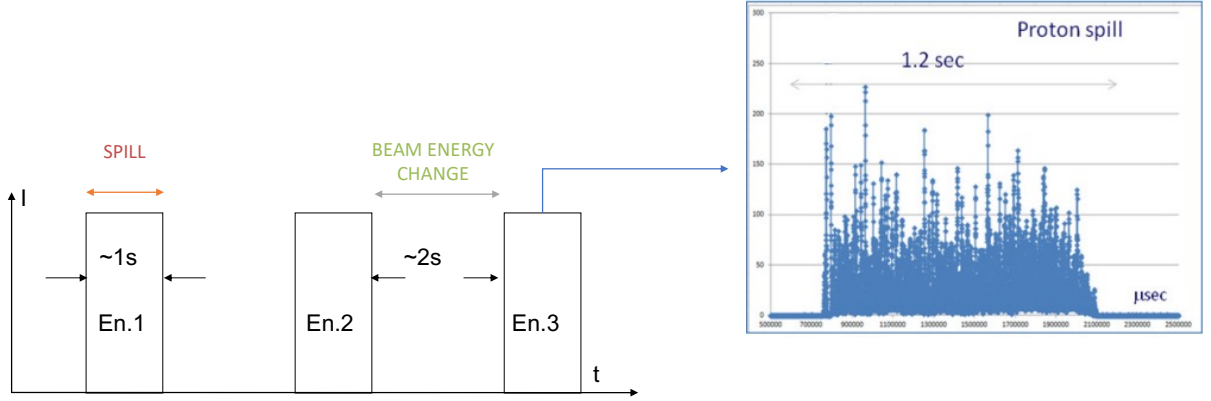


Figure 1.7: Beam current trend over time for a clinical treatment. A spill last about 1s and covers energy layer with a certain number of spots. The time to change energy in a synchrotron is about 2s. On the right, the time structure of a proton beam spill is represented, and the figure was taken from Ref. [13]

Before going into detail, let us first look at typical velocities. For a particle of kinetic energy  $E_{kin}$ , total energy  $E_{tot}$ , rest mass  $m_0$ , and momentum  $p$ , the particle velocity  $\beta$  normalized to velocity of light,  $c$ , is given by Eq. 1.1:

$$\beta = \frac{v}{c} = \frac{pc}{E_{tot}} = \frac{\sqrt{E_{tot}^2 - m_0^2 c^4}}{E_{kin} + m_0 c^2} \quad (1.1)$$

For a proton with kinetic energy,  $E_{kin}$ , of 250 MeV and given the proton rest mass,  $938 \frac{MeV}{c^2}$ , we find  $\beta_p \approx 0.6$ ; while a carbon ion with energy  $450 \frac{MeV}{u}$  has  $\beta_C \approx 0.7$ . Thus, in radiotherapy, particles are moderately relativistic

### 1.4.1. Interaction of charged hadrons

Moderately relativistic charged particles interact with matter by electrical (Coulomb) forces with the atomic electrons and nuclei. The particle loses energy primarily by inelastic collisions with the atomic electrons, resulting in ionization and atomic excitation. These are continuous energy losses. When the ejected electron is so energetic that it can cause ionization itself, it is called "delta-ray". The amount of energy lost in each Coulomb interaction with the material nuclei is very small. Indeed, the maximum energy that can be transferred from a charged particle of mass  $m$  with kinetic energy  $E$  to an electron of mass  $m_0$  in a single collision is  $4E \frac{m_0}{m}$ ,  $\sim \frac{1}{500}$  of the particle energy per nucleon. However, the particle interfaces itself with so many electrons that the net effect is the continuous decrease of its velocity until it stops.

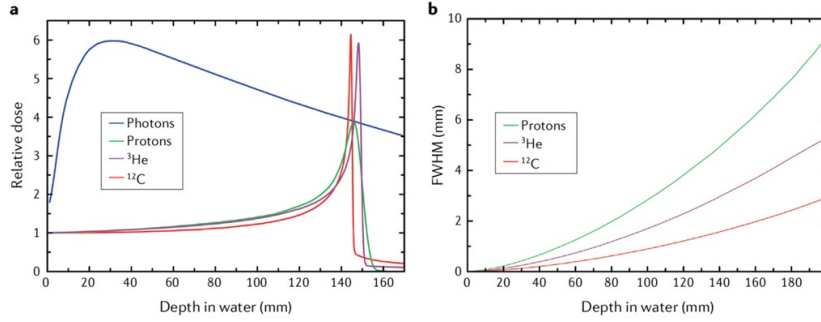


**Figure 1.8:** **a)** Depth-dose distributions showing the Bragg peak for different ions. The X-ray depth-dose curve is calculated for a 21MeV linac, while the energies of the ions correspond approximately to the same range: 148MeV for protons,  $170 \frac{MeV}{u}$  for <sup>3</sup>He-ions and  $270 \frac{MeV}{u}$  for <sup>12</sup>C-ions. **b)** Lateral broadening (full-width-at-half-maximum of the Gaussian distribution) for the same ions. The widening of the beam should be compared with typical entrance spot sizes of proton and ion beams of  $\sim 5 \div 10$  mm. Figure from Ref. [25].

Except at their very end, the tracks tend to be quite straight because the particle is not greatly deflected, and interactions occur in all directions simultaneously. Charged particles are therefore characterized by a definite range, which can be defined more precisely as the distance beyond which no particles will penetrate in a given target. The Bragg peak makes particles so appealing compared with X-rays, characterized by a depth-dose curve that decreases exponentially after the initial build-up (Figure 3.3a).

## Linear Energy Transfer

The energy loss per unit mass length is known as stopping power  $S$  in Physics and LET in Radiobiology. It is described by the Bethe-Bloch equation in the framework of the continuous slowing down approximation theory:

$$S = \frac{4\pi N_A e^4 Z_p^2 Z_T}{mc^2 \beta^2 A_T} \left[ \ln\left(\frac{2mc^2 \beta^2 \gamma^2}{I}\right) - \beta^2 - \frac{C(\beta)}{Z_T} + Z_p L_1(\beta) + Z_p^2 L_2(\beta) + L_3(\beta) \right] \quad (1.2)$$

where  $e$  is the electronic charge,  $N_A$  the Avogadro number,  $m$  the mass of the electron,  $c$  the speed of light;  $Z_p$  is the effective charge of the projectile,  $\beta$  its relative velocity and  $\gamma$  the Lorentz factor;  $Z_T$  is the atomic number of the target material and  $A_T$  is its mass number. In the logarithmic term,  $I$  is the mean excitation energy, an experimentally determined parameter for each element, which represents one of the main sources of range uncertainty in particle therapy. Additional correction terms are the shell correction  $C$ ,

Barkas correction  $L_1$ , Bloch term  $L_2$ , and Mott and density corrections  $L_3$ .  $S$  and LET are expressed, respectively, as  $\frac{MeVcm^2}{g}$  in Physics and as  $\frac{keV}{\mu m}$  in water (density  $1\frac{g}{cm^3}$ ) in Radiobiology.

Equation 1.2 is generally valid for different types of charged particles, provided that their velocity remains large compared with the velocities of the orbital electrons in the absorbing atoms. For a given non-relativistic particle,  $S$  therefore varies as  $\frac{1}{v^2}$ , or inversely to the particle energy. This behavior can be heuristically explained by noting that, because the charged particle spends a greater time at low velocity in the vicinity of an electron, the energy transfer will be the largest. Moreover, one can notice that  $Z_T$  and  $A_T$ , outside the logarithmic term, rule the behavior of different materials hit by external radiation. Hence, high atomic number, high-density materials will consequently result in the greatest linear stopping power. Equation 1.2 also shows the proportionality to the square of the ion charge and, therefore, it can be much higher for heavy ions than for protons, depending on the energy. This is the key to biological advantages of heavy ions: the RBE increases with LET bringing to the production of more clustered DNA lesions, difficult to repair. For very low energies, when  $\beta$  becomes comparable or less than the velocity of the orbital electrons, the so-called Lindhard region, Equation 1.2, is no longer valid. Then, the energy loss becomes proportional to  $\beta$  [60]. In between the Bethe-Bloch and the Lindhard region, energy losses can be described by the low energy model of Anderson and Ziegler [141]. The electronic stopping power as function of the kinetic energy of protons impinging on a water target is shown in Figure 1.9.

Finally, charge exchange between the particle and matter becomes important. The positively charged particle will then tend to pick up electrons from the material, reducing its charge and, consequently, its linear energy loss. At the end of the track, the particle has accumulated  $z$  electrons and becomes a neutral atom.

## Scattering

Beyond inelastic collisions with the atomic electrons, a charged hadron also may undergo numerous elastic Coulomb scatterings from nuclei themselves. Beam dispersion in the longitudinal and lateral directions is an important feature in particle therapy. Longitudinal straggling  $\sigma_R$  determines the width of the Bragg peak at a range  $R$ . For two particles of different mass  $M$  at the same range  $R$ , it can be shown that:

$$\frac{\sigma_{R1}}{\sigma_{R2}} = \sqrt{\frac{M_2}{M_1}} \quad (1.3)$$

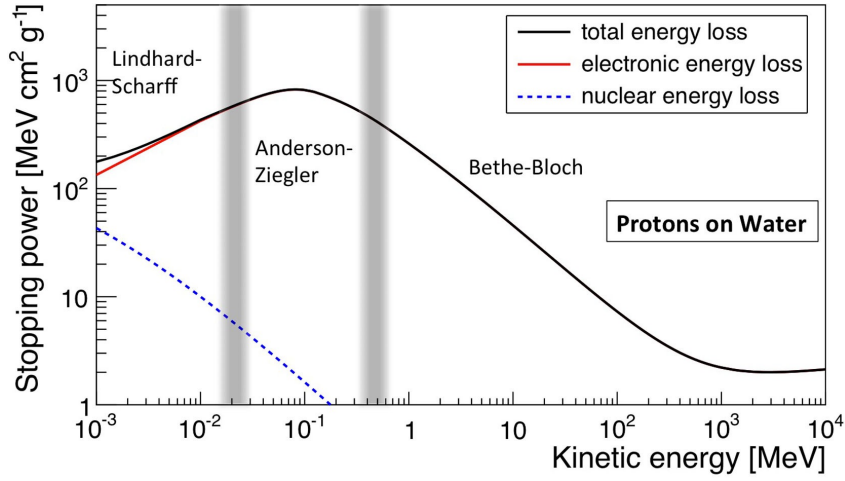


Figure 1.9: Stopping power,  $S$ , in  $\frac{\text{MeVcm}^2}{\text{g}}$ , for protons in water as function of kinetic energy. The total, electronic, and nuclear stopping power are shown, as well as the characteristic regions. Figure from Ref. [60].

Equation 1.3 shows that longitudinal straggling is lower for heavy ions compared with protons, resulting in a sharper and more precise Bragg peak (see Figure 3.3b).

Lateral scattering for thick targets is dominated by multiple Coulomb scattering and is well described by Molière's theory. At small scattering angles, the theory approximates the scattering distribution as a Gaussian with standard deviation  $\sigma_\theta$  that can be described as:

$$\sigma_\theta = \frac{14.1\text{MeV}}{\beta pc} Z_p \sqrt{\frac{d}{L_{rad}}} \left[ 1 + \frac{1}{9} \log\left(\frac{d}{L_{rad}}\right) \right] \quad (1.4)$$

where  $d$  is the total mass thickness and  $L_{rad}$  is the radiation length, which depends on the atomic number  $Z$  of the target material.  $\beta$  is relative velocity of the projectile, while  $p$  is its momentum.

Equation 1.4 shows that multiple Coulomb scattering increases for thick and heavy targets (since  $L_{rad} \approx Z^{-2}$ ), whereas it decreases with particle velocity and, for the same range, with particle mass (Figure 3.3b). Quantitatively, protons have a lateral scattering that is approximately three times greater than C ions at a depth of 15cm. However, at greater depths, C-ion projectiles gain substantial contributions to the lateral dose from secondary fragments produced by nuclear interactions, and the C-ion lateral dose distributions become like those of protons.

Lateral scattering is responsible for the dose halo in treatment planning and makes dose fall-off sharper for heavy ion treatments. This property is attractive for sparing organs

at risk (OAR), especially in hypofractionation, when the smooth fall-off can produce substantial doses to the OAR surrounding the tumor.

## Fragmentation of heavy ions

Nuclear fragmentation is another major difference between protons and heavy ions. Both induce fragmentation of target nuclei, which, in the body, are mostly  $^{16}\text{O}$ , but protons do not undergo fragmentation after nuclear interactions, whereas heavy ions break into lighter projectile fragments. The nuclear fragmentation cross section,  $\sigma_f$ , at high energies is well described by the geometric Bradt-Peters approximation:

$$\sigma_f = \pi r_0^2 (A_p^{\frac{1}{3}} + A_T^{\frac{1}{3}} - b)^2 \quad (1.5)$$

where  $r_0$  is the nucleon radius ( $\sim 1\text{fm}$ ),  $b$  the overlapping parameter;  $A_p$  and  $A_T$  are, respectively, the mass number of the projectile and the target nuclei.

Equation 1.5 shows that the cross section increases as  $\sim A_p^{\frac{2}{3}}$  and is, therefore, more significant in heavier ions.

The projectile fragments have similar velocity and direction to the primary ion but lower charge, and, consequently, have larger range. They generate a ‘dose tail’ beyond the Bragg peak, which is not observed in proton irradiation (Figure 3.3a). The mean free path for  $350 \frac{\text{MeV}}{u}$  carbon ions in water, whose computed range is 20cm, is approximately 25cm, meaning that only about 50% of the accelerated  $^{12}\text{C}$ -ions actually reach a deep-seated tumor, the others undergoing nuclear fragmentation. However, in most practical cases, the tail is within the planned high-dose region in the patient, because two parallel opposed beams are often used. Treatments with single beams are, indeed, generally avoided because of the problem of the range uncertainty, which is the main physics problem limiting the precision of particle therapy.

At the same time, fragmentation can be beneficial for treatment monitoring and reducing range uncertainty. Image guidance is essential for heavy ions, even more than for X-rays. In fact, the sharp dose gradients in heavy ion therapy become a problem if the target is missed and the Bragg peak occurs in an OAR. For this, in clinical particle therapy, a substantial margin is added to the prescribed range in order to ensure tumor coverage, sparing normal tissues. Anyway, wide margins jeopardize one of the main advantages of the Bragg peak: the steep dose gradients and the potential high accuracy and precision. It is, therefore, desirable to monitor heavy ion treatments precisely and, thereby, reduce these margins.

Image guidance was originally developed for X-rays and is taking time to be fully exploited

in particle therapy, where additional complications can occur. However, the physics of charged particles offers unique opportunities for in vivo range verification [57]. For instance, in C-ion therapy, fragmentation of the primary ion generates positron-emitting isotopes, above all  $^{11}\text{C}$ . Positron annihilation with electrons produce two 511-keV  $\gamma$ -rays emitted at  $180^\circ$  to each other that can be visualized by a PET system that is positioned around the patient during the treatment. A similar approach can be used with heavier ion beams, such as  $^{16}\text{O}$ . Hence, in heavy ion therapy, the projectile fragments provide a large part of the signal, whereas in proton therapy, only target fragments can be used for imaging.

### 1.4.2. The origin of prompt gamma rays

Beyond inelastic collisions with the atomic electrons, charged particles can also suffer nuclear interactions with the material nuclei, which contribute significantly less to energy losses than electromagnetic processes (see Figure 1.9). Still, they are highly relevant for range verification methods, as shown below. Contrary to electromagnetic interactions, no rigorous models exist to describe them. In the following, the common approach to model nuclear interactions is described, as adopted by most state-of-the-art MC codes.

To start, as a general aspect, we can say that nuclear interactions (collisions) can be divided into:

- *Elastic collisions.* Kinetic energy is conserved, and the nucleus stays intact. This is similar to multiple Coulomb scattering, but now due to strong interaction rather than electromagnetic ones. Such interactions are not occurring so frequently, but still, they cause a certain amount of broadening of the beam.
- *Inelastic collisions.* Reactions between projectile and target, where total kinetic energy is not conserved. The projectile may knock out secondary particles (protons, neutrons, deuterons,  $\alpha$ s, etc.) from the nucleus and may break into fragments.

## Nuclear Interactions of Protons

A proton hitting the atomic nucleus starts a series of nucleon-nucleon collisions, which leads to emission of protons, neutrons, light fragments, and to equilibrium of the remaining nucleus. First, the intranuclear cascade model (INC) has been applied successfully to the study of heavy ion collisions for a beam energy ranging from 250MeV to 2GeV per nucleon [28]. It was developed at the very beginning (the original ideas go back at the end of the 40's) of the history of energetic nuclear interaction modelling, but it is still valid. The model is intrinsically a Monte Carlo code, well suited for numerical applications,

while no closed analytical expression can be derived without severe approximations. One of the fundamental requirements for a model describing nuclear interactions to be applied in practical calculations is speed. The best approach to the speed problem is to use a Monte Carlo method, simulating at run time every interaction, which involves the ability to model, in reasonable time, almost whichever target nucleus and whichever projectile, with no or small need for external input information or preliminary calculations. The speed of such model is a key feature, since large number of interactions can be simulated within an acceptable time and most INC codes are fast enough so that they do not represent any significant limitation to the CPU required.

Classical INC codes are based on more or less accurate treatment of hadron multiple collision processes in nuclei, with the target being assumed to be a cold Fermi gas of nucleons in their potential well [36]. The hadron-nucleon cross section used in the calculations are free hadron-nucleon cross sections. This “free” nucleon approach is justified if the De Broglie wavelength  $\lambda_h$  of the incident particle is much smaller than the average distance  $d_{ave}$  between the nucleons in the material nucleus, and much smaller than the mean free path  $\lambda_N$  inside the nucleus:

$$\lambda_h = \frac{2\pi\hbar}{p} \ll d_{ave} = \left(\frac{3}{4\pi\rho_N}\right)^{\frac{1}{3}} \quad (1.6)$$

$$\lambda_h = \frac{2\pi\hbar}{p} \ll \lambda_N = \frac{1}{\sigma\rho_N} \quad (1.7)$$

where  $\sigma$  is the proton-nucleon cross section and  $\rho_N$  is the intranuclear density (typically  $0.17 \frac{nucleons}{fm^3}$  at the center of nuclei).

Another requirement for this approach to be valid is that the time in which a collision happens is smaller than the time between the collisions, so that they take place independently. For radiotherapeutic energy ranges, it is not obvious the validity of this approach. For instance, a proton of kinetic energy 250MeV has  $\lambda_h \sim 1\text{fm}$ , which is roughly the same as  $d_{ave}$ , making invalid the condition in Equation 1.6.

The basic assumptions of INC models can be summarized as follow:

1. Hadrons propagate like free particles in the nuclear medium, with interaction probability per unit length given by free space cross sections, properly averaged over the Fermi motion [8] of the target nucleons, times the local nuclear density.
2. The particle motion is formulated in a classical way. It can be subject to an average nuclear mean potential, which must be added to the free particle kinetic energy

when tracking through the nucleus. The radial and energy dependence of such field are model and particle dependent.

3. The effect of the nuclear mean field on the particle motion can either be null or can produce curved trajectories in a semiclassical approach, according to energy and momentum conservation, depending on the model. The curvature effects induced by the nuclear mean field are usually referred to as refraction and reflection effects.
4. Interactions occur like in free space in the Center of Mass System of the two colliding hadrons. Of course, because of the Fermi motion, the lab frame will not coincide with the frame where the target nucleon is at rest, but suitable Lorentz boosts [28] have to be applied to transform back the secondary particles in the lab frame.
5. Interactions occur in a completely incoherent and uncorrelated way. No coherence or diffractive effect is included. No multibody or cluster process is included, except for pion absorption.
6. Quantum effects are mainly limited to Pauli blocking [28]: only few codes contain further quantum effects.
7. Secondaries are treated exactly like primary particles, with the only difference that they start their trajectory already inside the nucleus.

A typical INC code usually follows the following logic:

- Target nucleus description, typically realized through a few concentric spheres of different density and Fermi energy.
- Geometrical cross section, corresponding to the nuclear radius or to the maximum possible impact parameter.
- Impact parameter selection with a constant probability over the geometrical cross section area. More than one selection can be required if the particle crosses the nucleus without interacting.
- Interaction point selection and projectile tracking through the nucleus, according to Fermi motion averaged hadron-nucleon cross sections and possibly to the nuclear mean field, including the Coulomb field.
- Target nucleon selection according to  $\sigma_{hp}$ ,  $\sigma_{hn}$  and local Fermi energy.
- Interaction simulation according to free hadron-nucleus interactions, local Fermi energy and Pauli blocking.
- Secondary tracking into the nucleus, until interaction, escape, or energy cut-off.

- (Possible) preequilibrium stage, whenever all excited nucleons are below a given energy threshold (typically a few tens of MeV). This stage is included only in the most recent developments.
- Evaporation stage whenever the preequilibrium stage is finished, or all particles are below a given threshold (usually of the order of the binding energy), and the system can be assumed to be equilibrated.
- Final deexcitation stage when the excitation energy is below the threshold for particle emission and it is spent through photon emission.

A detailed description of the physics involved in all stages can be found in [28]. In the following, we will briefly describe the main passages.

The physical foundation of INC becomes approximate at low energies, resulting in a decrease of its accuracy. Moreover, it can be very time consuming since many particles must be followed down to very low energies. Already in 1966 Griffin described the spectra following nucleon-induced reactions in terms of a pre-equilibrium model, that is, a transition between the first step of the reaction and the final thermalization [39]. Since then, many models have been developed.

The pre-equilibrium stage begins when the energy of the particles in the cascade has reached the lower limit of 50 MeV and the nucleus is not yet in thermal equilibrium. It is commonly modeled in Monte Carlo codes according to the exciton model, a semi-classical model introduced to explain high-energy emitted particles in nuclear reactions [7]. The evolution of the nuclear reaction is also pictured as successive nucleon-nucleon collisions, but within a particle-hole, or “exciton,” formalism, where nucleons are excited from the Fermi sea leaving a hole. The nucleus proceeds in the chain of nucleon-nucleon collisions which increase the exciton number by two units, thus if the probability of having an interaction that decreases the exciton number or lets it unchanged can be neglected (the so-called “never come back” approximation). The chain stops, and equilibrium is reached, when either the exciton number is sufficiently high, or the excitation energy is below any emission threshold.

At the end of the preequilibrium stage, a true compound nucleus is left with  $Z_{\text{res}}$  and  $N_{\text{res}}$ , moving with a given residual momentum vector, and with excitation energy  $U$ . The de-excitation stage is then performed starting from this configuration: depending on the mass of the target nucleus and on the energy left, the nucleus can dissipate its remaining energy in several ways such as evaporation, fission, or fragmentation.

Let us first consider the evaporation process. At the end of the exciton chain, or of the INC part whenever no preequilibrium stage is included in the calculation, the residual

nucleus is supposed to be left in an equilibrium state, in which the excitation energy  $U$  is shared by a large number of nucleons. Such equilibrated compound nucleus is supposed to be characterized by its mass, charge, and excitation energy with no further memory of the steps which led to its formation. The excitation energy can be higher than the separation energy, thus nucleons and light fragments ( $\alpha$ ,  $d$ ,  ${}^3\text{H}$ ,  ${}^3\text{He}$ ) can still be emitted: they constitute the low-energy (and most abundant) part of the emitted particles in the rest system of the residual nucleus, having an average energy of few MeV. The emission process can be well described as an evaporation from a hot system, as in the Weisskopf-Ewing approach [129].

The evaporative process is in competition with another equilibrium process, that is fission. A fraction of the excitation energy may be spent to induce a collective deformation. As the nucleus shape departs from sphericity, the surface energy increases but the Coulomb energy decreases. The potential energy reaches a maximum at a deformation stage that is called "saddle point". The height of the potential energy over the ground state is the fission barrier. Once a nucleus reaches the saddle point, the fission occurs, and the nucleus separates, typically into two heavy fragments. The height of the fission barrier can be, as first approximation, computed with the liquid drop model, incorporating shell effects. For fission probability, a statistical method can be used: it will be equal to the probability of reaching the saddle point, because this is a no-way-back point [9].

The initial nucleus excitation energy,  $U$ , will be divided between a relative kinetic energy of the two fragments,  $E$ , and a residual excitation. After scission, the fragments acquire kinetic energy from the Coulomb repulsion between them. Their mass distribution depends on  $Z$  and on the excitation energy of the fissioning nucleus (fission is negligible for  $Z < 70$ ): for low  $Z$  system, the mass distribution is centered around the half mass; while for high  $Z$  nuclei, the mass distribution has a symmetric component and an asymmetric one in which one of the fragments has always a mass around 140. The two fragments are, then, treated like independent residual nuclei with their own excitation and can possibly emit further particles.

For light nuclei, the statistical assumptions and the sequential emission scheme underlying the classical evaporation models become less and less sound, because:

- Already moderate excitation energies can represent a substantial fraction of the (total) binding energy of such nuclei.
- The level structure of such nuclei is usually highly specific and anyway level spacings can be comparable with the excitation energy.
- The "evaporation" of light fragments other than  $p$  or  $n$  becomes meaningless, since the mass of the "evaporated" fragment can be comparable or even larger than the

mass of the residual nucleus.

Therefore, other de-excitation mechanisms are more suitable for these light (typically  $A < 17$ ) residual nuclei. A possible choice for these calculations is the so called "Fermi Break-up" model [27]: the excitation energy of the excited nucleus may be larger than the binding energy of some fragmentation channels. In this case, nucleus disassembles in one step into smaller fragments, with branching given by plain phase space considerations. Fermi break-up is relevant for radiotherapy because the human body is mainly composed of low-Z nuclei.

Finally, the evaporation stage ends when the nuclear excitation energy becomes lower than all separation energies for nucleons and fragments. This residual excitation energy is then dissipated through emission of gamma rays. Gamma emission occurs even during the pre-equilibrium and evaporation stages, in competition with particle emission, but its branching ratio is low, and it can safely be neglected in most practical applications. Gamma de-excitation proceeds through a cascade of consecutive emissions, until the ground state is reached.

The whole process following nucleon-nucleus interactions is summarized in Figure 1.10.

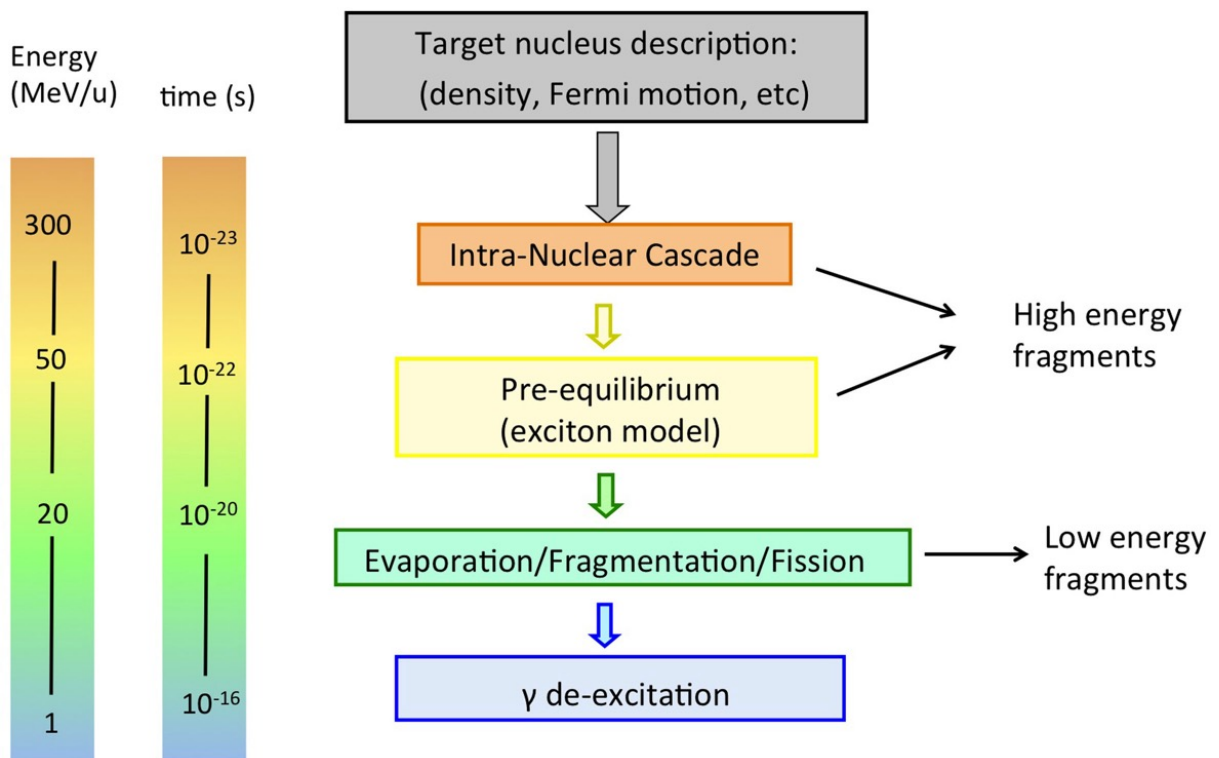


Figure 1.10: Schematic display of stages in a nucleon-nucleus interaction relevant for radiotherapy, together with time scale and energy of interacting particle. Figure from Ref. [60].

## Nuclear Interactions of Heavy Ions

The fundamental difference between nucleus-nucleus and nucleon-nucleus reactions is that the incoming nucleons are not free. Most models for nucleus-nucleus interactions are variants of the “abrasion-ablation” model [43]. During the fast stage (abrasion, time scale  $\sim 10^{-22} \div 10^{-23} s$ ), the projectile and target nuclei overlap, resulting in a kind of reaction zone. An excited quasi-projectile is formed with much of the initial velocity, a quasi-target fragment at rest, and several excited light fragments. During the slow step (ablation, time scale  $\sim 10^{-18} \div 10^{-16} s$ ), the remaining projectile, target and light fragments de-excite by evaporating light nuclei or fragments. It must be noted that in this case both target and projectile-nuclei can fragment, as opposed to proton irradiation, where only the target-like nuclei can fragment (see Figure 1.11). The projectile fragments travel further in the forward direction, losing energy through ionization and undergoing further interactions. These fragments have approximately the same velocities and directions as their mothers, but larger ranges than the primary ions as range scales with  $\frac{A}{Z^2}$ . This leads to the characteristic tail beyond the Bragg peak.

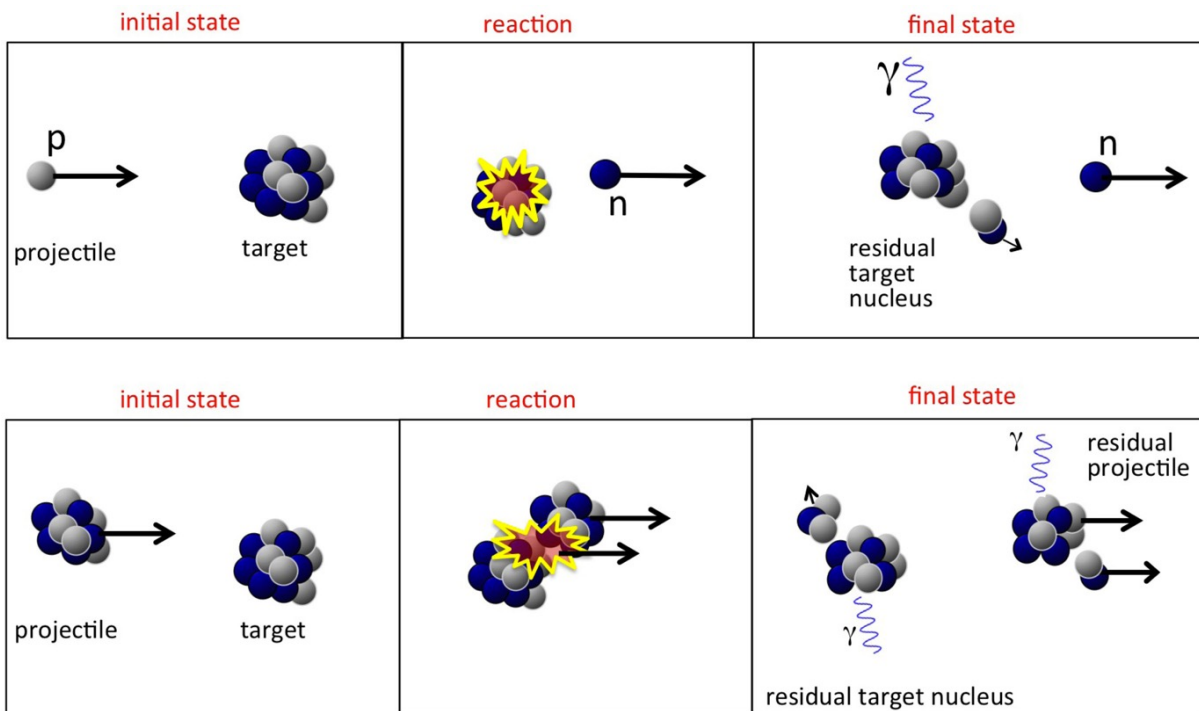


Figure 1.11: Top: sketch of a possible nucleon-nucleus reaction in proton therapy, whereby a neutron is created. Bottom: sketch of nucleus-nucleus reaction in heavy ion therapy, with creation of light fragments. Figure from Ref. [60].

The target fragments have short ranges and high stopping power, and their evaporation products are evaporated isotropically in the reference frame of the target fragments. To

describe the dynamics of these reactions, various models have been proposed, which are mainly different in the treatment of the nuclear field affecting the propagation of the particles inside the nucleus. Examples are:

- *Intra-nuclear cascade model*. For high-energy nuclei with energies above about  $100 \frac{\text{MeV}}{u}$ , the description is similar to what was outlined above for protons.
- *Quantum molecular dynamics (QMD)*. Valid for energies from 50 to about  $400 \frac{\text{MeV}}{u}$ , this model can be seen as sophisticated form of the INC model. Here, each nucleon is described by a gaussian wave packet, and all nucleons in the projectile and target nuclei are participants in the collision process. By minimizing the Hamiltonian describing nucleon-nucleon interactions when projectile and target nuclei overlap, it predicts the formation of heavy or light nuclei and secondary protons and neutrons. Because of their complexity, these models are generally much slower in MonteCarlo codes than the normal INC model.
- *Boltzmann-Master-Equation (BME)*. It is a sophisticated model to simulate the pre-equilibrium stage, describing the thermalization of composite nuclei for projectiles with energies below  $100 \frac{\text{MeV}}{u}$  down to the evaporation/fission/break-up stage. Based on a set of time-dependent transport equations, BME describes how a statistical state far from equilibrium evolves to an equilibrium state, through a sequence of two-body interactions and emission of unbound particles (neutrons/protons) and clusters (heavy/light nuclei).

For the de-excitation phase in nucleus-nucleus interactions, the same models as those already described for nucleon-nucleus interactions are used: evaporation, fission, Fermi-breakup, and gamma emission.

## Conclusions

Various types of secondary particles are produced, which can be used for particle range verification. All three stages of the nuclear reactions contribute to the production of secondaries. The INC and pre-equilibrium stage mostly lead to production of high-energy secondary particles (with energies that may exceed even a hundred MeV), emitted mostly in the forward direction in the laboratory frame. The slow part of the nuclear interaction leads to lower energy secondaries, emitted almost isotropically in the center-of-mass frame of the parent nucleus. In the case of ion projectile emissions, this implies mostly forward in the laboratory system due to the kinematic boost. Three types of secondaries are used for range monitoring in hadron therapy:  $\beta^+$  emitting isotopes, which can be measured with a PET detection system, enabling to extract information about the beam path; prompt

gammas, which accompany the nuclear reactions along much of the primary particle path and are emitted with energies ranging from 0 to about 10 MeV; charged fragments are produced, which can possibly be measured and used for verifying particle range.

### 1.4.3. Interaction of electromagnetic radiation with matter

Indirectly ionizing photons can be subdivided into multiple groups. Let us start from  $\gamma$ -rays, which have a discrete energy spectrum and are emitted during nuclear transitions. Bremsstrahlung X-rays have, instead, a continuum energy spectrum and are generated by the acceleration/deceleration of charged particle, mainly electrons. There exists also characteristic X-rays, produced in transitions of electrons bound to atomic shells (K, L, M, etc...) with a discrete energy spectrum. Then, annihilation  $\gamma$ -rays are generated following a positron annihilation with an electron.

The electromagnetic radiation is a useful tool for radiation therapy. Indeed, the  $\gamma$  emitters  $^{60}\text{Co}$  and  $^{137}\text{Cs}$  are currently employed in brachiterapy (seeds of various radionuclides implanted locally into the tumor), while other gamma emitters incorporated in radiopharmaceuticals are employed in the Single Photon Emission Tomography (SPECT diagnostics). Then, bremsstrahlung X rays are generated by accelerated electrons impinging on high  $Z$  materials (such as W, Pb) and are employed in radiation therapy and diagnostics (radiography, CT, etc.). Not to think at the importance of annihilation  $\gamma$ -rays, which are widely exploited in Positron Emission Tomography (PET), where radiopharmaceuticals loaded with  $\beta^+$  emitters (generally  $^{18}\text{F}$ ) reach the organs to be examined.

While photons are interacting with matter, some partners play a part into the interactions: atomic electrons, nuclei or nucleons, and nuclear electric field. The effect of the interaction can be various, from a complete photon absorption to inelastic (incoherent) or elastic (coherent) scattering. Among the full set of interactions with matter, some of them are the most probable:

- **Photoelectric effect.** It leads to the total absorption of the impinging photon from an electron bound to its atom. This phenomenon cannot occur after the interaction of a photon with a free electron, since energy and momentum conservation is not fulfilled. Therefore, for finite energies, the photoelectric effect occurs only if the target electron is initially bound to an atom, since momentum is conserved by the whole residual atom recoil. From this consideration it can be inferred that the photoelectric effect possesses a higher probability of occurrence with highly bound electrons. Experiments have demonstrated that about 80% of photoelectric effects occur with K shell electrons. This effect is a threshold reaction which can occur only if the impinging photon energy is higher than the electron binding energy. After the

occurrence of the photoelectric effect, the residual atom is left into an excited state, since the emitted electron left a free orbital which is filled by less bound electrons from more external shells: characteristic X-rays and Auger electrons are emitted during this atomic de-excitation. It should be stressed that the photoelectric effect is more probable the higher is the atomic number of the target,  $Z$ , material and the lower is the impinging photon energy,  $E$  (staying, however, above its threshold value) as shown by Eq. 1.8:

$$\sigma_{\text{ph}} \propto \frac{Z^n}{E^{3.5}} \quad (1.8)$$

where  $n$  ranges between 4 and 5.

For low impinging photon energies, photoelectrons tend to be emitted perpendicularly to the photon incidence direction, while at higher energies their angular distribution tend to be forward-peaked.

- **Compton effect.** When the photon energy is not negligible with respect the rest electron energy, the incoherent scattering must be described through a relativistic theory. The Compton effect describes photon scattering interactions with atomic electrons; the model assumes that the impinging photon energy is higher than the binding energy of the electron, which can be considered as free. For lower photon energies, when the electron binding energy cannot be neglected, correction coefficients should be accounted for.

The kinetic energy of an electron emitted by the Compton interaction is of primary importance for the estimate of the absorbed dose in a radiation therapy treatment since the dose is given by secondary electrons.

The Compton cross section is proportional to the atomic number,  $Z$ , of the target material.

- **Rayleigh scattering.** Rayleigh scattering is more probable at low energies, when photon energy is smaller than the electron binding energy. In this process, photons are scattered by the atomic electrons and the atom is neither ionized nor excited. The impinging photons change their initial direction, and the atom absorbs the recoil momentum, but the recoil kinetic energy is negligible, since the electron mass is much lower than the atom one.
- **Pair production.** At photon energies higher than  $2m_e c^2 = 1022 \text{keV}$ , the phenomenon of pair production may occur. In this process, the impinging photon, first, interacts with the Coulomb nuclear field; then, it is absorbed completely; finally,

an electron-positron pair is created. Pair creation can be modelled according to the Dirac theory, by considering positrons as holes in negative energy states which are initially filled completely by electrons. These negative energy states come from the negative square root of the fundamental relativistic relation (Eq. 1.9):

$$E = \pm \sqrt{p^2 c^2 + m_0^2 c^4} \quad (1.9)$$

The model of pair creation is strictly linked to Bremsstrahlung phenomenon. In both processes, an interaction with the Coulomb nuclear field occurs; but, in the latter, an electron undergoes a transition between two positive energy states and a photon is emitted instead of being absorbed. Since both processes depend on the square of the atomic number of materials,  $Z^2$ , we will expect an intense line at 511keV in a suitable detection system, in presence of high energy photons and high Z materials (like Pb, or W).

- **Positron annihilation.** Positrons are not stable particles in matter. They interact with electrons in the target material and give back the sum of electron and positron rest masses ( $2m_e c^2$ ) as emission of electromagnetic radiation by the process called "annihilation".

Positrons slow-down in matter by transferring their energy through atomic ionization and excitation. While slowing-down, in-flight annihilation with a bound electron may occur (half-life 0.5 ns). But, when positron energy goes below about 10 eV, annihilation becomes more probable: the positron can bind with an electron extracted from an atom, by generating an unstable system, the "positronium", whose binding energy is half the one of an hydrogen atom and its radius twice the Bohr radius.

Positronium may be generated into two states, depending on the electron and positron spins. In a para-positronium (p-Ps), the two particle spins are anti-parallel and positronium is in a singlet state with angular momentum  $J=0\hbar$ . The p-Ps half-life in vacuo is 0.125 ns. In an ortho-positronium (o-Ps), spins are parallel and therefore a triplet state is generated with angular momentum  $J=1\hbar$ . The o-Ps half-life in vacuo is 140 ns.

The positron from an o-Ps state can annihilate with another electron from an atom in matter, hence conversion processes from o-Ps to p-Ps may occur, reducing the o-Ps half-life down to a few nanoseconds. By assuming that the kinetic energy of para-positronium ( $E_{\text{rest}}=2m_e c^2$ ) is negligible, since the photon angular momentum is  $J=0\hbar$ , energy and momentum conservation require that two opposing photons are

emitted from annihilation, each one with energy  $h\nu = m_e c^2$ . On the other hand, o-Ps annihilation occurs by emitting an odd number of photons: typically, annihilation occurs through the emission of three photons space by  $120^\circ$  one each other with  $\frac{1022}{3}$  keV in energy.

To sum up, Figure 1.12 resumes the probability of occurrence of photon interaction with matter. Photons are a fundamental part of this thesis, and it is important to have in mind which is the most probable interaction in the considered energy range. Moreover, the geometry of the simulation study will include components (target, collimator, detector) with strong differences in the atomic number, so that the most likely effect may vary from different components.

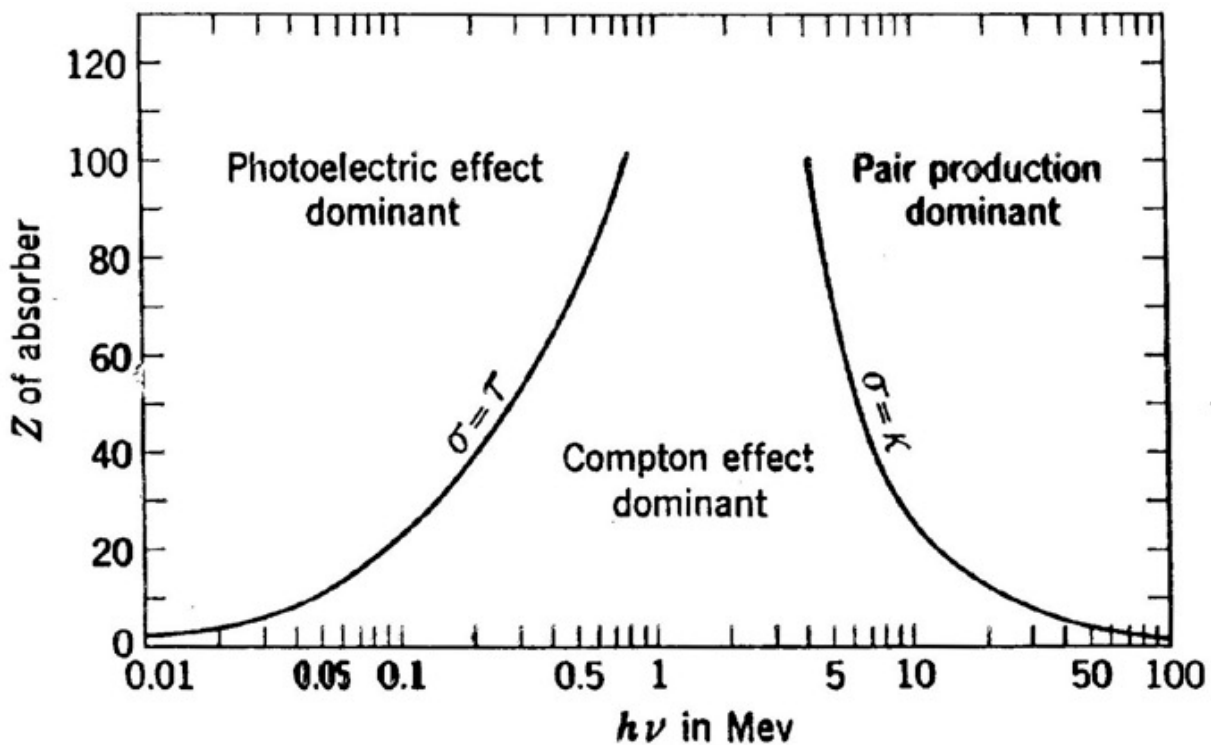


Figure 1.12: Relative probability of the three major types of gamma-ray interaction in matter as function of the impinging photon energy and the target atomic number. Figure from Ref. [54].

## 1.5. Radiation detection

The detection of ionizing radiation by the scintillation light produced in certain materials is one of the oldest techniques on record. The scintillation process remains one of the most useful methods available for the detection and spectroscopy of a wide assortment of

radiations. The ideal scintillation material should possess the following properties:

1. It should convert the kinetic energy of charged particles into detectable light with a high scintillation efficiency.
2. This conversion should be linear and the light yield should be proportional to deposited energy over as wide a range as possible.
3. The medium should be transparent to the wavelength of its own emission for good light collection.
4. The decay time of the induced luminescence should be short so that fast signal pulses can be generated.
5. The material should be of good optical quality and subject to manufacture in sizes large enough to be of interest as a practical detector.
6. Its index of refraction should be near that of glass ( $\sim 1.5$ ) to permit efficient coupling of the scintillation light to a photomultiplier tube or other light sensor.

No material simultaneously meets all these criteria, and the choice of a particular scintillator is always a compromise among these and other factors. The most widely applied scintillators include the inorganic alkali halide crystals, of which sodium iodide is the favorite, and organic based liquids and plastics. The inorganics tend to have the best light output and linearity, but with several exceptions are relatively slow in their response time. Organic scintillators are generally faster but yield less light. The intended application also has a major influence on scintillator choice. The high Z-value of the constituents and high density of inorganic crystals favor their choice for gamma-ray spectroscopy, whereas organics are often preferred for beta spectroscopy and fast neutron detection (because of their hydrogen content).

### 1.5.1. Inorganic scintillators: LYSO

Scintillation is found in a wide variety of both organic and inorganic materials and is defined as the efficient conversion of incident ionizing particles into an optical response of fast rise and/or decay times. This ability has made scintillators the cornerstone of room temperature ionizing radiation spectroscopy and imaging. A high-performing family of scintillation detectors is the cerium-doped lutetium orthosilicate  $\text{Lu}_{2-x}\text{Y}_x\text{SiO}_5:\text{Ce}$  (LYSO:Ce) crystals developed in the '90s, which have an exceptional high photon-emission rate. This material has enabled the development of the current generation of time-of-flight positron emission tomography (TOF-PET) clinical scanners and is of high interest for

reconstruction-free TOF-PET imaging and online monitoring of adaptive proton therapy enabled by its high photon-emission rate [67] [29].

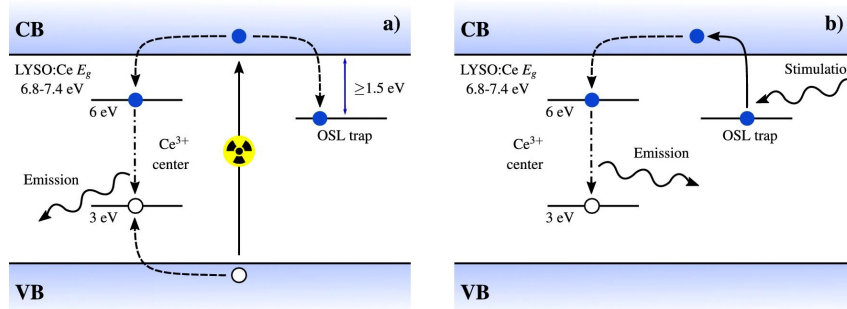


Figure 1.13: Band gap diagram for LYSO:Ce. (a) illustrates the scintillation process: Ionizing radiation generates electrons and holes, which are subsequently trapped by  $Ce^{3+}$  centers with a life time of  $\sim 40$ ns and give rise to prompt light emission. (b) A fraction of electrons are stored in auxiliary OSL traps, which are readout on request through the same  $Ce^{3+}$  centers using optical stimulation. Solid lines illustrate excitations, dashed lines illustrate capture processes, dash-dotted lines illustrate radiative decays and wavy lines illustrate optical photons.

Figure 1.13a [47] illustrates the scintillation process within the band gap of a LYSO:Ce crystals. Upon interaction with ionizing radiation, electrons are excited across the band gap, where they generate secondary electrons and holes that thermalize to the lowest available energy in their respective bands. Energy from the thermalized charge carriers is transferred to the  $Ce^{3+}$  centers energetically located within the  $6.8 \div 7.4$  eV band-gap of the insulating inorganic matrix [132]. The  $Ce^{3+}$  centers function as recombination centers through a  $5d-4f$  optical transition characterized by a decay time around 40 ns, and are responsible for the scintillation in this material, producing around 40000 optical photons per deposited MeV. As illustrated in Figure 1.13a, capture to another more long-lived trap state also occurs, allowing for storage of a fraction of the excited electrons. Electrons captured and trapped in this metastable trap state can be excited post-irradiation using low-energy optical stimulation allowing for radiative recombination through the  $Ce^{3+}$  centers as illustrated in Figure 1.13b. Such optically stimulated luminescence (OSL) provides a method to interrogate the OSL-traps and assess the number of trapped electrons, as this correlates directly with the number of emitted OSL-photons.

Previous studies (such as [33]) of lutetium orthosilicate (LYSO) compounds using films, powders, and structurally defective cerium doped single crystals have reported OSL properties in these compounds. These studies agree on the stability and dose-linearity of OSL in the investigated LYSO compounds and the relevance of this energy-storage mecha-

nism in radiation dosimetry. However, the study and application of OSL in commercial LYSO:Ce samples used for current TOF-PET imaging remains to be explored [47].

### 1.5.2. Silicon photomultipliers

The visible photons generated by a scintillation crystal must be detected and converted into detectable electronic signal by a photo-sensor. For this, the principle of the photoelectric effect is exploited to convert photons into photoelectrons that can be amplified by the sensor and read out by the subsequent signal processing electronics.

When coupling the photo-sensor to the scintillation crystal, it is crucial to match the optical index of refraction between these two components to avoid losing light at the surface interface. There are different types of photo-sensors, whose main requirement is to provide a high photon detection efficiency (PDE) in the wavelength region of interest. The only technology of silicon photomultipliers is shown here, as they are an important component in the discussion of Chapter 4.

Silicon photomultipliers (SiPM) are today more and more popular as an alternative to standard photomultiplier tubes (PMTs), mainly because of their insensitivity to magnetic fields, compactness, and low voltage bias. A SiPM is a silicon-based photodetector that uses multiple APD (Avalanche Photodiode) micropixels operating in Geiger mode. These are called Single Photon Avalanche Diode (SPAD). To build up one SiPM module, several hundreds, up to a few thousands, of these micro-cells are connected, sharing the same bias and ground, in a parallel circuit. The pixels are electrically decoupled from each other by polysilicon resistors located on the same substrate (Figure 1.14).

SiPMs operates in reverse bias, specifically slightly above the breakdown voltage ( $V_{bd}$ ), that is the bias for which the electrical field strength, in the depletion region, is sufficient to create a Geiger discharge. Entering the photodiode in Geiger mode, photons generate a self-sustaining avalanche current which is, then, quenched and reset by use of either passive elements or active quenching circuits. A SPAD of the SiPM produces a pulse signal when it detects one photon. The sum of all SPADs signals will generate the output of the SiPM, whose gain, mainly determined by the overvoltage, is typically in the range of  $10^5$  to  $10^7$ . On the surface of a SiPM pixel an anti-reflective layer is added to optimize the efficiency of the detector by increasing the number of photons reaching the depletion region at the pn-junction.

In the following, I will introduce two of most important figures of merit of SiPMs.

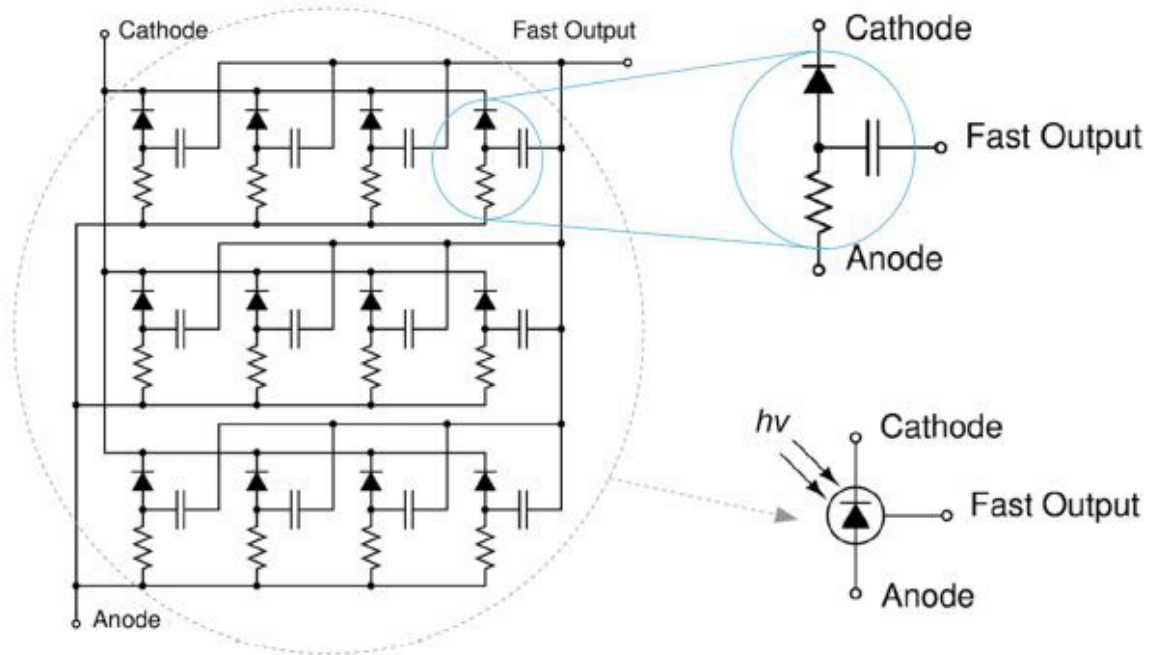


Figure 1.14: Simplified schematic representation of a silicon photomultiplier circuit. Each micro-cell consists of a SPAD, quench resistor and fast output capacitor.

## Photon Detection Efficiency

The Photon Detection Efficiency (PDE) is defined as the probability for an impinging photon to produce an electron-hole pair. This quantity can be expressed as the joint probability for a photon to impinge on the active area of the photodetector, to be absorbed in silicon, and to effectively trigger the avalanche, as shown in Eq. 1.10:

$$PDE(\lambda, V) = \eta(\lambda) \times P(V) \times FF \quad (1.10)$$

where  $\eta$  is the quantum efficiency of silicon,  $P$  is the avalanche initiation probability and  $FF$  is the fill factor of the device, a geometrical parameter defined as the ratio between the active area and the overall area of a micro-cell. The PDE, thus, indirectly depends on the wavelength,  $\lambda$ , and on the overvoltage that goes to the SiPM. Typical values can be considered around 40% and 50%.

The dead area is mainly attributable to the quenching resistor and guard rings. Increasing the size of the cell for the same dimensions of quenching resistor, the fill factor improves, as the relative weight of the dead area reduces; but a larger active area leads to a larger depletion capacitance, hence to a slower response of the device. Moreover, in SiPM of the same overall size, it is true that the larger the cells the lower the total number of

them, which brings to a decrease of the dynamic range. Therefore, a trade-off must be considered during electronics design and the optimal condition must be found to obtain the best performances for the target application.

The quantum efficiency is the probability for an impinging photon to be absorbed in the medium, generating an electron-hole pair. So, being related to the promotion of valence electrons into the conduction band, it is dependent on the wavelength of the impinging photon and on the absorption material, which is silicon in the present case. To properly absorb the incident light, the material must be sufficiently thick. The quantum efficiency can reach values as high as 98% by means of proper anti-reflecting coating layers deposited over the SiPM active area.

Finally, the triggering probability depends on the capability of a carrier to trigger an avalanche and can be expressed as in Eq. 1.11 [82]:

$$P = P_e + P_h + P_e \times P_h \quad (1.11)$$

where  $P_e$  and  $P_h$  are, respectively, the probability to trigger an avalanche for an electron and a hole.

Being related to the electric field in the depletion region,  $P$  is a function of the SiPM bias voltage. In silicon  $P_e > P_h$ , but the respective probabilities also depend on the position of generation of the electron-hole pair. The electron avalanche triggering probability is maximized if the electron is generated at the limit of the depletion region, so that the electric field will accelerate the electron for the longest possible time.

## Dynamic range

SiPMs are constituted by an array of elementary micro-cells. The maximum signal provided by a SiPM photodetector corresponds to the case in which all the cells are triggered, while the minimum signal consists in an output of a single cell.

The detection of photons is a statistical process, based on the probability of detecting a certain number of photons by a limited number of sensitive micro-cells. Therefore, the output signal of a SiPM is influenced by the statistical fluctuations that more than one photon hit the same cell. The average number of firing micro-cells  $N_{fired}$  as a function of the number of impinging photons  $N_{ph}$ , given a certain number of cells  $N_{cell}$  and PDE can be computed as [85]:

$$N_{fired} = N_{cell} \left( 1 - e^{-\frac{PDE \times N_{ph}}{N_{cell}}} \right) \quad (1.12)$$

According to Eq. 1.12, the output signal of a photodetector is proportional to the number of impinging photons only when  $N_{ph} \ll N_{cell}$ . Conversely, saturation effects are explained for a number of photons comparable to the number of the micro-cells, when the probability of multiple photons hitting the same cell becomes significant. In Figure 1.15, experimental results obtained for three SiPMs with different number of cells are shown. The number of fired micro-cells is represented as a function of the generated photoelectrons, found by knowing the average number of impinging photons and the PDE of the SiPMs.

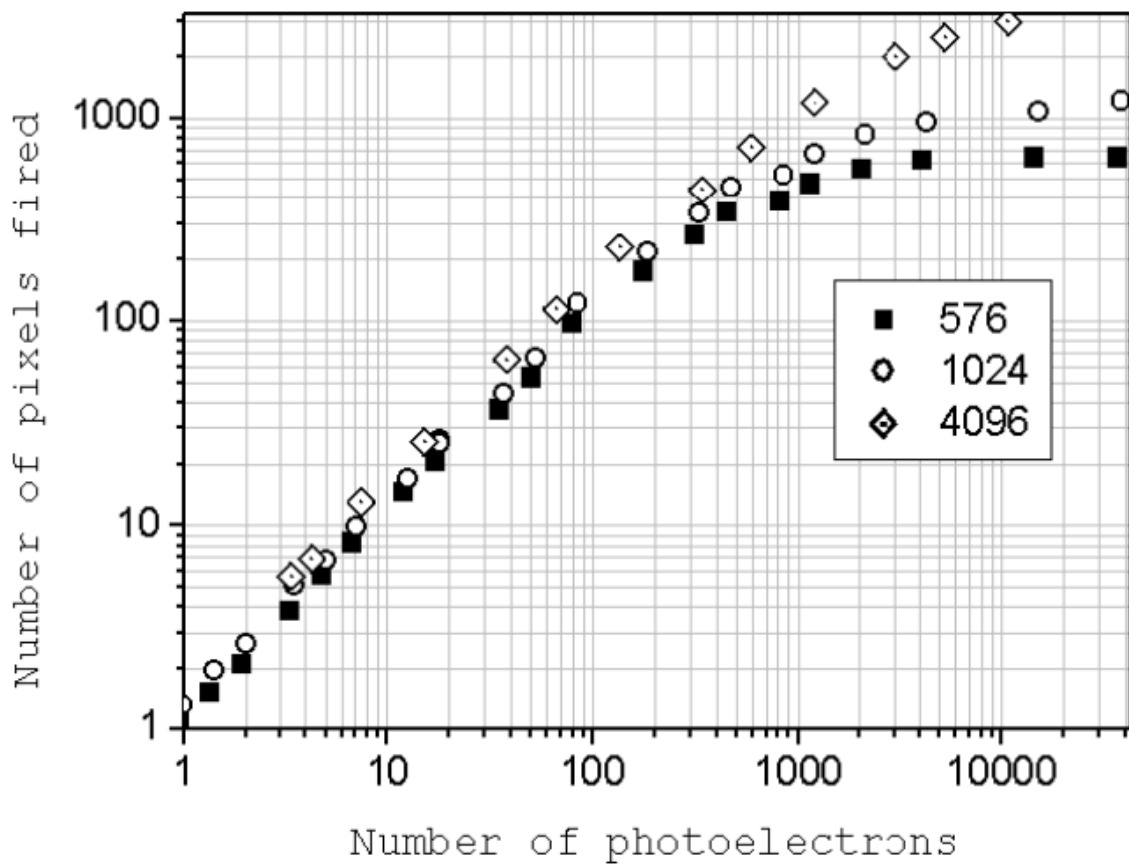


Figure 1.15: The SiPM output signal saturation for three different numbers of micro-cells, namely 576, 1024 and 4096. The number of fired micro-cells is proportional to the number of impinging photons when this is well below the total number of cells; when this is not the case, saturation of the output signal shows up. Figure from Ref. [85].



## 2 | Range uncertainties in particle therapy

*In this chapter, I will tackle the problem of range uncertainties in particle therapy, which is one of the main limiting factor for the spreading of this technology. The most promising solutions will also be shown.*

*The first section will be devoted to report the definition of range, to describe the sources of range uncertainties and their influence on hadrontherapy.*

*Then, in the second section, I will classify in three categories the methods under investigation to reduce the impact of the range uncertainties on particle therapy.*

*Finally, last section will focus on the family of techniques which exploits prompt gammas generated by the interaction with matter of the therapeutic ion beam. Not only that, but I will also consider the detection systems for range monitoring in particle therapy that are already reported in literature, showing their performances, needs and challenges.*

### 2.1. Introduction

The main challenge in radiotherapy is how to deliver high dose to the tumor region, while minimizing the irradiation of healthy tissue. Proton and carbon ion beams offer the possibility to accurately target tumors thanks to their rising dose distribution culminating at the Bragg peak. However, treatments with charged particles are more sensitive to uncertainties than conventional radiotherapy, because of their steep dose profile. Hence, to avoid under-dosage to the tumor and unwanted dose to healthy tissues, large safety margins around the tumor are employed, and/or robustly optimized conservative treatment plans are used. Anyway, this way may not be the optimal for patient and may limit the beneficial effects of charged particle therapy.

### 2.1.1. Definition of range

Ideally, the range of a charged hadron is defined at the position where the dose has decrease of the 80% of the maximum dose, i.e., at distal dose fall-off [38]. The reason behind this definition is that, considering a monoenergetic proton beam, the 80% fall-off position coincides with the mean projected range, which in turn is defined as the position where the 50% of protons have stopped.

Due to range straggling, not all charged hadrons of the same energy have the same range. It makes sense, though, to define the range for a beam resulting in a SOBP.

The range definition is not unique: in most proton facilities, the prescribed range is defined at the 90% fall-off position in water.

### 2.1.2. Sources of uncertainty

Let us now dig into the causes of range uncertainty, which can be divided into two main categories:

- **Dose calculation errors.** The development of a treatment plan based on a specialized computerized tomography (CT) scan is a routine in radiation therapy. From a CT scan, which can also be coupled with other diagnostic images, clinicians determine the tumor location and plan the parameters of daily treatment (such as the number of beams, the beam directions, the dose to deliver). An important part of the planning process involves the computation of both the exact range of each beam, needed to cover the whole tumor volume, and the associated beam energy to produce the exact range. However, the accuracy of these calculations is compromised by three main sources.

First, artifacts in the planning CT scan, such as uncertainty in highly inhomogeneous patient tissues, or in presence of metallic implants. Secondly, limitations can be found in the algorithms used to determine the beam dose delivery rates in different tissues. The estimation of the tissue relative stopping powers is deduced from X-ray CT, converting photon attenuation coefficients to ion stopping powers: CT numbers, represented in Hounsfield units (HU), reflect the relative X-ray attenuation of a given tissue in comparison to the attenuation in water. To get ion ranges for treatment preparation, HU must first be converted to relative stopping powers, where calibration curves are created using elaborate algorithms that involve inevitable uncertainties; then, the actual conversion is based on the chemical structure of the material [107].

Lastly, another kind of uncertainty is often associated to the RBE: proton therapy

has been focused on the use of a generalized RBE, but its dependencies on various physical and biological properties are not considered. This uncertainty can be quantified as few millimeters in biological range [87].

- **Gap between treatment preparation and delivery.** During the treatment delivery, the patient must be immobilized and positioned on the treatment couch in a way that matches the CT simulation. Due to setup errors, patient's mispositioning is the most significant source of uncertainty, especially when treating areas with high density heterogeneities and patient non-planar surfaces along the beam direction. A second not negligible uncertainty is given by internal organ motion, such as breathing.

The positioning and alignment for each treatment session is performed by means of a robotic couch and onboard CT imaging systems to ensure that the patient's bone and soft-tissue landmarks are aligned as they were at the time of treatment planning; however, the exact reproduction of the planned patient alignment is not possible, for several reasons: first, the on-board imaging systems are limited in contrast and resolution; then, over the course of radiotherapy, which can last 30 days or more, patient anatomy can change due to weight loss, tumor shrinkage, or normal tissue swelling; finally, patients may wiggle, cough, scratch an itch, or shift position during the several minutes between the end of the alignment process and the conclusion of the daily treatment.

Table 2.1 resumes the sources of uncertainty in particle therapy, based on a systematic study and classification done by Paganetti [88], in which is also highlighted the importance of Monte Carlo techniques that can reduce the range uncertainty by several millimeters.

### 2.1.3. Range uncertainty influence on particle therapy

Particle range uncertainty needs to be considered when designing the treatment plan with practical consequences that compromise part of the benefit of particle therapy. Thus, to mitigate possible side-effects and to ensure that the clinical target volume is effectively irradiated with the prescribed dose, safety margins are applied in the Planning Treatment Volume (PTV).

A typical margin is chosen to be 2mm plus 3.5% of the beam range, so for deep-seated tumors, 1cm or more of tissue might be added to the treated target volume [88]. In Figure 2.1, safety margins applied to the total uncertainty are reported for different therapy centers.

Nonetheless, adding range-uncertainty margins and using sub-optimal beam arrange-

Table 2.1: Estimated proton range uncertainties and their sources and the potential of Monte Carlo for reducing the uncertainty. The estimations are average numbers based on 1.5 standard deviations. Extreme cases, such as lung treatments, might show bigger uncertainties.

Range uncertainty source in patients	Range uncertainty without Monte Carlo	Range uncertainty with Monte Carlo
<b>Independent of dose calculation</b>		
Measurement uncertainty in water for commissioning	$\pm 0.3\text{mm}$	$\pm 0.3\text{mm}$
Compensator design	$\pm 0.2\text{mm}$	$\pm 0.2\text{mm}$
Beam reproducibility	$\pm 0.2\text{mm}$	$\pm 0.2\text{mm}$
Patient setup	$\pm 0.7\text{mm}$	$\pm 0.7\text{mm}$
<b>Dose calculation</b>		
Biology (always positive) (a)	$+ \sim 0.8\%$	$+ \sim 0.8\%$
CT imaging and calibration	$\pm 0.5\%$	$\pm 0.5\%$
CT conversion to tissue (excluding I-values)	$\pm 0.5\%$	$\pm 0.2\%$
CT grid size	$\pm 0.3\%$	$\pm 0.3\%$
Mean excitation energy (I-values) in tissues	$\pm 1.5\%$	$\pm 1.5\%$
Range degradation; complex inhomogeneities	$-0.70\%$	$\pm 0.1\%$
Range degradation; local lateral inhomogeneities (b)	$\pm 2.5\%$	$\pm 0.1\%$
Total (excluding a,b)	$2.7\% + 1.2\text{mm}$	$2.4\% + 1.2\text{mm}$
Total (excluding a)	$4.6\% + 1.2\text{mm}$	$2.4\% + 1.2\text{mm}$

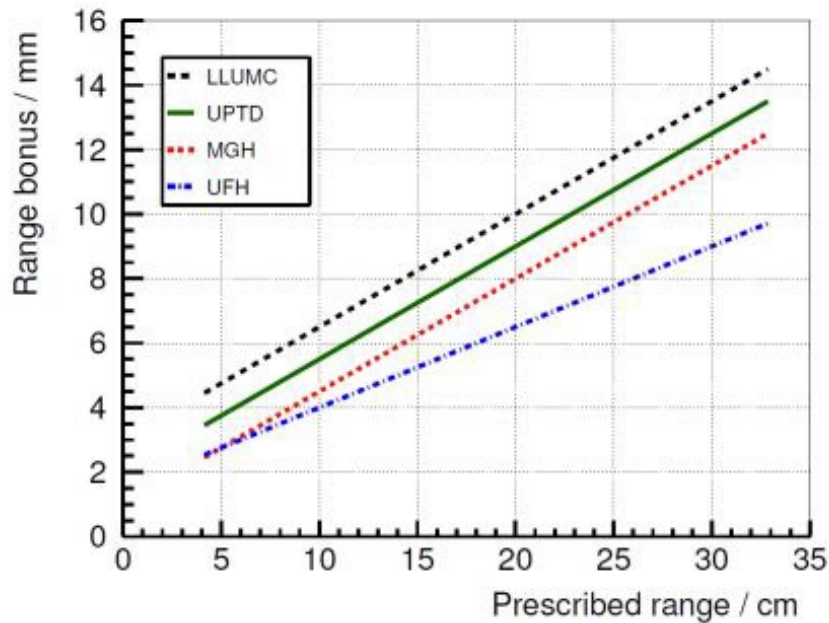


Figure 2.1: Safety margins used in different clinical proton therapy facilities: (3.5% + 3mm) at Loma Linda University Medical Center (LLUMC), (3.5% + 2mm) at Universitäts Protonen Therapie Dresden (UPTD), (3.5% + 1mm) at Massachusetts General Hospital (MGH) and (2.5% + 1.5mm) at University of Florida Health Proton Therapy Institute (UFH). The term "range bonus" refers to the margin applied to the specified range to ensure maximum tumor coverage even in the case of an undershoot. Under certain treatment scenarios, these centers may use larger margins.

ments, it often means losing the intrinsic advantage of charged hadrons depth-dose distribution.

A promising strategy that could limit beam-range uncertainty are either techniques able to directly image the beam as it passes through the patient during treatment, or techniques in which the secondary particles whose emission is correlated with the beam range are properly detected. These methods would allow clinicians to verify that the treatment fraction is delivered to cancer as planned. For instance, the detection and imaging of secondary emissions outside the patient can provide a real-time visualization of the dose distribution inside the patient. For this, many different methods for *in-vivo* range verification have been proposed and explored over the last years. The following section will be devoted to an overview of state-of-the-art range verification methods.

## 2.2. Range Verification methods

To start, let us classify the various solutions under investigation to limit range uncertainty in particle therapy. We can distinguish three distinct categories: first, methods that aim at reducing uncertainties before treatment delivery; then, methods that operate during delivery monitoring the treatment; lastly, the so-called post-treatment verification methods.

Next subsections will summarize the most promising solutions in particle therapy and we will be helped by the huge work done by J. Smeets in his PhD thesis [111].

### 2.2.1. Pre-treatment reduction of uncertainties

Reducing the different sources of range uncertainties to a minimum before treatment delivery is of course the best practice. Among the different techniques, we can find:

- **Robust planning.** Approach that aims at reducing uncertainties on the treatment outcome. It takes range uncertainties into account at the treatment planning stage to mitigate their potential consequences at the treatment delivery stage. Efforts are focused on avoiding significant under-dosage of the target volume or excessive exposition of a critical healthy structure, because of range uncertainties. This is commonly integrated by medical physicists who apply such principles as field patching, safety margins, the use of lateral penumbra rather than the distal one to avoid critical structures, etc. These principles also need to be integrated in treatment plan optimization software.
- **Proton radiography.** Range uncertainties could be efficiently reduced by perform-

ing a proton radiography before the delivery of every treatment fraction, using the therapeutic beam. A proton beam of sufficient energy to exit the patient would give the possibility to measure the proton residual energy thanks to a position-sensitive range telescope. Comparing the results to the computed predictions, physicists could identify, for instance, setup errors and evolution of the cancer size causing under- or overshoot.

Ideally, the treatment would even be planned using proton computed tomography data, which would eliminate the present ambiguity in the conversion to proton stopping powers of CT numbers from classical X-ray CT scans. Even though radiography and computed tomography via proton and heavy ion beams have been investigated by different groups who confirmed the great potential of these approaches [97], they are not yet used in clinical routine as both technical and financial difficulties are still faced.

- **Dual-energy X-ray computed tomography.** Dual-energy X-ray computed tomography is another option to reduce range uncertainties due to the ambiguity in the conversion of CT numbers to proton stopping powers.

A dual-energy CT scanner uses two X-ray energy spectra, generated at a different voltage. The two sets of data and their energy dependence give the possibility to simultaneously retrieve both the density and the effective atomic number  $Z$  of the tissues. Yang *et al.* already concluded that, for the dual-energy CT, the combination of two X-ray spectra, one in the kV range, plus one in the MV range, could be more effective in reducing errors than the more conventional combination of two kV X-ray spectra. The reasons are to be found in random noise and beam hardening effects [137].

- **Radioactive probing beam.** For carbon ion therapy, a very efficient concept is the use of a radioactive beam. The stable  $^{12}\text{C}$  isotope can be replaced by the positron emitting isotopes, such as  $^{10}\text{C}$  or  $^{11}\text{C}$ , with similar dose deposition curves. The penetration depth can then be retrieved, as most of the radioactive C-ions will stop at their mean projected range and emit positrons; annihilation photons, escaping the patient will then be detected by a gamma camera.

This was first realized at the Lawrence Berkeley Laboratory in the 80's with a  $^{19}\text{Ne}$  beam and more recently at the Heavy-Ion Medical Accelerator (HIMAC) in Chiba with beams of  $^{10}\text{C}$  and  $^{11}\text{C}$  [51]. Iseki *et al.* did not find  $^{11}\text{C}$  to be advantageous because its long half-life (20.4min) results in low count rate and the measurement is blurred by other positron emitters produced along the incident beam tracks. Thanks to a shorter half-life (19.3s), beams of  $^{10}\text{C}$  were preferred despite a lower production

yield and deeper maximum range of the emitted positrons (up to 9.2mm for positrons of  $^{10}\text{C}$  and up to 4.2mm for  $^{11}\text{C}$ ). Measurements were conducted with a  $^{10}\text{C}$  beam of  $345.8 \frac{\text{MeV}}{u}$  average energy, incident a PMMA target (PolyMethyl MethAcrylate,  $(\text{C}_5\text{H}_8\text{O}_2)_n$ ,  $1.19 \frac{\text{g}}{\text{cm}^3}$ ) and a pair of Anger-type scintillation detectors operating in time coincidence were used to collect the signal. The data analysis revealed that the range could be measured with an uncertainty as low as 0.3mm for  $2.7 \times 10^5$  ions implanted, corresponding to a biological dose of only 9.6cGyE (gray-equivalent dose taking into account a relative biological effectiveness of 4.1) [46].

### 2.2.2. Real-time treatment monitoring methods

Following the optimization of sources of the treatment planning uncertainties, real-time monitoring would offer powerful feedback during treatment delivery: the treatment could be corrected before the whole fraction is delivered, if the measured range does not match the prescribed one. Different approaches have been investigated and can be distinguished in direct methods, based on direct measurement of the depth-dose distribution, and indirect methods, which take advantage of the secondary emission from the patient during treatment.

#### Time resolved diode dosimetry

An example of direct method is the "time resolved diode dosimetry". This is an extremely promising approach for quality control with passive scattering delivery systems. It is principally meant for prostate treatments where diodes are introduced in the rectum with a rectal balloon as illustrated in Figure 2.2. This method could also be applied for other treatments provided that diodes can be inserted in a body cavity.

Intra-cavity dosimeters are already used for quality control in conventional photon and electron radiotherapy. One specific difficulty for proton therapy is the flatness of the dose distribution before and beyond the BP, as the dosimeter cannot be placed right at the dose distal fall-off. If the dosimeter is placed before the BP in the plateau of the SOBP, the dose distribution will give no indication on the residual range of protons. Beyond the BP, the dose is almost zero and it cannot be accurately related to the average distance of proton maximum penetration depth.

In the work of Lu, a solution to this difficulty is given by taking advantage of the time-dependence of the signal measured by the diodes exposed to the plateau of a SOBP [70]. Passively scattered proton systems deliver SOBP by intercepting the incident beam with a rotating wheel composed of segments of variable thickness: the range modulator. The

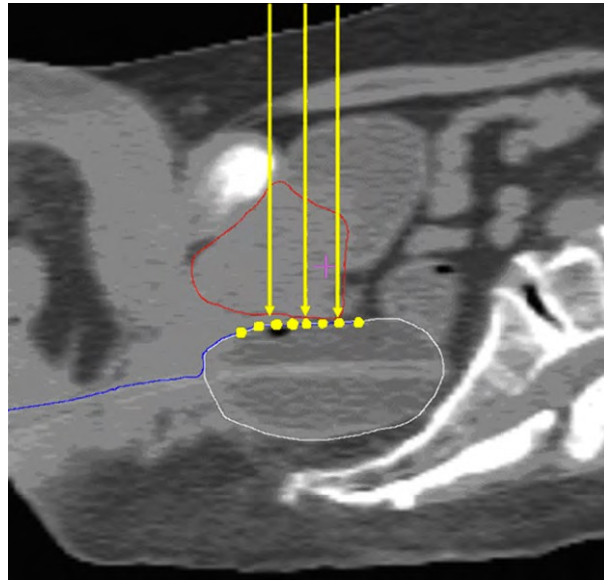


Figure 2.2: Schematic view of an *in-vivo* range verification with diode detectors (yellow dots) for a patient whose prostate (red delineation) is treated by an anterior proton field (yellow arrows) with an endorectal balloon (white curve). Figure from Ref. [116].

different segments of the wheel cause the degradation of the beam producing different BP depths. As a consequence, the dose rate measured by a diode at a fixed depth varies periodically as a function of time: even if the diode measures the same total dose at all depths of the SOBP dose plateau, the time-dependence is different and thus encodes the residual range.

This method could be applied before and during a prostate treatment. When the patient is positioned, a probing beam would first deliver a low dose (less than 1cGy) with a deeper range than prescribed so that the diodes are exposed in the plateau of the SOBP. The millisecond dose-time dependencies measured by the diodes are compared to a database of reference dose-time functions (obtained by calibration measurements, or via Monte Carlo simulations) to deduce the residual range at these points. If this residual range does not match the expected value within a specified margin (let us say less than 1mm), the range is adjusted. After this pre-treatment verification, the diodes measure the rectal dose continuously during the actual treatment delivery with the adjusted prescription range: protons are supposed to stop before the diodes to spare the anterior rectal wall. If for any reason this rectum dose gets too high, the treatment could be immediately interrupted, and resumed after a new range adjustment.

## Range verification via prompt gammas

After collisions with charged hadrons many nuclei of the patient tissue are left excited and decay by emitting neutrons or prompt gammas very quickly ( $10^{-19}$  to  $10^{-9}$  s), as explained in section 1.4). Prompt gammas have a wide energy spectrum with a few characteristic rays of the nuclei that are present or produced in the target. Reproducing data from Kozlovsky *et al.* [59], the cross section of gamma ray lines from proton reactions with  $^{12}\text{C}$  and  $^{16}\text{O}$  are plotted in Figure 2.3. It is expected that the most intense peaks will be the 4.44MeV due to  $^{16}\text{O}$  and  $^{12}\text{C}$ ; the 6.129MeV, 6.916MeV and 7.115MeV due to  $^{16}\text{O}$ , and the 0.718MeV due to  $^{12}\text{C}$ .

In 2003, Stichelbaut and Jongen suggested that these PGs, leaving the patient, could be used to deduce the particle range [115]. As PGs are produced along the proton tracks, the path of a pencil beam within the patient could be imaged as a line source by an adequate gamma camera: this technique was then called Prompt Gamma Imaging (PGI). Thanks to Monte Carlo simulations, they predicted that the prompt gamma emission profile should be correlated with the depth-dose distribution produced by the primary beam. Prompt emission of high-energy gamma rays provides a direct and instantaneous signature of the beam range in matter.

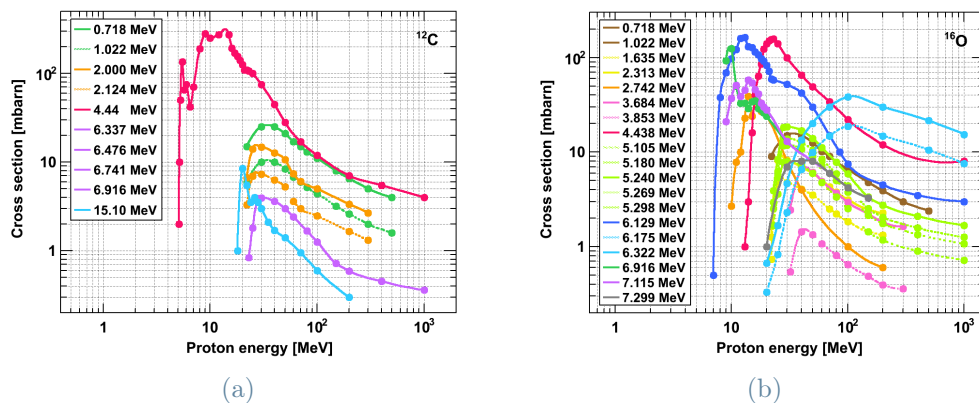


Figure 2.3: Gamma production cross sections from proton reactions with  $^{12}\text{C}$  (a) and  $^{16}\text{O}$  (b). Cross sections are drawn in the same color when they use the same data multiplied by different factors. For  $^{12}\text{C}$ , the 4.438MeV and 4.444MeV peaks are merged as the 4.44MeV peak. Figure from Ref. [111].

The use of PG detection to monitor proton range has been already experimentally verified (e.g., [76] [118]). As classical cameras used in nuclear medicine were not adapted to detect high energy gammas, in the presence of an important neutron background, a knife-edge camera was developed by IBA in collaboration with Politecnico di Milano and XGLab [94], has been applied for the first time clinically for a treatment of a head and neck

tumor [102], with measured inter-fractional global range variations of the order of  $\pm 2$ mm. Developments of Compton cameras for PG measurements are also ongoing (see, e.g., [120] [114] [32]) although not yet with clinical trials. Prompt-gamma spectroscopy (PGS) [126] [125] and timing (PGT) [37], based respectively on energy and timing (time-of-flight) measurements, are also under development and have been recently tested [19] [130] [72].

### Proton vertex imaging

Interaction vertex imaging (IVI) is a proposed method which exploits prompt secondary protons and other light ions (secondary particles) to reconstruct the positions of nuclear reactions (the "interaction vertices") inside the patient body in heavy ion therapy [40]. These protons are mostly emitted after fragmentation reactions of the beam and tissue along the trajectory of the beam. In an ideal implementation, the reconstruction of interaction vertices could take place during the treatment to provide fast feedback on BP position [44].

### Secondary electron bremsstrahlung for carbon ion therapy

To assure in-beam quality of treatment applications, several techniques for therapeutic carbon-ion beams are worldwide under study. A beam-monitoring technique which involves the measurement of low-energy secondary electron bremsstrahlung (SEB), was proposed and is under active investigation for therapeutic carbon beam applications [136]. The potential of this approach for beam-trajectory imaging using a pinhole camera was investigated using therapeutic proton beams and the trajectories of these monochromatic beams were appropriately imaged [2].

This technique has the potential to significantly improve overall sensitivity, for the two following reasons. The emission intensity of SEB is larger than that of high-energy PG rays and of positron-annihilation gamma rays (including very short-lived nuclides). Secondly, collimators and detectors can be easily fabricated for low-energy photons, so that simple and high-sensitivity imaging devices can be easily realized.

### Positron emission tomography

Positron emission tomography (PET) imaging has been the most extensively investigated method for noninvasive, *in-vivo* visualization of the delivered ion treatment. PET exploits the detection of the coincident, anti-parallel 511 keV photon pairs following the annihilation of the positron emitted in the  $\beta^+$  decay of neutron deficient nuclei. There are three operational modalities for PET-based verification in hadron therapy, the first of which is

used during treatment and will be followed in this paragraph; the other two are classified as post treatment techniques and will be faced in the next subsection 2.2.3.

The operational modality exploited during the ion treatment is also known as "In-beam PET" which has been already clinically applied at GSI [26] and at CNAO [6]. A limitation of this method is that the signal can be considered intrinsically delayed with respect to the beam delivery, following the half-life of  $\sim 2 \div 20$  min of the most abundant positron emitting reaction products. Hence, In-beam PET does not offer proper real-time monitoring. Another limit is represented by biological washout and organ motion, which affect PET excellent accuracy [79] [56] [41]. Nevertheless, researchers are working to develop both modern in-beam PET instrumentation tailored to *in-vivo* range verification and computer-assisted tools for adjusting the treatment plan when PET detects an offset between the delivered and intended beam range.

At GSI in Darmstadt, a dedicated in-beam PET system was integrated in the treatment unit to perform in-beam acquisitions during carbon ion therapy [30]. The scanner is composed of two heads rather than a full ring not to limit patient positioning and handling. For more than 440 patients, acquisitions were started with the irradiation and stopped 40s after the ion beam.

PET is still the most used technique for verifying range in hadron therapy, especially for offline acquisition, for which commercial scanners are already available. State-of-the-art on-line PET detectors are just entering the phase of clinical evaluation with the most modern form of scanned proton beam delivery. At the combined proton and carbon ion therapy facility of CNAO in Italy, a dual-head PET scanner based on modern scintillation crystals (Lutetium fine silicate) and photosensors (multi-pixel photon counters) is used to dynamically (every  $\approx 10$  s) reconstruct the irradiation induced activity during treatment, with very promising initial clinical results [29] [93].

### 2.2.3. Post treatment verification methods

Post treatment verification methods estimate the beam penetration depth after the treatment delivery. This information is still very valuable for three reasons. First, if an under- or overshoot is detected after a treatment fraction, the cause can be investigated before next fraction is delivered; moreover, positive range verification after the first fraction is enough to discard the risk related to uncertainties in the conversion of CT numbers. Statistics on treatment outcomes are more reliable if we can distinguish treatments that were delivered as planned from others that were affected by unacceptable range errors. At last, the information obtained improves our knowledge about range uncertainties, which is of capital importance to describe relevant scenarios in the robust planning approach.

## Positron emission tomography

PET was already encountered as useful tool for real-time range verification. In-room and off-line PET, instead, are classified as post-treatment verification methods. The idea is the same: to image  $\beta^+$  emitting isotope distributions with a PET/CT scanner. Cross sections for the reactions of proton and carbon ion beams with abundant tissue nuclei are reproduced in Table 2.2 from Ref. [30].

**Table 2.2:** Partial cross sections  $\sigma$  of the reactions of proton and carbon ion beams with the most abundant nuclei of human tissue. From Ref. [111].

		Projectile $^{12}\text{C}$		Projectile $^1\text{H}$	
Target atom	Positron emitting fragment	$\sigma$ (mb)	E ( $\frac{\text{MeV}}{u}$ )	$\sigma$ (mb)	E (MeV)
$^{12}\text{C}$	$^{11}\text{C}$	$55.97 \pm 4.06$	250	$45 \pm 2$	150
	$^{10}\text{C}$	$5.33 \pm 0.81$	250	$2.6 \pm 0.3$	155
$^{16}\text{O}$	$^{15}\text{O}$	$28.3 \pm 0.2$	290	$38 \pm 4$	155
	$^{11}\text{C}$	$16.3 \pm 0.2$	290	$11 \pm 1$	155
	$^{10}\text{C}$	$1.65 \pm 0.02$	290	$1 \pm 0.2$	155
	$^{13}\text{N}$	$6.09 \pm 0.09$	290	$4.5 \pm 1$	155
$^{14}\text{N}$	$^{13}\text{N}$	$13.3 \pm 0.4$	600	$8.3 \pm 0.5$	155
	$^{11}\text{C}$	$27.5 \pm 0.4$	600	$15 \pm 1$	155
	$^{10}\text{C}$	$2.1 \pm 0.2$	600	$1.6 \pm 0.3$	155

Thus, acquisition can be realized (in-room) with a PET scanner in the treatment room, or simply offline, in which case the patient is quickly transported to a PET facility close to the therapy center where the treatment was given.

These methods have their own advantages and disadvantages. In-room and real-time acquisition avoid delay between treatment and imaging, requiring shorter data acquisition and, consequently, obtaining less wash-out, better statistics and less motion, but they reduce patient throughput in the treatment room [55]. A disadvantage of real-time/online imaging systems is also the exposure to PGs, neutrons, and scattered radiations.

Offline PET allows to use commercially available and dedicated PET or PET/CT scanners, initially designed for nuclear medicine imaging. Just after the treatment, the patient is moved in a nearby room, where the scanner is found. This can result in delays of up to 30 minutes between treatment and scan, with implications on the reconstructed PET images due to signal losses from the short-lived  $\beta^+$  emitters.

Another disadvantage is the occurrence of biological washout during patient transport, which lowers activity in the target zone: the impact on relative activity distribution can cause image blurring, especially in well-perfused areas like muscles. The differing half-

lives of the related isotopes cause variations in emission rates for different tissues over time.

In-room PET adopts a stand-alone PET scanner placed in the treatment room. It can be considered a compromise between in-beam and off-line PET. The cost of a stand-alone PET scanner is significantly lower compared to the installation of a PET system integrated into the beam delivery system and there is no geometrical constraint associated with the beam delivery and the patient positioning. Moreover, there is still a delay between treatment and PET scanning, but it is much shorter than in the offline PET situation so that signal collection from  $^{15}\text{O}$  ( $t_{1/2}=2.04\text{min}$ ) is still possible. Hence, the offline PET complications such as biological washout, repositioning defects, anatomical modifications, and so on are often significantly minimized or removed.

In-room PET can be a cost-effective choice for most hospital-based proton centers that use a cyclotron to generate proton beams, although the time taken for each patient treatment is likely to be longer than for in-beam PET.

PET imaging has been shown in clinical trials to detect beam range inaccuracies in tumors that are at high risk of treatment delivery error, such as deep-seated tumors requiring a long beam range, those located in abdomen or pelvis; tumors positioned among multiple interfaces between bone, soft tissue, and air cavities that complicate beam transmission, like head or neck tumors.

Studies conducted with offline PET/CT after proton therapy at MGH in Boston found that the spatial reproducibility of the measured activity distributions can be as good as 1mm [56]. Unfortunately, range verification with an accuracy of  $1\div 2$  mm is only feasible for few particular positions and tumor sites, namely low-perfused bony structures of the head and the neck patients.

## Magnetic resonance imaging of the vertebral column

Krejcarek *et al.* proposed a very specific post-treatment range verification technique for craniospinal irradiation [63]. After irradiation, the vertebral bone marrow is replaced by fatty marrow, which is visible through magnetic resonance imaging (MRI). Certain tumors of the central nervous system present an important risk of subarachnoid dissemination and metastases along the neuraxis: craniospinal irradiation is prescribed to reduce this risk and proton beams give the opportunity to limit the radiation dose to the bowel, lungs, and heart. Two different approaches are adopted depending on the age of the patient. For adult and adolescent patients who have reached maximal growth, full dose is only prescribed to the thecal sac (surrounding the spinal cord and filled with cerebral spinal

fluid) and exiting nerve roots. But for younger patients, the entire vertebral body must be exposed to the prescription dose to avoid a future asymmetric growth of the vertebrae that would result in an abnormal curvature of the vertebral column.

Gensheimer *et al.* (2010) studied 10 patients who had completed vertebral growth and thus received a dose distribution planned to fall off in the vertebrae. Two or three postero-anterior fields were delivered in 1.8 to 2.0 Gy fractions for a total spine dose ranging from 23.4 to 50.4 Gy(RBE) (weighted by the relative biological effectiveness of 1.1) [34]. Using spine MRIs, they investigated proton range errors and found an average over-penetration in 8 patients and an average under-penetration in 2 patients. Range errors were of the order of a few millimeters.

At last, the weakness of the method is that the fatty marrow replacement is only visible after the end of the treatment. In case of over- or undershoot, the proton range cannot be corrected before the whole treatment is delivered.

## 2.3. Prompt-gamma monitoring in charged particle therapy

### 2.3.1. Prompt gamma techniques

Figure 2.4 show the longitudinal distributions of prompt secondary radiation emitted from a phantom composed by a homogeneous water cylinder, which are the outputs of Monte Carlo simulations reported in [64].

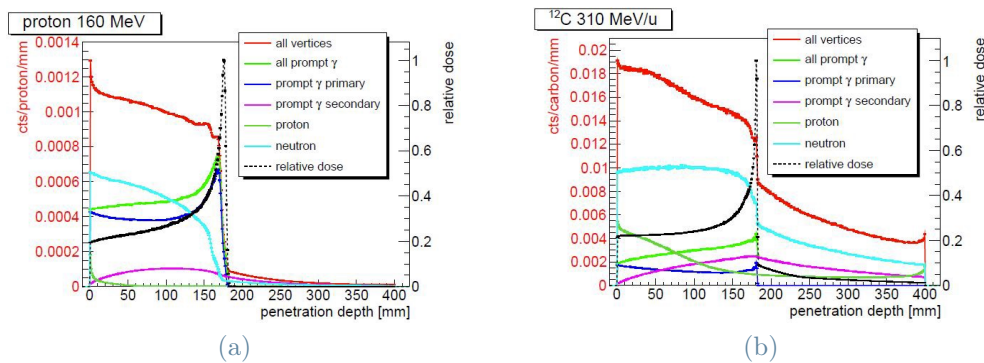


Figure 2.4: (a) Emission vertices of secondaries with energies larger than 1MeV emerging from a water target (cylinder with 15cm diameter, 40cm length) irradiated by a 160MeV proton beam; (b) emission vertices of secondaries with energies larger than 1MeV emerging from a water target (cylinder with 15cm diameter, 40cm length) irradiated by 310  $\frac{\text{MeV}}{u}$  carbon ion beam. Figures from Ref. [64].

The cylinder was irradiated axially by protons (Figure 2.4a ) and carbon ions (Figure 2.4b), whose energies were chosen to get the same range in both cases.

For both incident beams, what can be inferred is that the prompt-gamma generation profiles are well correlated to the particle range. If one regards the sharpness and position of the emission fall-off in the Bragg peak region, the correlation is better for carbon ions than for protons. However, note that secondary particles generate, in turn, ternary ones during secondary reactions, outside the primary beam path, and possibly beyond the Bragg peak. As expected, the secondary-interaction production is more pronounced for carbon than proton beams, the yield of secondary vertices increases with penetration depth, and starts to decrease beyond the Bragg peak.

## Prompt Gamma Imaging

The correlation between longitudinal PG emission and dose profiles makes it possible to use 1D PG imaging (PGI) as a tool to retrieve the Bragg peak position, for a given beam energy and pencil beam spot distribution in case of active beam delivery, provided that the available statistics is sufficient. The first gamma camera suitable for proton range measurement at clinical beam currents was presented in [94], where a dedicated slit-collimator design was chosen, and several parameters needed for PGI were optimized. The measurements demonstrated the ability of the camera to detect millimetric shifts of the target for high levels of dose. Acquired profiles and simulations were compared and showed good agreement, especially at 100 MeV: a precision of 4mm ( $2\sigma$ ) was achieved for  $0.5 \times 10^8$ ,  $1.4 \times 10^8$  and  $3.4 \times 10^8$  protons at 100MeV, 160MeV and 230MeV, respectively.

Richter *et al.* reported the first clinical application of a PG-based range verification system, in which the aforementioned knife-edge slit camera was used, after being continuously improved [102]. In this work, the inter-fractional analysis of the PGI measurements revealed minimal variation in PG profiles of  $\pm 2$  mm in the sum profiles, consistent with control CT-based evaluation of dosimetric variations: an important finding as first clinical application. The authors compared the inter-fractional variation with the absolute range uncertainty assumed in their clinic, i.e., 6.7mm specifically for that beam energy (3.5% of the nominal range plus 2mm) and the inter-fractional range variation analysis confirmed that the random contribution of the range uncertainty was well within the allowed range variation window.

However, they also were conscious that it was too early to draw final conclusions on the sensitivity of the method from a single clinical application. A systematic correlation was concluded to be possible between measured PG profiles and anatomical changes visible in control CT, on the condition of more clinical data acquirement, in the near future, by

the continuation of clinical study.

One year later, Xie *et al.* reported the first clinical results and value assessment of prompt gamma imaging for *in-vivo* proton range verification in pencil beam scanning mode. The treatment was delivered with a PBS-dedicated nozzle on a fixed/horizontal beam line [135]. The patient treatment plan consisted of 3 equally weighted fields, which were composed of 17 layers from 160 to 101 MeV, 17 layers from 155 to 100 MeV, and 18 layers from 160 to 101 MeV. PGI was performed twice per week during the final 3 weeks of treatment.

In this study, the absolute amplitude of the average shift resulted as 1 to 2 mm, which was smaller than the fixed distal margin of 5mm clinically applied. The average shift variation of 1.9mm, at 2 sigma over 6 days for the 3 fields, was essentially attributed to the uncertainty on the camera positioning: the variation was larger between fractions than between layers within a given acquisition. Hence, they concluded that the retrieved shift was sensitive to the camera positioning.

Another important point that they considered is linked to tissue composition. In this first clinical PGI application in PBS mode the proton beams travelled through nearly homogeneous tissues, which made the spot-by-spot analysis and aggregation straightforward; in a more complex target with greater tissue in-homogeneity, instead, they suggested range mixing and spot selection for spot aggregation, in the analysis.

Finally, they proposed further optimizations for the precision retrieval. First, they considered the strongest weakness, camera positioning, proposing a real-time camera position monitoring system to increase the overall precision; secondly, a nozzle-mounted range shifter was suggested since it would allow the camera to be positioned closer to the beam, increasing the detection statistics of PG signal; third, spot aggregation was recognized as way to further improve the camera precision, especially in the low-dose spot regions, with marginally compromised lateral resolution. Anyway, the aggregation of neighboring spots brought to some doubts, because it would promote the range mixing in case of lateral heterogeneities and, therefore, decrease the ability to identify local range shifts.

To conclude, all the studies that were presented concerned the PGI technique in proton therapy. In this workflow, carbon ions are not considered, and this represents a clear gap in knowledge, which is the reason behind this present thesis. Starting from a simulation study, it could be interesting to investigate this technique for heavy ions too.

## Prompt Gamma Spectroscopy

The path of Prompt Gamma Spectroscopy (PGS) started with a simulation study [126] about prompt gamma-ray emission, which resulted to be dominated by proton-induced

nuclear reactions on  $^{12}\text{C}$ ,  $^{16}\text{O}$  and  $^{14}\text{N}$  when proton therapy is concerned. Knowledge of these reactions, in presence of limited experimental data, has been the key to an accurate simulation of potential range verification methods employing prompt gammas, especially in the design of detection systems.

PGS has several benefits for range verification: as the discrete energies correspond to specific nuclear transitions, the magnitude of  $\gamma$ -lines have unique correlations with the proton energy and can be directly related to nuclear reaction cross sections; then, the quantification of these discrete lines also enables elemental analysis of tissue in the beam path, providing a better prediction of PG-ray yields.

In 2013, Verburg *et al.* presented experimental results of a novel prompt gamma-ray detector for proton beam range verification [127]. They adopted a detection system composed by an actively shielded cerium-doped lanthanum(III) bromide scintillator, coupled to a digital data acquisition system. The acquisition was synchronized to the cyclotron radio frequency to separate the prompt gamma-ray signals from the neutron background. The detector was designed to provide high energy resolution with an effective reduction of background events to resolve discrete proton-induced prompt gamma lines.

One year later, in a different publication [125], J.M. Verburg and J. Seco proposed for the first time the PGS method for proton range verification, exploiting spectroscopy of proton-induced PG-rays: in this work, the range of proton beams was obtained by directly relating measured PG spectra with models of proton-nuclear interactions.

The proposed range verification method was enabled by quantitative measurements of PG emissions from specific nuclear reactions: discrete gamma lines were resolved and proton- and neutron-induced contributions were separated. Derived from measured differential cross sections, models were used to simultaneously determine the proton range, the oxygen and carbon concentrations of the irradiated tissue (hence, the method is robust in the presence of tissue with an unknown composition).

Furthermore, their results showed that it was possible to accurately verify the proton range using a single detector acquiring data at a fixed position, during the delivery of a few distal pencil beams. Although a single detector is necessary, they proposed an idea dealing with the main problem of range verification, statistics: multiple detectors to improve statistical precision and to obtain simultaneous measurements at different positions along the beam path, which may be advantageous to ensure coverage of the entire field when the distal surface of the tumor is highly curved.

Finally, they concluded reporting an interesting result of the experimental study. The achieved statistical precision with their small-scale prototype detector was about 1mm (standard deviation) for absolute range verification and 0.4mm for relative verification

based on five pencil-beams delivering  $5 \times 10^8$  protons, which is the typical number for an irradiation spill [13].

Taking the heritage of previous works, Hueso-González *et al.* developed and evaluated a new full-scale clinical prototype detection system for PGS [42]. They reported a mean statistical precision of 1.1mm at a 95% confidence level, delivering a dose of 0.9Gy and aggregating data from several pencil beam spots. Hence, results showed that proton range verification with 1 millimeter precision was achievable in phantoms under clinically realistic conditions.

For what concern helium ions, it is worth to mention the work done by Dal Bello *et al.*, in which the first experimental results were presented for prompt gamma spectroscopy applied to  $^4\text{He}$  beams at clinically relevant intensities and energies. The optimized detector based on  $\text{CeBr}_3$  surrounded by BGO has been proven to provide an excellent performance, especially for the low-energy component of the prompt-gamma energy spectrum [19].

To conclude, in 2020, Dal Bello *et al.* presented a small-scale prototype for absolute range verification of ion beams at synchrotron-based facilities [20]. The study was conducted using clinically relevant beam energies and intensities using PGS technique, which was already demonstrated for proton beams accelerated at a cyclotron-based facility [42]. The authors extended the applicability of the technique to a synchrotron-based facility, for heavier ions up to  $^{16}\text{O}$  beams.

Using the small-scale prototype described in Ref. [20], they demonstrated for the first time the possibility to measure the absolute BP position for  $^{12}\text{C}$  beams accelerated by a synchrotron: a submillimetric precision was found for the BP position measurement in the experimental setup.

## Prompt Gamma Timing

The introduction of time-of-flight (TOF) techniques improved the signal to noise ratio due to the separation of PG-rays from those produced in reactions of neutrons with the target tissue, or with surrounding materials. Testa *et al.* reported a series of experiments with carbon ions, in which they investigated whether a collimated set-up detecting single photons by means of TOF measurements could also be used at the typical high energies of ion therapy. Moreover, the possibility to extract the same information from fast neutrons was also considered. The conclusion, based on the results of the described experiments, was that single photon emission tomography, including a collimated set-up and TOF measurements, could constitute a promising method to control, in-situ and in real-time, the dose distribution during ion therapy treatments [119].

Starting from this idea, Golnik *et al.* proposed a novel method for on-line range verification based on PG-ray timing (PGT) spectroscopy [37]. The concept behind PGT utilizes an elementary physical effect: therapy particles move very fast penetrating a tissue, but they need a measurable time from entering the patient's body until they reach the target volume, i.e., the region of maximum energy deposition. This particle transit time is about  $1\div 2$  ns in case of protons with a range of  $5\div 20$  cm. PG-rays may be emitted along the particle track in tissue, while a detection system, situated outside of the target, shall measure the time difference between the time when particle bunch passes a reference plane and the arrival time of the corresponding PG-ray at the detector. This time difference incorporates the particle transit time through the material  $t_p$ , as well as the flight time  $t_{\gamma TOF}$  of the PG-ray to the detector (Figure 2.5). The authors defined this time distribution as PG-ray time (PGT) spectrum.

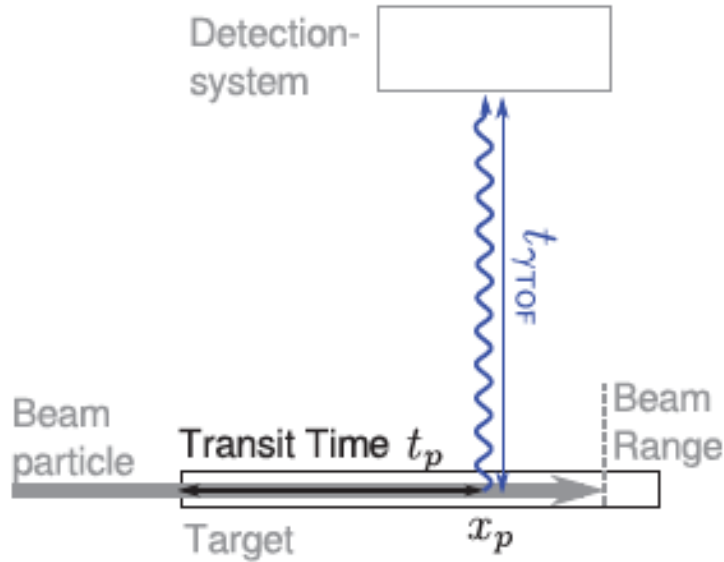


Figure 2.5: A particle beam of given initial energy irradiates a target and, consequently, a PG-ray is emitted along the beam track at position  $x_p$ . The time  $t_p$  has elapsed from the entrance of particle into the target up to the gamma emission, which is assumed to be instantaneous. The PG-ray time of flight,  $t_{\gamma TOF}$ , is necessary for the radiation to reach the detector, which is situated outside of the target and measures the whole time difference between the time of the particle entering the target and the arrival time of the PG-ray at the detector. The measured distribution is denoted as PG-ray timing (PGT) spectrum. Figure from Ref. [37]

The particle transit time relation,  $t_p(x_p)$ , is range dependent: particles with longer ranges have to travel longer paths, which implies wider times. Also, longer periods of (potential)

PG-ray emission and, on average, delayed emission times are found in the corresponding PGT spectrum, which produce a broader peak as well as a distinct peak shift. Hence, PGT statistical moments, such as the distribution mean ( $\mu$ ) and the standard deviation ( $\sigma$ ), contain information on the particle transit time.

The PGT technique was then explored in first proof-of-principle experiments at clinical proton therapy facilities but far off treatment conditions [95]. Later, a clinically applicable hardware solution for energy and timing spectroscopy of PG rays at high throughput rates was developed by Pausch *et al.* [91].

Finally, Werner *et al.* questioned whether it was possible to detect few-millimeter range deviations of individual proton pencil beams under clinical beam conditions by means of PGT using detection units as described in Ref. [91]. An experiment was performed in the gantry treatment room of the University Proton Therapy Dresden (UPTD), whose results encouraged further experiments in more realistic clinical conditions [130].

### 2.3.2. Detection camera prototypes

PET, developed in the 1990s, was the first method of *in-vivo* range verification that has ever been successfully applied in patient treatments with particle beams. As already mentioned, its main disadvantage is the signal delay of seconds to minutes in correspondence with the respective decay times of the  $\beta^+$  emitters. In-beam PET measurements, however, could only be performed with a scanner that does not interfere with the beam and is not blinded by the PG-ray flash during dose delivery. Even if dedicated instrumentation was available, the prolonged measurement after beam delivery compromised the clinical workflow and reduced the patient throughput. That is why applications of in-beam PET are restricted to clinical studies performed with non-commercial scanners, usually built by research teams [26] [93].

The economically more efficient solution fitting with the mentioned constraints, namely measurements with a commercial PET scanner after moving the patient to another room, suffers from much lower statistics and the consecutive disturbance of the primary correlation between  $\beta^+$  activity distribution and spatial dose deposition in the patient due to biological washout by metabolism, blood, and lymph circulation [56]. That is why many research groups have focused their efforts on a promising alternative, namely range verification based on PGs.

To detect this hard radiation, imaging systems with passive collimation by a pinhole, a linear slit, or multiple slits, have been investigated. The following subsections will be dedicated to the review of the most important detection systems reported in literature.

## Pinhole concept

An example of pinhole passive collimated system can be found in Ref. [110]. Seo *et al.* designed a PG scanning system, called "Prompt Gamma Scanner", by means of a series of Monte Carlo simulation studies.

The system was designed to keep high-energy neutrons away from the scintillation detector. For this, a layer of titanium hydride ( $TiH_2$ ) was first used to moderate high-energy neutrons. Then, borated carbon ( $B_4C$ ) was inserted to capture the low-energy neutrons from the paraffin layer. Also, lead was used to absorb the secondary gamma radiation generated from neutron capture reactions in the borated carbon layer. Figure 2.6 shows a schematic view of the designed scanner, together with the movement system.

The system has a small hole behind the scintillator for neutrons to escape without interactions with the scanning system. An empty space is also intentionally provided around the scintillation detector to reduce the neutron background while keeping the PG field at the same level.

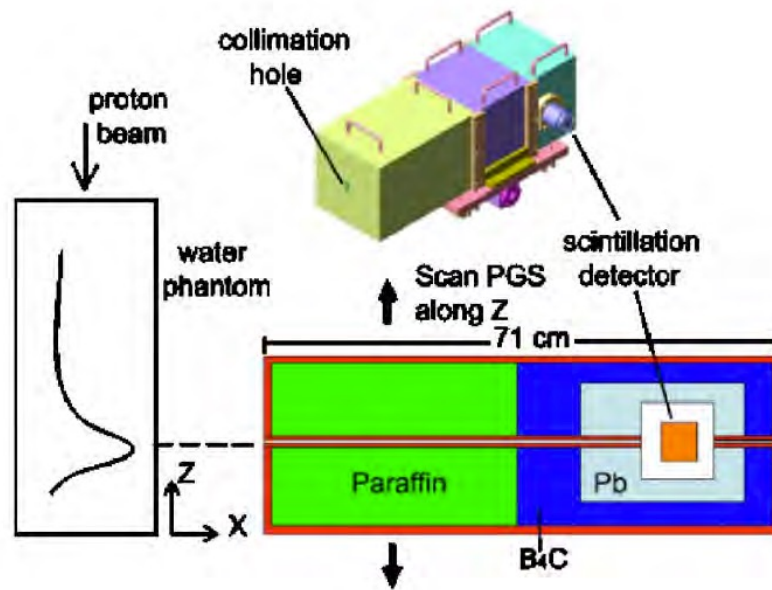


Figure 2.6: An example of a passive collimated system for PG detection is depicted. The collimation hole gives the name to this particular set up, which is mounted on a moving system. Figure from Ref. [76]

Kim *et al.* pursued an experiment with a 50MeV proton beam impinging on a water target, after optimization through Monte Carlo simulations [53]. The PG-rays were observed adopting a CsI(Tl) scintillation detector placed beyond a pinhole aperture to get the range's endpoint. Unfortunately, the output profiles did not show a clear spatial correlation with the beam particle range. To the author's knowledge, this geometry is no

longer under investigation due to the low counting statistics of PG-rays going through the pinhole aperture.

### Knife-edge slit camera

An example of gamma camera with knife-edge slit was developed based on simulation studies by Smeets [111] and constructed by Perali *et al.* [94] with joint forces between Politecnico di Milano and the company XGlab [134], as part of a project that also included the manufacturer of proton accelerators, the Belgian company IBA [45].

The design was optimized using Monte Carlo simulations and experimentally tested acquiring data with proton pencil beams of 100, 160 and 230 MeV on a PMMA target. In Figure 2.7, a patient irradiation is depicted during a clinical treatment, in which PGs are travelling through the knife-edge collimator and reaching the well-positioned gamma camera. The designed camera was composed by 20 LYSO scintillator slabs ( $4 \times 31.5 \times 100 \text{ mm}^3$  each, mounted in two rows behind the mechanical slit collimator), the photodetector and the readout electronics.

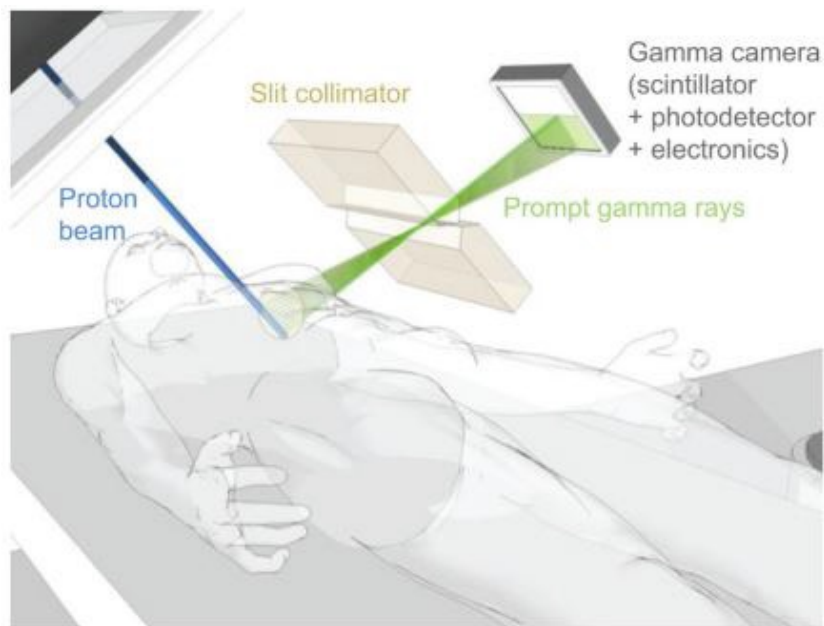


Figure 2.7: The slit camera’s conceptual design: a slit collimation produces a 1D projection of PG emissions along the beam path on a pixelated scintillation detector. Figure from Ref. [94]

At the OncoRay treatment facility [83] of the Universitäts Protonen Therapie Dresden, the camera was first tested by irradiating water and head phantoms with proton pencil-beams of different energies; then, it was applied to real clinical cases [102], demonstrating

that PGI-based range verification is feasible in clinical proton therapy treatments. Further experiments were conducted using both pencil beam scanning and passive double scattering, and it was shown that global shifts of the depth-dose distribution fall-off can be detected with a precision of 1mm for both treatment modalities [81].

### Multi slit camera

In 2008, Min *et al.* conducted a feasibility study of a multi-slit camera, which consisted of an array of collimated scintillators, to detect prompt photons emitted at  $90^\circ$  along the proton track (see Figure 2.8) [77]. As readout sensors, the device employed an array of lead-collimated slots filled with CsI(Tl) scintillators coupled to photodiodes.

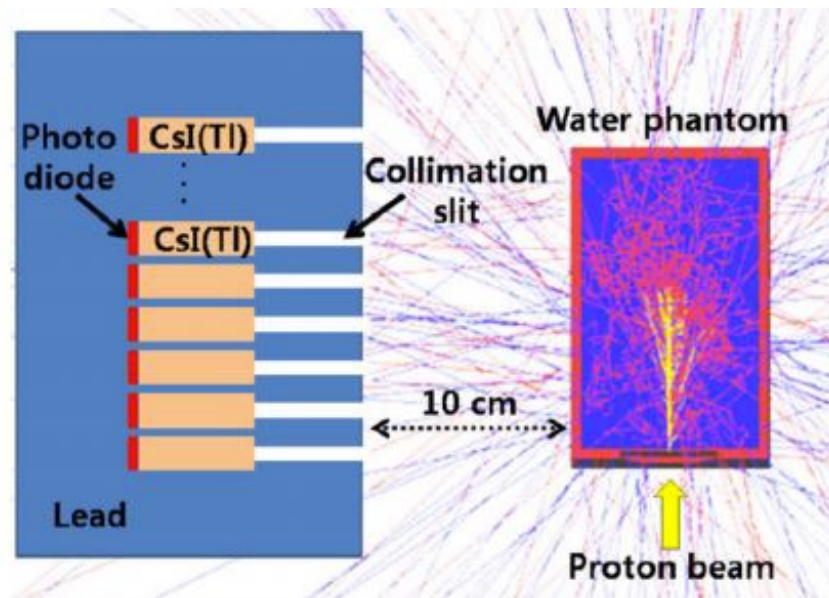


Figure 2.8: Scheme of the array of collimated scintillators to detect PG rays emitted from a water target after proton irradiation. Figure from Ref. [77].

Few years later, Min *et al.* performed an optimization study using the Monte Carlo code MCNPX [78], to determine the optimal size of the scintillator blocks. The tests were realized using a simplified system composed of a single CsI(Tl) scintillator. Proton irradiation of a water target at various beam energies produced the detected rays. An energy window was set in the energy range between 4 and 10MeV and the fall-off of the detection profiles around the Bragg peak was fitted with sigmoidal curves, whose half-values were found to be within 4mm of the distal dose edge (Figure 2.9).

In 2014, Pinto *et al.* published about the optimization of a parallel multi-slit camera [96]. The tool to get their goal were Monte Carlo simulations, whose accuracy was, then, verified with experimental data. In the optimization process, the TOF technique was used

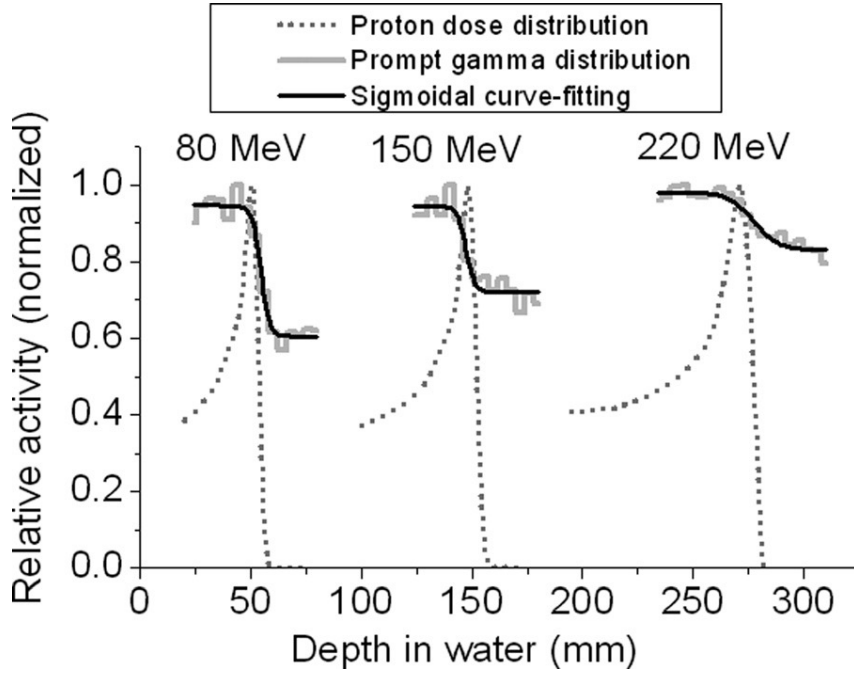


Figure 2.9: PG profiles acquired with a multi-slit camera and fitted with a sigmoidal curve for 80, 150, and 220 MeV proton beams. The measured proton dose distributions are shown for comparison. Figure from Ref. [78].

in order to achieve a better camera performance due to the improved signal-to-background ratio. The detector considered for simulations was a bismuth germanium oxide (BGO) mono-block, while the collimator material was set to be tungsten alloy.

### 2.3.3. Needs and challenges

#### Detector load

In a PBS treatment, spatially resolved range verification means assessing the individual ranges of distinct PBS spots. Range verification systems must, therefore, extract the necessary information from statistics that can be collected during delivery of a single spot, which means in a measuring period of 10ms or less. Furthermore, they must cope with a detector load as defined by the maximum rate of proton delivery in the strongest beam spots, which produce plenty of PG rays with a short time available for a range measurement. The statistics of ‘usable’ PG events per spot is, then, not essentially given by the detector efficiency, but rather by the acceptable detector load, by the achievable system throughput, and finally by the fraction of events passing the respective event filter criteria.

In all PG-based approaches to range verification, the number of registered events is larger

than the number of ‘valid’ or ‘usable’ events. Event filtering is applied to suppress background and to select data comprising the range information. Typically, only events with energy depositions in the detector between 3 and 7 MeV are considered to reduce the radiation noise caused by uncorrelated gamma rays (such as the 511keV annihilation photons, or 2.2MeV gamma ray following neutron capture on  $^1\text{H}$ ). This energy cut rejects about 90% of all events; a number that can be gradually improved by raising the trigger threshold and fully exploiting the detector load capability, i.e., by shifting the bottleneck from electronic throughput to constraints given by the detector physics. However, a noticeable improvement of the statistics can only be achieved by using more detectors. It must be emphasized that the statistics limit is not due to an insufficient PG production per spot, rather to the finite event rates the detectors and electronics are able to process.

## Drivers in design

For the design and construction of a detection system, clear needs are to use pixels of fast and bright scintillator materials distinguished by excellent linearity and negligible internal activity, to provide them with individual Si-based light sensors, and to arrange a reasonable number of such pixels in arrays to form a detection module. The size of the scintillator pixels has to be chosen as a compromise between cost (strongly affected by the number of readout channels) and reasonable granularity. The pixel depth should fit with the absorption length of 4÷5 MeV gamma rays. Hence, considering the active area of available light sensors and an acceptable depth-to-pitch ratio of the scintillator crystals, pixel pitches of 6÷10 mm and depths of 3÷5 cm seem reasonable cornerstones.

The different PG-based techniques have also challenges to overcome. For instance, the energy resolution of pixels must be good enough for PGS, while time resolution is a critical parameter for what concern PGT. Not to mention, the tolerable detector load and gain stability in presence of such energetic radiation: detection systems for PG rays are exposed to frequent, abrupt, irregular load leaps challenging the stability of detectors and electronics.

## Conclusions

So far, the Knife-Edge Slit Camera [94] developed by IBA is the only system that has ever been used for range monitoring in clinical treatments. This camera is capable of detecting local range shifts down to 1÷2 mm. However, the massive and heavy collimator may interfere with the patient’s position and makes integration in a treatment facility an expensive challenge. So, it seems obvious to use active collimation instead. Several groups have tackled the challenge of Compton imaging in the PG energy domain (Ref.

from 16 to 23 in Ref. [92]). Anyway, technical complexity, the huge detector load to be handled, the low fraction of ‘valid’ events and the remaining background after event selection criteria are intrinsic hurdles that cast doubts on the applicability of Compton imaging under therapy conditions, despite punctual encouraging results [22].

# 3 | Monte Carlo feasibility study of a prompt gamma slit camera in carbon ion therapy

*This third chapter constitutes the heart of the current thesis.*

*In the introduction section, I will start from considering the transport problem, focusing on the solution proposed by the Monte Carlo method.*

*The second section will contain a preliminary study devoted at understanding the target secondary emission downstream an irradiation with different beams (protons, He-ions, C-ions). The simulation features will be reported, and the results discussed.*

*The following section will include a Monte Carlo feasibility study for the application of the prompt gamma imaging technique with a slit camera in carbon ion radiation therapy. The possibility to find a correlation between the detection profile in a knife-edge configuration camera and the depth-dose distribution will be explored, in the high neutron background of C-ion irradiation. Successively, I will investigate the sensitivity of the same detection system in retrieving the shifts of the Bragg peak when the target is moved along its longitudinal axis. Finally, a simulation of C-ion irradiation in pencil beam scanning under typical clinical conditions will be reported, both with a planar and inclined entering target surface. The utilized Monte Carlo code, the simulation features and the data analysis will be described in detail, along with the results in separated subsections (respectively, Methods and Results).*

## 3.1. Introduction

### 3.1.1. The transport problem

The transport equation determines the spatial and temporal evolution of a radiation field of several particle species, with different energies and directions in a small volume. To solve it, different strategies can be followed.

Analytical solutions can be found only in restricted geometries and interaction models. Its main drawback is computation time which may be enormous, being really accurate. The spectral method exploits symmetries and appropriate basis functions, but it is not a general solution. Then, the numerical quadrature integration is a general strategy, but inefficient for high-dimensional integrals.

Lastly, Monte Carlo method is a general, efficient solution that can treat arbitrary radiation fields and geometries. It is a stochastic method, which exploits random numbers to simulate ensembles of particle histories governed by known interaction cross sections, tracking them in arbitrary geometries. The simulation outputs are the cumulative contribution of each track to statistical estimator of desired physical observables.

### 3.1.2. Steps in Monte Carlo methods

Monte Carlo simulations are an effective method to compute macroscopic physical quantities, such as energy deposition, displacement per atom, particle fluence, dose, activity, etc.

The radiation transport problem is composed by three key passages:

1. **Radiation source.** Photons, leptons, hadrons, etc. can be chosen and simulated as a monoenergetic beam, or with a custom energy, spatial and angular distribution, according to the faced problem. Depending on the utilized code, particle energy can typically vary from keV to PeV, down to thermal energies for neutrons.
2. **Simulation geometry.** An arbitrary geometry composed by bodies of different materials must be set up, in which transport equation will be solved following the Monte Carlo method.
3. **Propagation in matter.** Best performing and efficient Physics models will describe the interaction between radiation and matter. Moreover, transport thresholds are set in order to stop the tracking of the particle at a given energy.
4. **Scoring.** There are several estimators to score the goal physical quantity inside a Monte Carlo code, closely related to the scientific field of user application. Examples are accelerator design, shielding design, radiation protection, dosimetry, radiation damage, neutronics, and so forth.

## 3.2. Secondary emission from an irradiated phantom: A preliminary study

In this section, the simulation of the secondary emission from a tissue-equivalent target bombarded by particle therapy beams at clinical energies was pursued. It constituted a good starting point of the present thesis, helping to deeply understand the roots of the PGI-technique and to verify some of the most important results, already reported in literature (such as the higher yield of PG production of C-ions over protons, or the quasi-isotropic emission of gamma radiation in contrast to the forward-peaked neutron emission). Moreover, this preliminary study also helped to verify that PG emission is taken into account by MC code FLUKA and the most important PG lines are included in its library. This knowledge was certainly fundamental to compile the input of simulations which constituted the main topic of this thesis and tried to answer the following question: is it feasible to reconsider the application of PGI range verification method for carbon ion radiation therapy?

### 3.2.1. Methods and materials

The numerical simulations were realized using the general purpose Monte Carlo code FLUKA for particle transport (version 4-1.1) [4]. The study compared the secondary emission and the energy deposition of the most considered primary beams in particle therapy, whose energy was selected inside the interval already adopted in clinical treatment (see Section 1.2.1):  $200 \frac{MeV}{u}$  for protons and He-ions,  $385 \frac{MeV}{u}$  for C-ions. These energies were correlated, in a sense that all the beams had the same theoretical particle range of approximately 28cm.

The simulation geometry was composed by a target of tissue equivalent material (tissue soft, ICRP), inside a room filled by air surrounded by walls made of Portland cement. As one can see in Figure 3.1, the target was cut in 16 slices to characterize the secondary emission at different depths along the beam direction, i.e., the z axis. These slices had different dimensions, 3cm in the proximal part of the depth-dose distribution and 1cm around the Bragg peak.

The emission spectra of photons and neutrons following the target irradiation of primary beams were obtained exploiting the FLUKA estimator "USRYIELD", which allowed to score the double differential spectra in energy and solid angle. As shown in Figure 3.2, secondary photons and neutrons were scored only within an emission angle window between  $85^\circ$  and  $95^\circ$  with respect to the beam direction. The perpendicular emission strongly

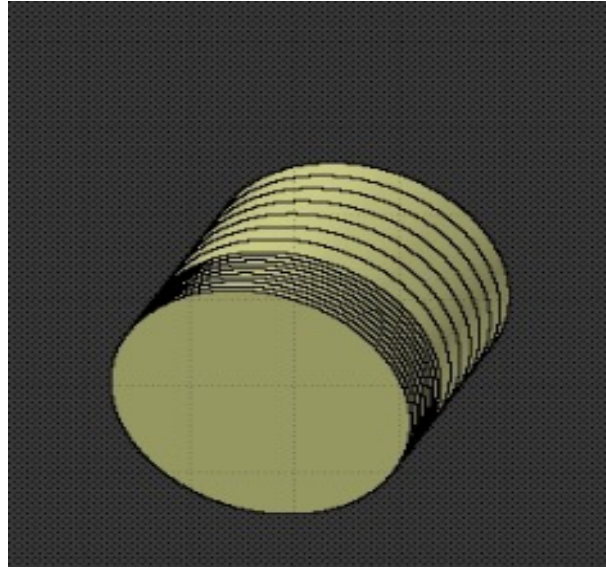


Figure 3.1: Representation of the simulation geometry for the investigation of the secondary emission from a tissue-equivalent target. The target was cut in 16 slices, 7 of which were 3cm-thick while the remaining ones 1cm-thick (around the Bragg peak). The room hosting the target was air-filled and the walls were made of Portland cement.

reduced the neutron component, which is known to be mainly forward peaked. (The positioning of detection systems always exploits this physical feature, to minimize the neutron background with respect to the useful PG signal, which, instead, follows an isotropic emission.)

On other hand, the energy deposition of the beams was scored by the FLUKA estimator "USRBIN", which is a useful tool able to compute many different physical quantities. In particular, one can select a 3D mesh in which the energy deposition of particles inside finite volumes can be scored and then reported in an output file.

Data analysis was performed by the multi-paradigm programming language and numeric computing MATLAB. With a proper code, I imported the output files, analyzed data and, finally, plotted in suitable graph to clearly show the results of simulations.

### 3.2.2. Results and Discussion

In Figure 3.3, one can see the depth-dose distribution curves generated by the energy deposition of the aforementioned beams. As expected, the highest LET was attributed C-ions, followed by He-ions and protons. For carbon and helium, it was also possible to observe a tail in the distal region, which is a consequence of nucleus fragmentation in ion-matter interactions: from theory, fragments have approximately the same velocities and directions of their parent nucleus, but they travel larger paths than the primary ions

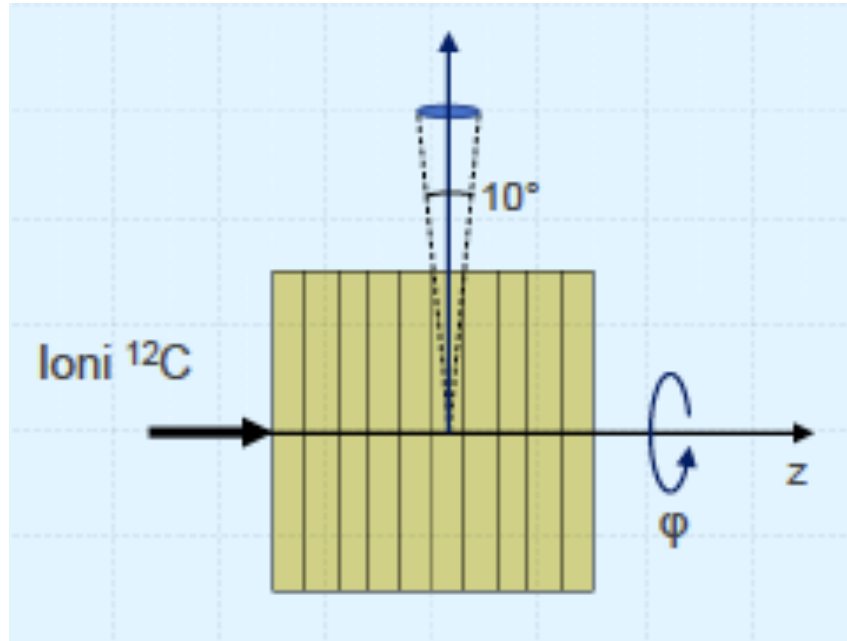


Figure 3.2: Graphical representation of the scoring features for the investigation of secondary emission. Only photons and neutrons emitted within  $85^\circ$  and  $90^\circ$  with respect to the beam axis were scored.

because range scales with  $\frac{A}{Z^2}$ , where A and Z are, respectively, the mass and the atomic number. The tail was more pronounced for C-ions, which produced much more secondary fragments owing to bigger nucleus dimensions than the other simulated particles. However, in the proximal region, the plateau is less intense for C-ions: from theory, the energy deposition before the Bragg peak is strictly related to the multiple Coulomb scattering which goes as  $\sim \frac{1}{Z^2}$ . Hence, carbon ions suffered the lowest proximal dose deposition, while protons had the highest one having the lowest atomic number. As usual, He-ions placed themselves in the middle with respect to proton and C-ion behavior.

As already mentioned and depicted in Figure 3.1, the target was cut into slices around the Bragg peak, which allowed to plot the total number of particles per unit of primary emitted perpendicularly from each slice. Before that, since FLUKA produces double differential spectra, preliminary manipulations on raw data were performed: the counts (or better, particles perpendicularly emitted per unit of primary ion, energy and solid angle) were integrated on the angle and energy, to obtain the spatial profile of the emission along the target axis. In Figure 3.4, the depth-dose distribution (orange) of 385MeV C-ions was compared to the photon (black) and neutron (blue) emission counts (per unit of primary particle). A clear correlation was found between the emitted photon profile and the depth-dose distribution, which would be more visible if only PGs were scored: indeed, around the Bragg peak, the black curve started to fall where the production of

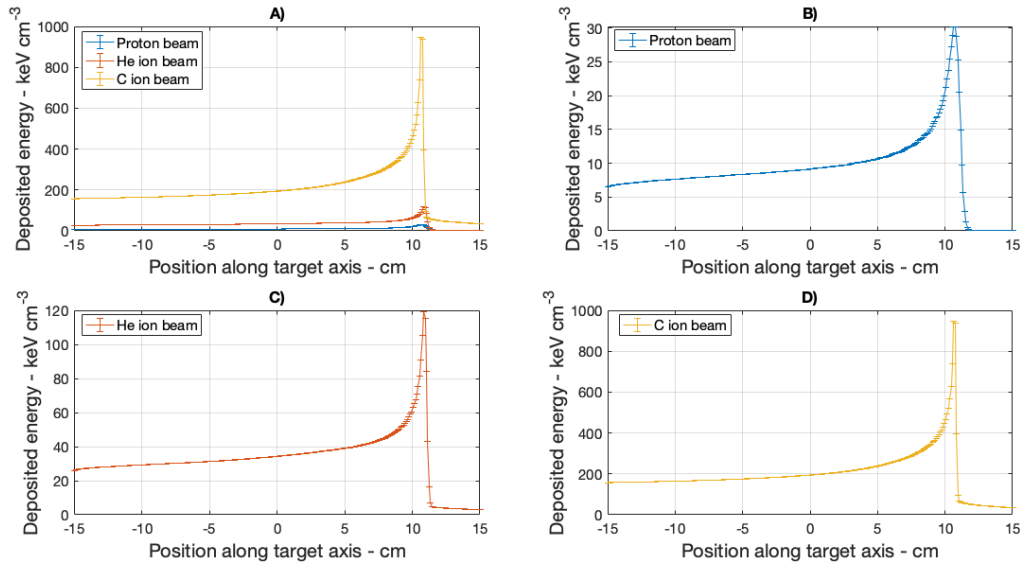


Figure 3.3: The depth-dose distributions, determined by the FLUKA estimator "USRBIN", are here reported. In particular, one can distinguish: **A)** curves from all the beams in a single plot for a direct comparison; **B)**  $200 \frac{MeV}{u}$  proton curve; **C)**  $200 \frac{MeV}{u}$  He-ion curve; **D)**  $385 \frac{MeV}{u}$  C-ion curve.

prompt gammas rapidly suppressed. On the other hand, the neutron profile is almost constant along the target axis. Moreover, less neutron counts per unit of primary particle were scored than photons, because just the normal emission of particles from the target surface was considered (Figure 3.2). The explanation of this result was found in the quasi-isotropic emission of prompt photons, mainly produced in the evaporation stage following the INC when emitting nuclei forget the primary beam direction of irradiation. Instead, the neutron component is dominated by the neutron production in first stage of INC model, when the emission happens in the original direction of the beam.

From Figure 3.5 to Figure 3.8, the double differential spectra versus energy are depicted only for slices around the Bragg peak. Both neutron and photon secondary emissions were scored for the primary beams used in simulations: protons, He-ions, and C-ions. From these graphical results, some important comments were drawn. All the beams produced the same photon lines, more intense as the atomic number increases: the 511keV due to positron annihilation; the 2.2MeV due to neutron capture on hydrogen, which is as expected the most intense for a tissue-equivalent material; the most important lines for PGI, namely:

- The 4.44MeV line due to  $^{16}O$  and  $^{12}C$ .
- The 5.2MeV peak given by the superposition of 4 different lines due to reactions

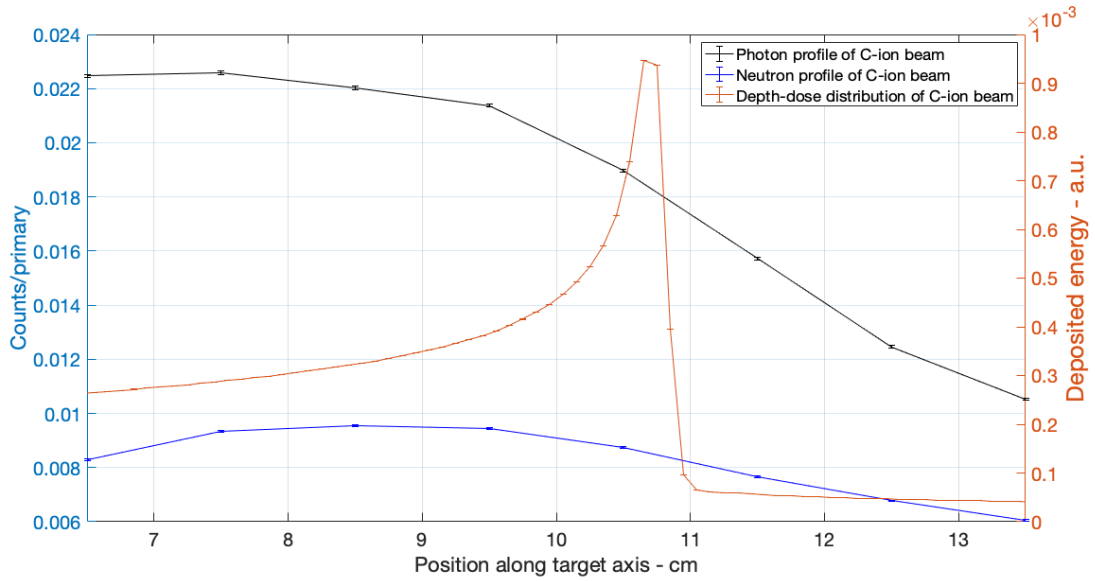


Figure 3.4: From preliminary manipulations, the secondary particle counts per primary following C-ion irradiation are summed for each slice from the 8<sup>th</sup> to the 16<sup>th</sup>. The photon (black) and neutron (blue) profiles are reported over the depth-dose curve.

with  $^{16}\text{O}$ .

- The 6.129MeV line due to  $^{16}\text{O}$ .

Moreover, the Bragg peak placed in the 12<sup>th</sup> slice and the photon counts slightly increased till 12<sup>th</sup> slice, where they started to decrease heavily up to the 16<sup>th</sup> (to have a clear reference point, take a look at 4.4MeV peak). In this observation, the correlation between BP and PGs is found.

For what concern neutrons, lethargy plots were reported, a natural choice to show both the thermal peak and the one centered at 10MeV due to neutron emission during the de-excitation stage at the end of INC (physically described by the Fermi break-up model, Section 1.4). The 10MeV peak decreases from the 12<sup>th</sup> till the 16<sup>th</sup> slice and shifts at lower energies as the slice number increases. The thermal peak follows the same behavior for what concern intensity, which continuously decreases till the 16<sup>th</sup> slice, but the peak center results to be more stable.

### 3.3. Feasibility study on the application of PGI technique in CIRT

### 3| Monte Carlo feasibility study of a prompt gamma slit camera in carbon ion therapy

76

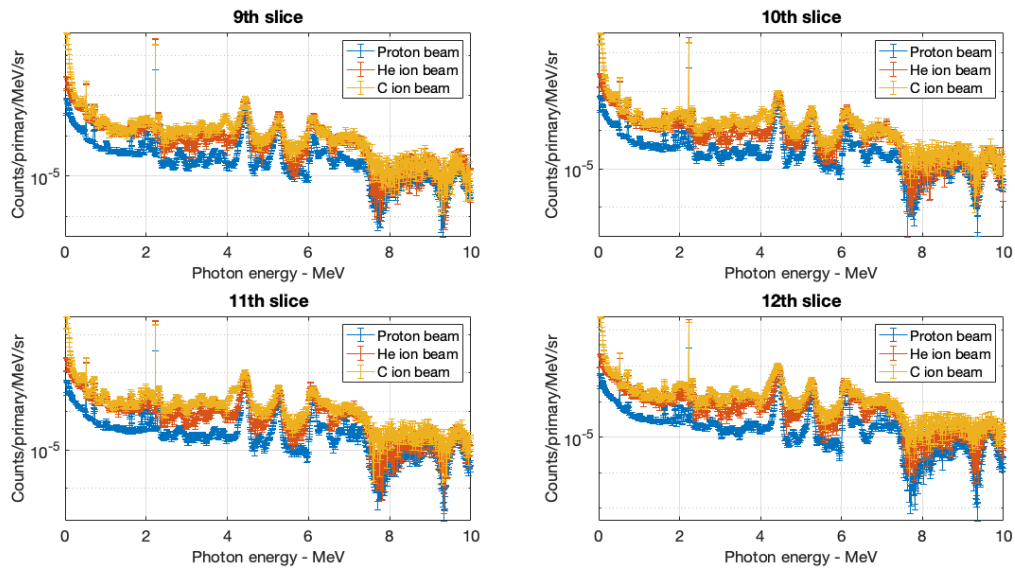


Figure 3.5: Double differential photon spectra in energy and solid angle, plotted against the energy. The secondary emissions from the 9<sup>th</sup> slice to the 12<sup>th</sup> are reported for the three different beams.

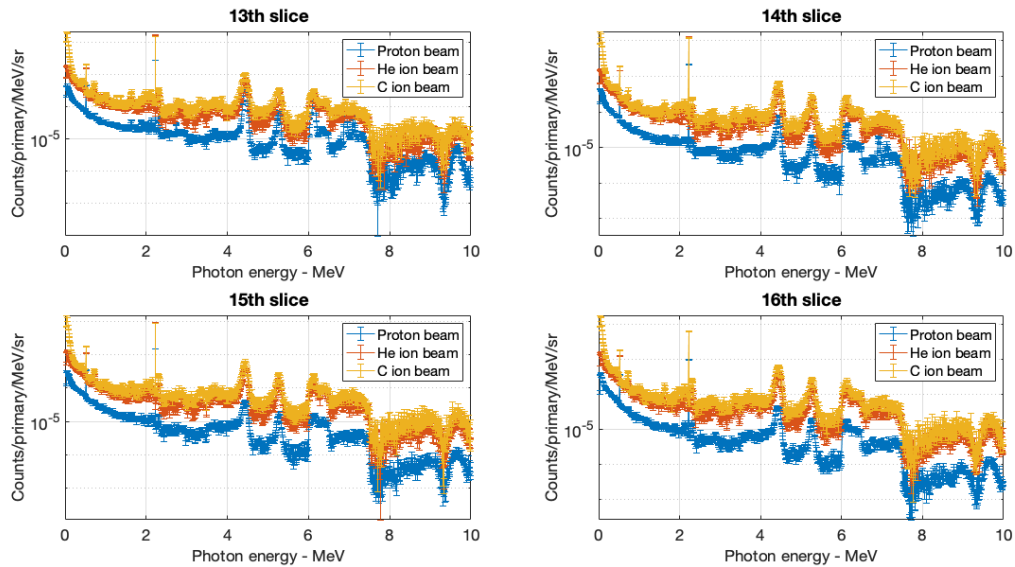


Figure 3.6: Double differential photon spectra in energy and solid angle, plotted against the energy. The secondary emissions from the 13<sup>th</sup> slice to the 16<sup>th</sup> are reported for the three different beams.

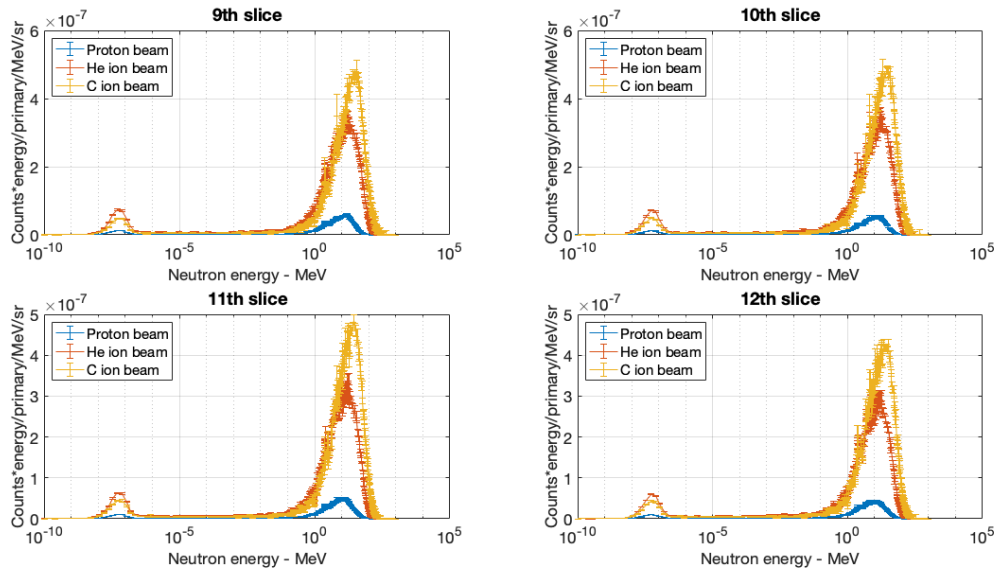


Figure 3.7: Lethargic double differential neutron spectra in energy and solid angle, plotted against the energy. The secondary emissions from the 9<sup>th</sup> slice to the 12<sup>th</sup> are reported for the three different beams.

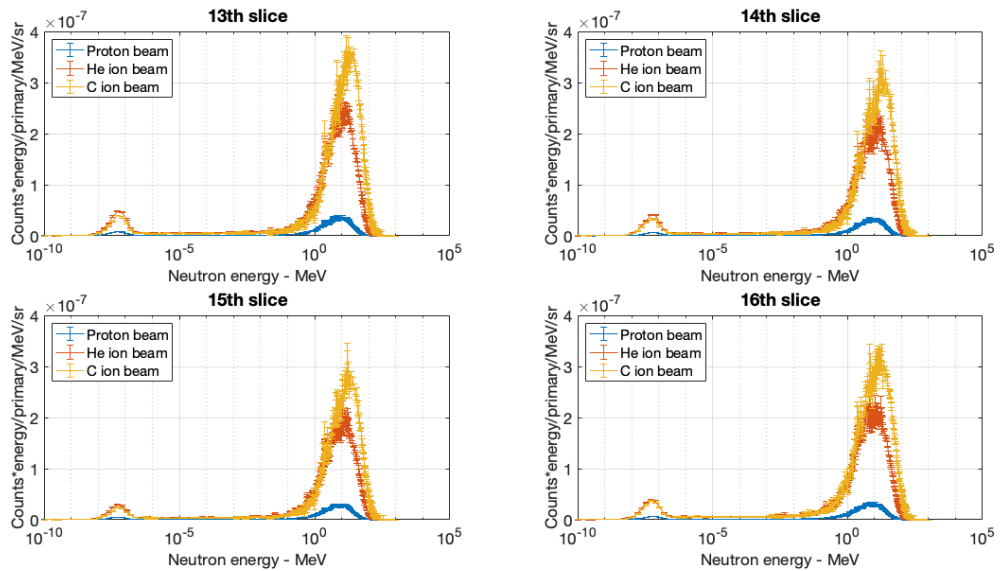


Figure 3.8: Lethargic double differential neutron spectra in energy and solid angle, plotted against the energy. The secondary emissions from the 13<sup>th</sup> slice to the 16<sup>th</sup> are reported for the three different beams.

### 3.3.1. Reasons

In recent years, there has been a substantial progress in the application of PGI mostly for what concern proton therapy. On the other hand, fewer studies were made in the range verification exploiting prompt gammas for carbon ion radiation therapy. Indeed, even if there are undoubted advantages of C-ion over proton and photon therapy [74], it is also true that the very same factors that make C-ions such interesting may hinder the application of PGI monitoring. For example, although C-ions have a higher yield of PG production with respect to protons [140], they also have a higher neutron production yield. In addition to this, the number of heavy ion projectiles needed to provide a given physical dose is smaller than for protons, due to the  $\frac{1}{Z^2}$  dependence of energy loss ( $Z$  being the atomic number) and the lower multiple scattering angle of heavier ion. The RBE leads to a further reduction of the number of ions necessary to deliver the desired biological dose with higher- $Z$  ions. Therefore, the total number of generated PGs for a given pencil beam spot is lower when considering heavier ions [133]: this strongly affects the counting statistics of PGs.

These factors make the optimization of detection efficiency and gamma-neutron discrimination even more critical for the application of PGI to CIRT. So far, the TOF discrimination technique has been successfully applied to the observation of PGs in carbon ion irradiation [118].

A feasibility study in the literature for the use of a pixelated slit camera in CIRT was performed by Smeets [111]. The results of the Monte Carlo simulations showed a weak correlation between PG and BP profiles. Anyway, the author himself questioned whether the MC code he used (MCNPX version 2.7.E) was mature enough for the simulation of prompt gamma emission during carbon ion irradiation at clinical energies.

The present thesis work took the precious legacy of the work conducted by Smeets and had the primary goal to investigate whether results come out differently with updated Physics models inside the general purpose FLUKA MC code. A numerical study was conducted to explore the feasibility of using a knife-edge slit prompt-gamma camera with a beam of C-ions at clinical energies. Firstly, I simulated the response of the detector to the delivery of a single pencil beam spot to a uniform soft-tissue phantom. The purpose was to test the sensitivity of the camera to shifts of the Bragg peak. In the second part of the study, I examined the cumulative signal obtained from the delivery of multiple spots within the same energy layer, seeking the chance to still reconstruct the position of the BP. The final goal of this work was to explore the PG fall-off retrieval capability with a well-established slit camera configuration, already tested clinically with proton irradiation.

### 3.3.2. Methods

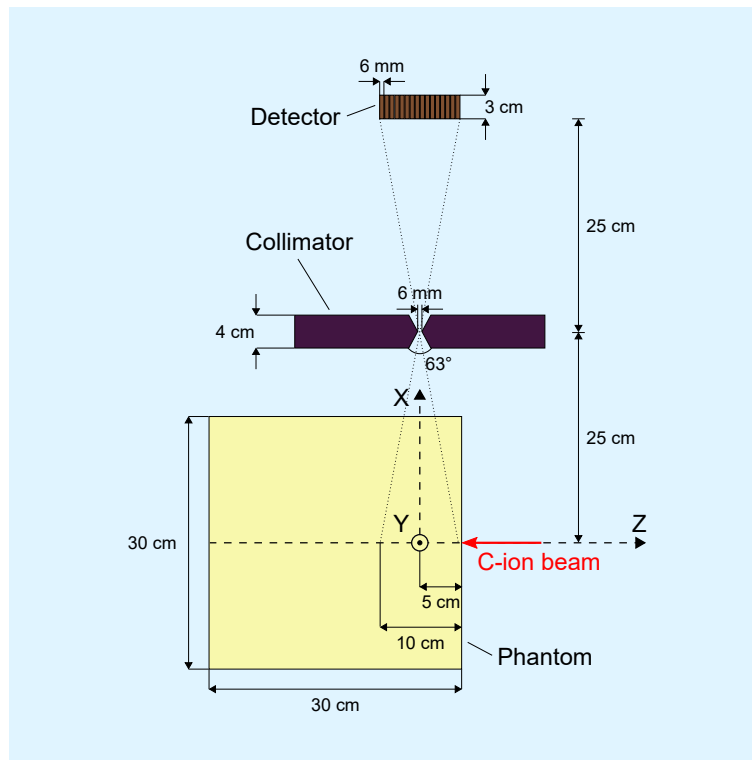
#### Outline of Monte Carlo simulations

Three sets of numerical simulations were performed using the FLUKA general purpose MC code for particle transport (version 4-1.1) [4]. Specifically, I scored the response of a pixelated knife-edge slit camera to the secondary particles emitted by a phantom irradiated with a C-ion beam.

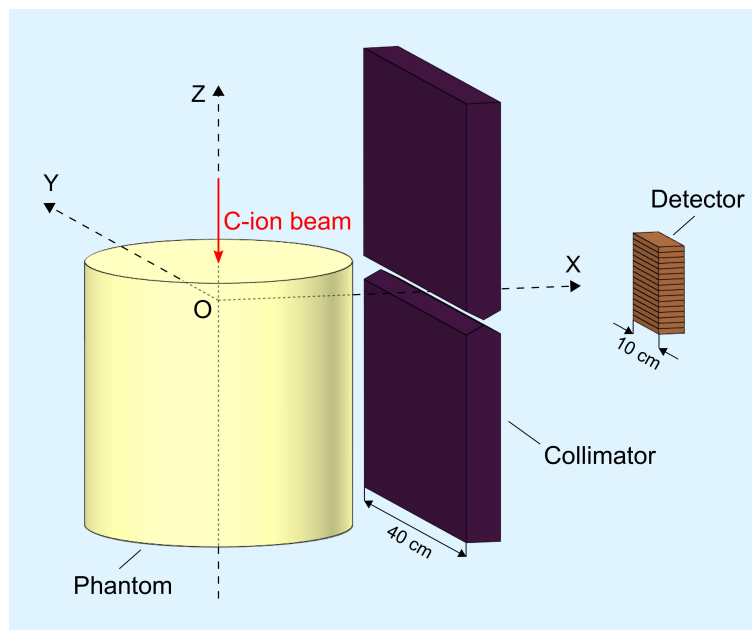
Although the irradiation geometry was slightly varied for the last simulation set, the generic setup is showed in Figure 3.9. A monoenergetic pencil beam of C-ions with a  $150 \frac{MeV}{u}$  energy was directed along the z-axis of the frame of reference towards one of the faces of the phantom, a square cylinder of 30cm diameter made of ICRP soft tissue. The energy of choice fits within the interval of therapeutic energies used in CIRT (at CNAO the beam energy range is  $120 \div 400 \frac{MeV}{u}$  [84] [104]). The irradiated face of the phantom was positioned at 5cm on the z-axis, so that the dose peak was almost centered on the origin of the reference frame (see Figure 3.9 (a)). I labelled this as the “no-shift” position. The detection system of reference for the simulations was a gamma camera similar to the one already developed and characterized in previous studies for proton therapy [94]. Such camera consists of a knife-edge collimator and a pixelated detector. The former is made of a tungsten alloy, 4cm-thick on the radial direction and 30cm wide along the beam axis. The knife-edge slit is 6mm-wide and has a  $63^\circ$  aperture angle. The detector is an array of 16 pixels made of  $Lu_{1.8}Y_{0.2}SiO_5$  (LYSO) scintillator, distributed along the beam axis with a pixel pitch of 6mm. Each pixel is a 10cm-wide slab with a 3cm thickness. As shown in Figure 3.9, the slit and the face of the detector were placed at a distance of 25cm and 50cm from the z-axis, respectively, giving a field-of-view of 10cm on the phantom. The detector and the slit were centered on the origin of the frame of reference to maximize the PG signal. The whole setup was defined inside a spherical room of 4m radius filled with air. See Table 3.1 for details about the materials.

I used the FLUKA “DETECT” estimator to score the spectrum of deposited energy in the detector on an event-by-event basis, considering each pixel as an independent detector. The spectrum was scored in 1024 energy bins, with a width of about 4 keV. Only the energy deposition events in the interval  $3 \div 7$  MeV were scored, as the most probable PG lines (reported in Section 3.2) are emitted within this energy window, as accounted by Kozlovsky *et al.* in Ref. [59]. Not only that, but a reduced scoring energy interval also brought to a lower simulation time.

For each pixel, the total number of events (or counts) in the scored energy interval was considered as the detector signal. Since DETECT does not discriminate the type of particle interacting with the detector, and since no particle was discarded in the simulation,



(a)



(b)

Figure 3.9: Schematic representation of the simulation geometry employed in this work: (a) 2D representation on the xz-plane; the depicted position of the phantom is labelled as the "no-shift" position; (b) 3D representation.

the signal was due to all secondary particles able to reach the detector, i.e., mainly photons and neutrons. Anyway, the FLUKA subroutine called "mgdraw.f" allows to save in a phase space file all features of a particle (type, energy, position, direction and so forth) crossing a certain geometry region. Exploiting "mgdraw.f", one MC simulation was dedicated to record in a text file all transport details about photons generated by carbon ion irradiation entering the detector region and the same was carried out for neutrons in a second file; in a second simulation, thanks to a second FLUKA subroutine "source\_newge.f", I separately transported photons and neutrons evaluating which were the two distinct contributions to the total detection profile, both from a qualitative and quantitative standpoint.

The transport of carbon ions takes much more time than simulations with protons as primary particles. This is a consequence of higher production of secondary particles for heavy ions, along with the possibility of the nucleus fragmentation, totally absent in proton simulations. Hence, simulating carbon ions implies a problem of speed: a typical simulation carried out in this thesis could also take more than 15 days to achieve an acceptable MC statistical error. For this, specific transport and production thresholds were introduced to cut off useless particle histories without affecting the physics of the problem. In particular, transport thresholds inside air and collimator were set at 3MeV for photons and electrons. Moreover, production thresholds of photons and electrons inside the target were set at 3MeV. Furthermore, fluorescence was turned off in the whole simulation volume, except inside the detector. In the latter, the electron and photon transport thresholds were set at 40keV. This energy is related to the K-shell of the element with the highest Z inside the detector, which results in a mean free path of the particle (electron or photon) considerably smaller than the pixel width of 6mm. Neutron generation by Fermi break-up of nuclei in the phantom was also introduced. For the scope of the study, the remaining characteristics of the detector (e.g., energy resolution) were considered ideal.

## Particle range sensitivity determination by target longitudinal shifts

For this first set of simulations, a 2D representation of the set-up is reproduced in Figure 3.9(b). The axis of the phantom and the beam lied along the z-axis.

The goal of the first set of simulations was twofold. First, I wanted to investigate whether the spatial correlation between the BP position and the PG profile along the beam axis could be identified even in the high neutron background of CIRT. Secondly, I explored the theoretical limits in the determination of PG fall-off in C-ion irradiation with the delivery of a single pencil beam spot to the phantom: indeed, I performed several simulations

Region	Material	Composition	Density (g/cm <sup>3</sup> )
Phantom	ICRP soft tissue	10.4%H - 23.2%C - 2.4%N - 63.0%O - 0.1%Na - 0.01%Mg - 0.13%P - 0.19%S - 0.13%Cr - 0.19%K - 0.02%Ca - 0.005%Fe - 0.003%Zn	1.00
Collimator	Tungsten alloy	90%W - 6%Ni	16.96
Detector	LYSO	Lu <sub>1.8</sub> Y <sub>0.2</sub> SiO <sub>5</sub>	7.40

Table 3.1: Composition and density of the materials assigned in FLUKA to the various regions of the simulation volume. Percentages in the compositions refer to atomic percentage.

using the same described configuration, but shifting the position of phantom along the z-axis, to effectively shift the position of the BP. This is a typical procedure that was used in experiments to characterize the sensitivity of a given PGI-system in determining the particle range [94]. From the "no-shift" position, the phantom was translated with a 2mm step both in the positive and negative direction of the z-axis, and the same simulation was repeated. For each shift of the phantom, we found that  $4 \times 10^9$  primary particle histories were enough to obtain a low Monte Carlo statistical error.

### Delivery of multiple irradiation spots at constant energy

In the second set of simulations, I evaluated the response of the gamma camera to the delivery of multiple irradiation spots within a single layer of the phantom, shifting the beam axis along the xy-plane, but keeping its energy constant. This emulated what happens in PBS systems of synchrotron-based treatment facilities, in which the spots of a given layer are delivered in a single "spill" of the accelerator (Section 1.3). I thus referred to this case as a "spill irradiation".

As shown in Figure 3.10, the nine selected spots had the same z-coordinate but were distributed on the xy-plane, covering a  $2 \times 2$  cm<sup>2</sup> area centered around the axis of the cylindrical phantom, which was placed at the "no-shift" position.

### Tilted target simulations to account for non-planar shape of patient surface

For the last set, the detector response to a spill irradiation was still examined. However, in a real treatment, the covered spots do not have all necessarily the same distal coordinate. Indeed, even though the beam energy is constant, the non-planar shape of the patient

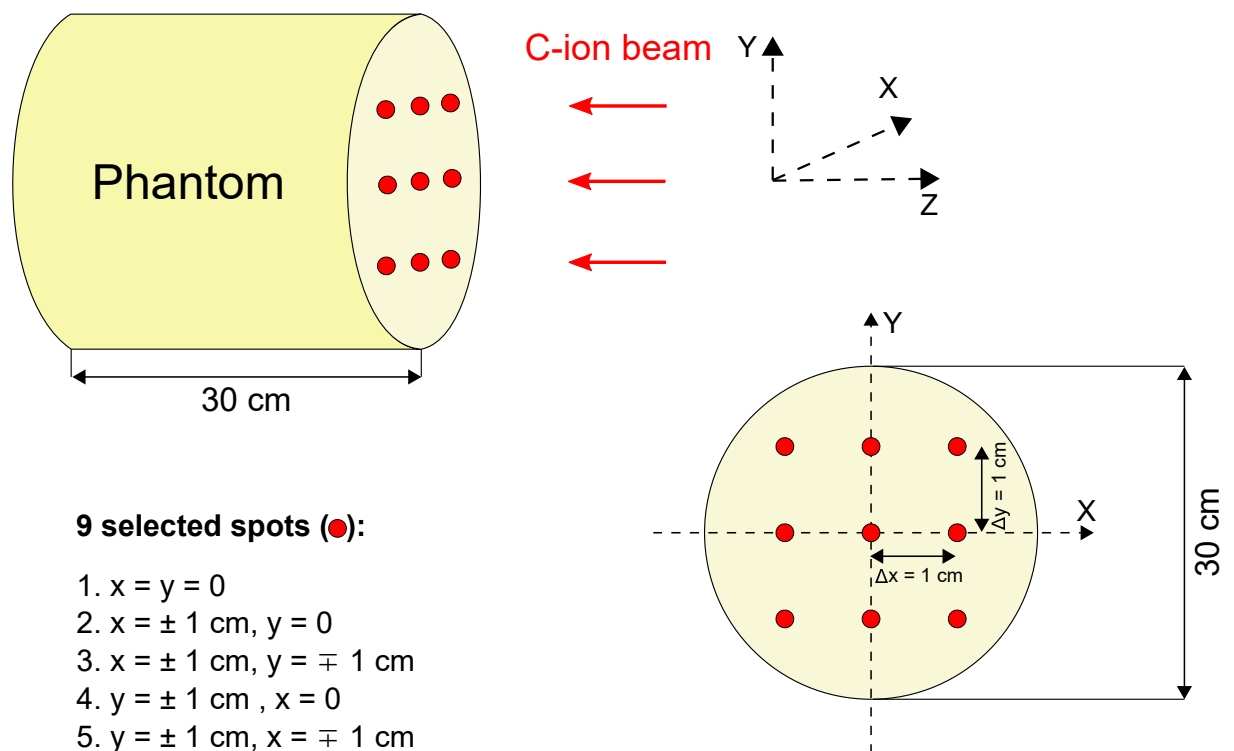


Figure 3.10: Illustration of the irradiation spots (red) selected for the second set of simulations. The spots have the same z-coordinate, and cover an  $2 \times 2 \text{ cm}^2$  area on the xy-plane inside the soft-tissue phantom (yellow). The pitch between the spots is 1cm.

surface and the inhomogeneities introduce a variation in the beam range for different spots. Instead of adopting an anthropomorphic phantom, the cylindrical phantom was inclined with respect to the z-axis by a  $22^\circ$  angle (Figure 3.11). In this way, the spots had a different z-coordinate, and the geometry of the set-up could be easily replicated in an experimental session. Moreover, the inclination angle of the phantom was chosen to be conservative, since moving the beam of 1cm along the xy-plane, the particle range varies of 4mm. Hence, good results for this kind of geometry would justify studies with a more realistic one. The detector geometry and the selected spots were still those described in the previous subsection.

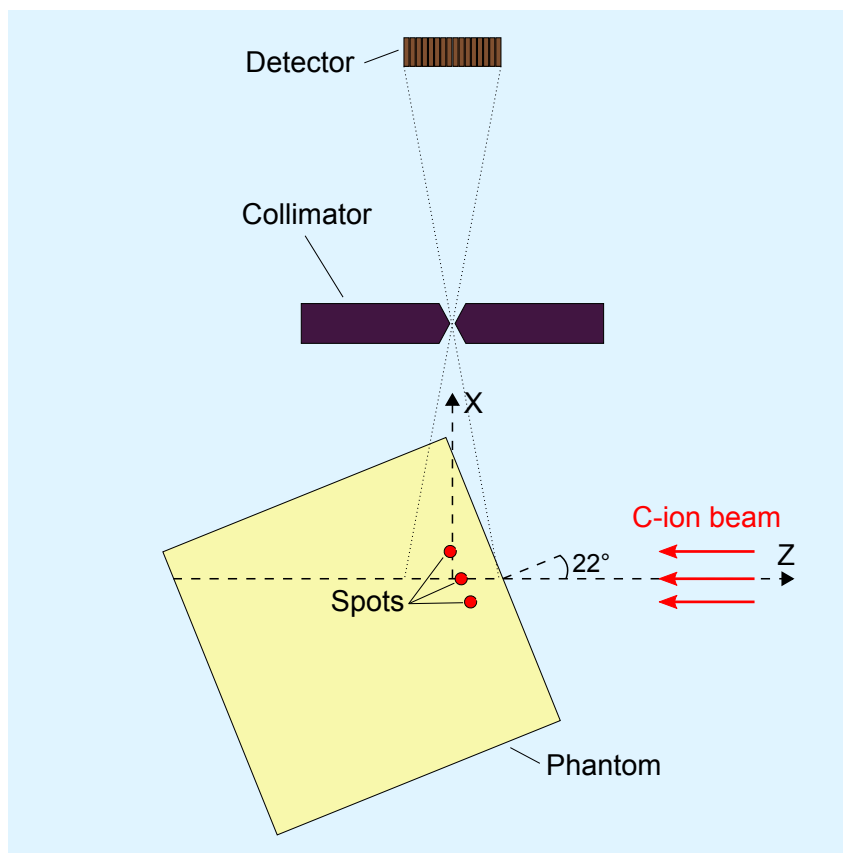


Figure 3.11: Simulation geometry of the third set of simulations: the target was inclined by a  $22^\circ$  angle with respect to the z-axis, so that the spots of Figure 3.10 have a different z-coordinate. This considers the variations of the beam range in a patient for the different selected spots, even with the beam at constant energy.

### Range retrieval precision analysis

On the simulation output data, an analysis was performed to determine the theoretical accuracy in the range retrieval of the PG camera, following an approach inspired by

Roellinghoff *et al.* [103]. The algorithm was composed by three autonomous parts.

In the first part, I obtained the signal curve from the FLUKA data. This curve represented the total number of counts (or events) per unit C-ion in each pixel as a function of the pixel position on the z-axis. I, then, chose a given number of incident C-ions,  $N_i$ , and, by this number, I re-normalized the counts in the signal curve, which was labelled as the “reference curve”. The reference curve represented the ideal signal curve numerically calculated, only affected by the MC simulation error (both statistical and systematic).

In the second part, I performed a MC propagation of the error on the reference curve. Namely, for each pixel I sampled a given number,  $N_c$ , of values from a Poisson distribution having a mean value equal to the number of counts of the reference curve. In this way, I obtained a given set of  $N_c$  noisy curves (Figure 3.12). Every noisy curve was interpolated with smoothing spline method, to get a continuous curve.  $10^4$  noisy curves were found to be enough to have a good statistics in the final normal distribution for all methods.

The final step of data analysis was to determine the precision of the detection system

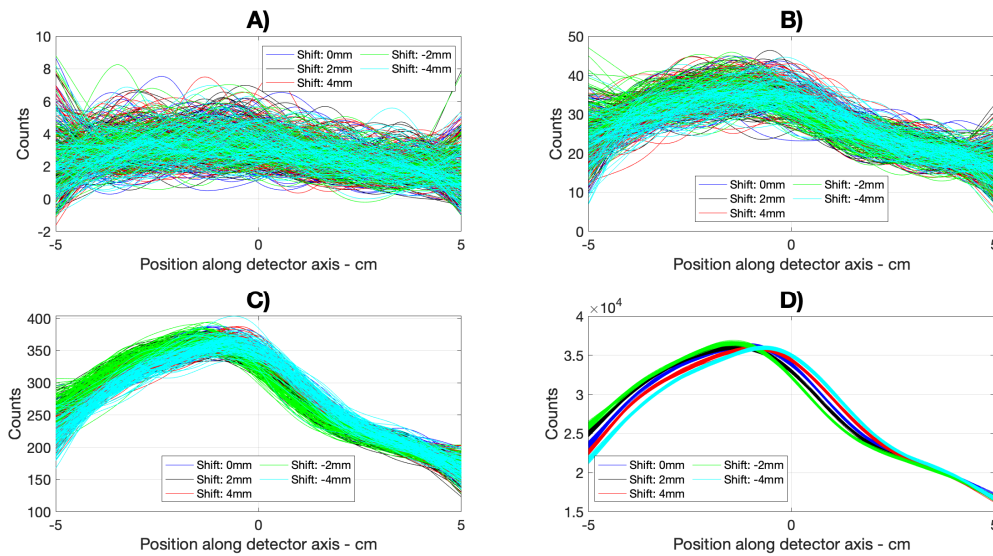


Figure 3.12: Graphical representation of the generated noisy curves for different phantom shifts and numbers of C-ions: **A)**  $10^6$ , **B)**  $10^7$ , **C)**  $10^8$ , **D)**  $10^{10}$ .

in retrieving the position of the dose fall-off, or its shift from the nominal position. To do this, I compared the obtained noisy curves with the reference one by employing three different methods to quantify the closeness of the curves. The graphical explanation of Method 1, which is similar to the one used by Roellinghoff *et al.* [103], is shown in Figure 3.13. For each noisy curve, the associated reference curve is shifted from its original position with a step of 0.02cm for a total path of 1cm, both in the positive and negative direction of the z-axis. To retrieve the shift for which the reference and the selected noisy

curves were superposed the most, a root mean square error (RMSE) is defined as figure of merit to quantify the degree of superposition. The optimal shift of the reference curve, the one that resembles the most the noisy curve under analysis, is found by the algorithm by minimizing the following RMSE (Eq. 3.1):

$$RMSE_{jk} = \sqrt{\frac{\sum_{i=0}^{N_p} (\text{predicted}_{ij} - \text{actual}_{ik})^2}{N_p}} \quad (3.1)$$

where  $\text{predicted}_{ij}$  represents the generic point  $i$  of the reference curve with shift  $j$  and  $\text{actual}_{ik}$  is the point  $i$  of the generic noisy curve  $k$ .  $N_p$  is the number of points which constitute the reference curve and each noisy one.

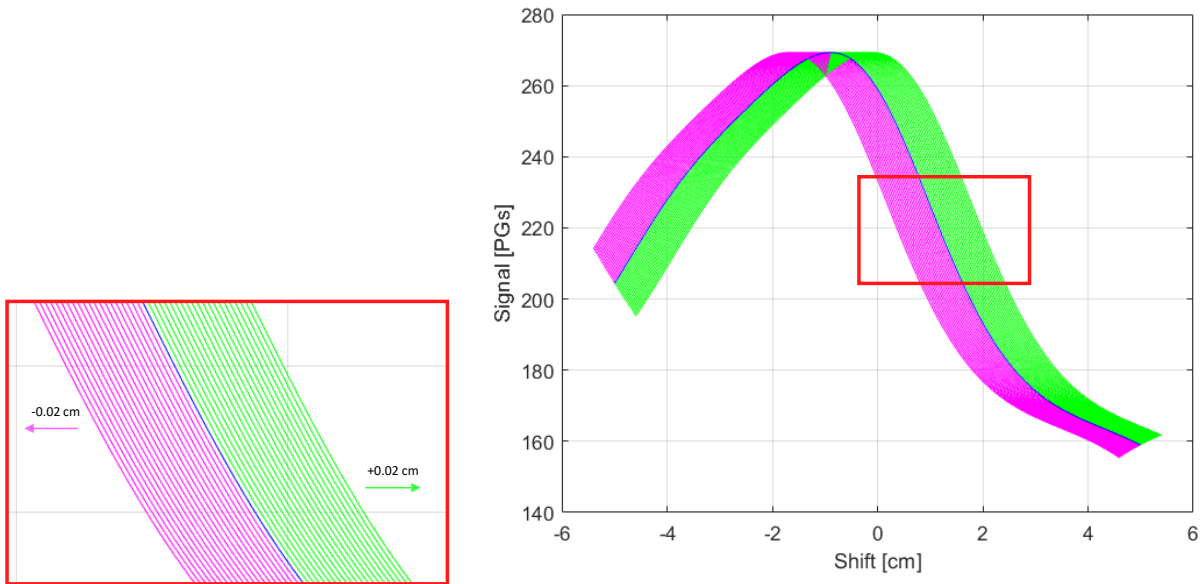


Figure 3.13: Graphical explanation of Method 1: the signal curve (blue) obtained by MC simulations is shifted up to 1cm, in 0.02cm steps, on the forward (green) and backward (purple) direction of the z-axis. The shifted curves are then compared with the investigated noisy curve, and the best match is found by a minimization of the RMSE.

The explained process is repeated for all generated noisy curves, obtaining a histogram of the optimal shifts, which could be approximated to a normal distribution, according to the central limit theorem. The precision in retrieving the BP fall-off is defined as twice the standard deviation of the resulting normal frequency distribution.

For Method 2, please refer to Figure 3.14. According to this method, each noisy curve (yellow) undergoes a linear interpolation (purple) in the fall-off region. Then, the algorithm is able to find the abscissa (green) of the intersection between the linear interpolation and the ordinate (blue) of the inflection point of the interpolated reference curve (red). The

distance between the green and black line (x-coordinate of the inflection point) is chosen as the error in the resemblance between the specific noisy curve and the reference one.

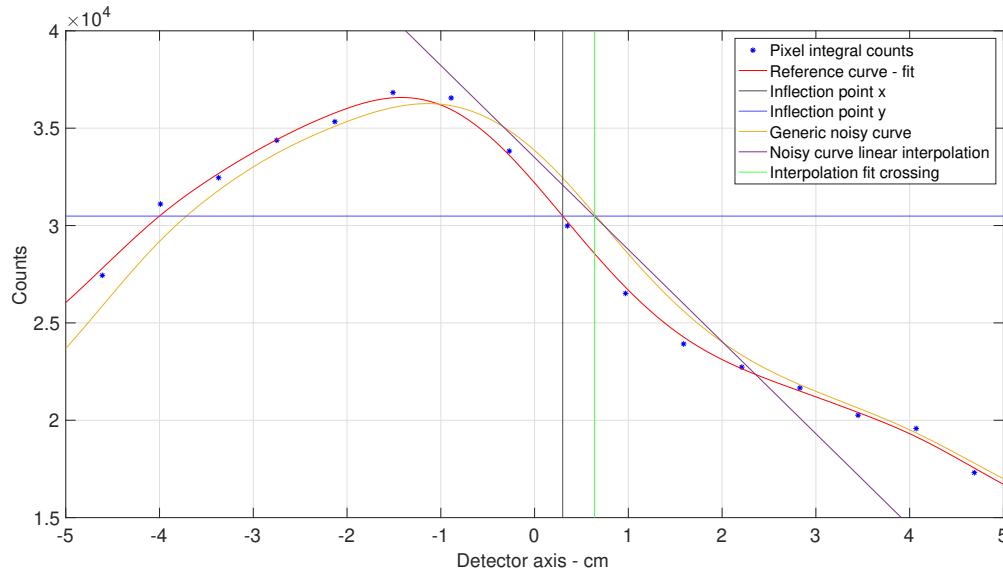


Figure 3.14: Graphical explanation of the Method 2: a generic noisy curve (yellow) is interpolated in the expected fall-off region (purple line), which is then crossed by the y-coordinate of the reference curve inflection point (blue line). The difference between the x-coordinates of the crossing point (green line) and of the inflection point is chosen as the error in the fall-off estimation.

Repeating this procedure for each noisy curve, the code produces a frequency distribution of positions in which the interception has occurred. As before, twice the standard deviation of the resulting distribution gives the theoretical uncertainty on finding the particle range.

Method 3 is explained graphically in Figure 3.15. The idea behind the code is to find the interception between the noisy curve (yellow) and the ordinate of the inflection point (blue) of the reference curve (red). The difference between the abscissas of the inflection point (black) and of the intersection point (pink) is chosen as the reconstruction error. Repeating this procedure for all the noisy curves, a normal distribution is again obtained.

Finally, I performed the analysis of the first simulation set results using as number of incident C-ions,  $N_i$ ,  $10^6$ ,  $10^7$ ,  $10^8$  and  $10^{10}$ . Referring to typical values used in therapeutic irradiation [13], the first  $N_i$  is close to the number of C-ions used in an irradiation spot and little lower than the minimum number of C-ions typically used in an irradiation spill (about  $4 \times 10^6$ ), while the second and the third are, respectively, in the middle of the interval and of the order of the maximum number of C-ions used in a spill. The last

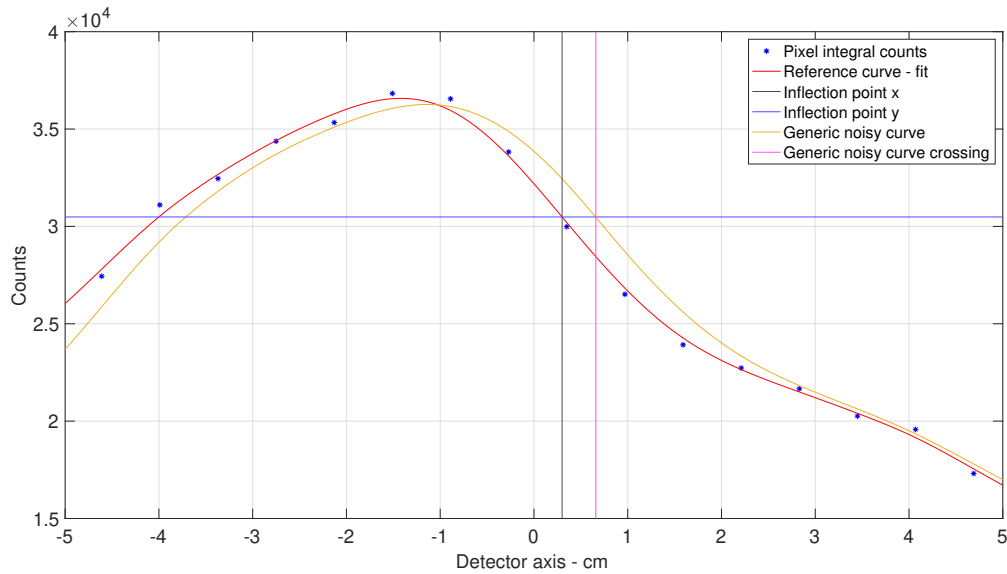


Figure 3.15: Graphical explanation of Method 3: the algorithm finds the x-coordinate (pink) corresponding to the interception between a generic noisy curve (yellow) and the y-coordinate (blue) of the inflection point of the reference curve (red). The error in the fall-off estimation was defined as the distance between the x-coordinates of the interception and of the reference curve inflection point.

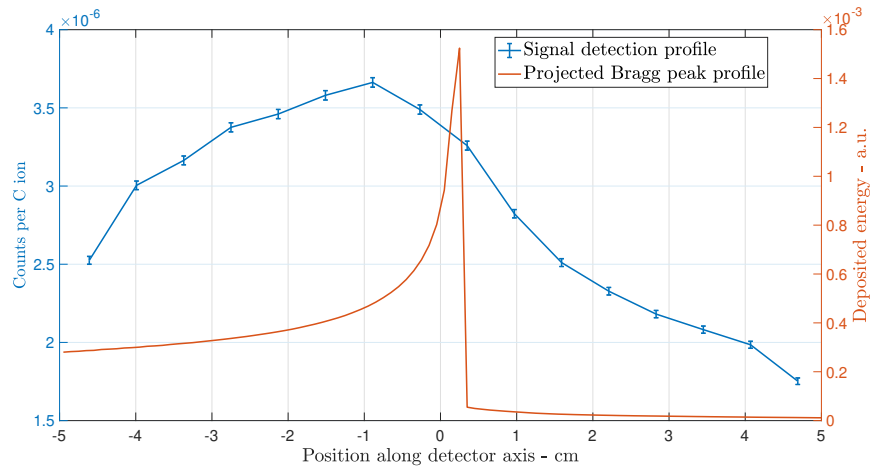
number is not found in a usual treatment, but it is considered as an upper bound inside the evaluation, which may be of interest for future developments in FLASH therapy [128]. For the second and third set of simulations (respectively, subsections 3.3.2 and 3.3.2), I performed the analysis using the average number of C-ions delivered in a spill, i.e.,  $5 \times 10^7$ .

### 3.3.3. Results

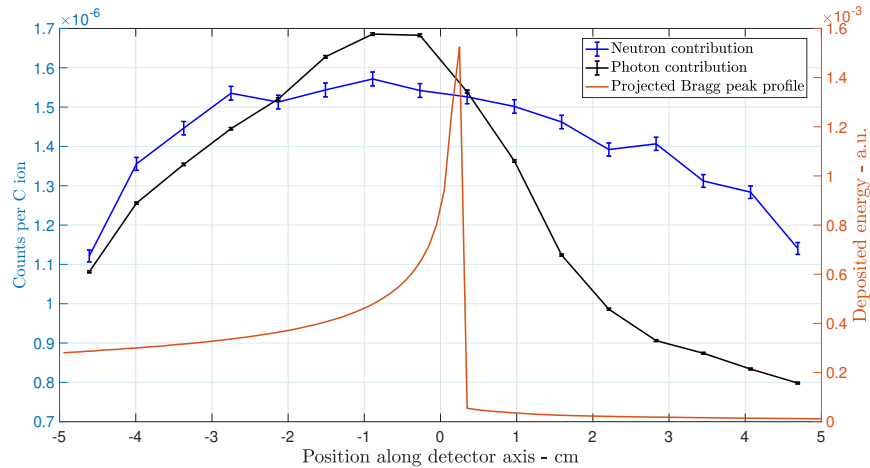
#### Particle range sensitivity determination by target longitudinal shifts

Figure 3.16(a) shows the profile of the total counts per unit of incident C-ion for each pixel, with the phantom in the “no-shift” position (see subsection 3.3.2). As for all the signal curves presented in the Results section, the error bars refer to the MC statistical uncertainty given by FLUKA. The signal curve (blue) is also compared with the inverted BP profile (orange), still obtained with FLUKA for the same simulation geometry and beam energy. The signal has a global maximum followed by a fall-off, that is clearly correlated to the BP. It is worth noticing that no discrimination was applied on the detector, so the signal is mainly due to the superposition of the PGs and the neutron background. Indeed,

Figure 3.16(b) separately shows the photon and the neutron contribution to the total detection signal, thanks to the "mgdraw.f" subroutine coupled to "source\_newgen.f". There exists a correlation between dose distribution and photon profile, while neutron energy deposition does not follow the step decrease of dose distribution. Without considering the possible losses due to the coupling between scintillator and readout in a real detector, the expected detection efficiency of the camera is of the order of  $3 \times 10^{-6}$  (Figure 3.16a).



(a)



(b)

Figure 3.16: Graphical representation of the correlation between the PG detection profile and the Bragg peak profile (orange), obtained with FLUKA simulations for the phantom in the "no-shift" position: (a) Total detection profile (blue); (b) Photon contribution to the detection profile (black) and neutron contribution to the detection profile (blue).

The signal profiles for the "no-shift" position and the symmetric translations of the phantom by 2mm and 4mm along the z-axis are displayed in Figure 3.17. The curves are clearly distinguishable, and both their maximum and fall-off move together with the BP. Con-

### 3| Monte Carlo feasibility study of a prompt gamma slit camera in carbon ion therapy

90

sidering that these are ideal curves, as they do not include the error due to the counting statistics and other non-idealities, a 2mm shift in the range is theoretically distinguishable.

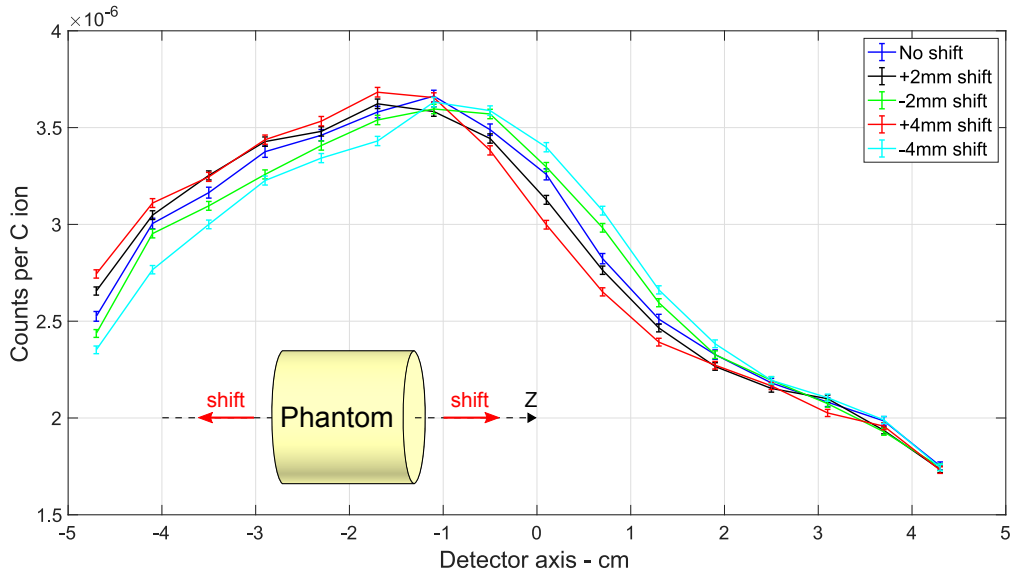


Figure 3.17: Range shift sensitivity: ideal signal curves obtained by MC simulations for various shifts of the phantom along the z-axis.

Results of the data analysis algorithm applied to ideal curves are presented in the following figures and are summarized in Table 3.2.

The application of Method 1 to these noisy curves produced the distributions illustrated in Figure 3.18, while Figure 3.19 refers to Method 2. Results of the Method 3 are not shown, as they were qualitatively identical to those of Method 2 (see subsection 3.3.2 for a description of the methods). An advantage of the latter two methods is the opportunity to see how the frequency distributions associated to the sets of noisy curves are located along the detector axis.

As expected, the precision in retrieving the fall-off of dose distribution is strictly connected to the number of incident C-ions. As reported in Table 3.2, the three methods gave similar results, Method 1 being the most optimistic. Figure 3.20 shows the plot of the precision retrieved by Method 1 versus the number of C-ions on a double logarithmic scale, considering the averaged precision over the shifts. The linear interpolation of the data produced a slope of about  $-1/2$ , thus the theoretical accuracy was found to be inversely proportional to  $\sqrt{N_i}$ . Considering the average results given by the three methods (see Table 3.3), a number of ions of about  $3 \times 10^8$  would be necessary to achieve a theoretical accuracy of 2mm in a single spot irradiation. Finally, all Gaussian curves are perfectly distinguishable at  $10^{10}$ , showing that with a very high number of particles even a sub-

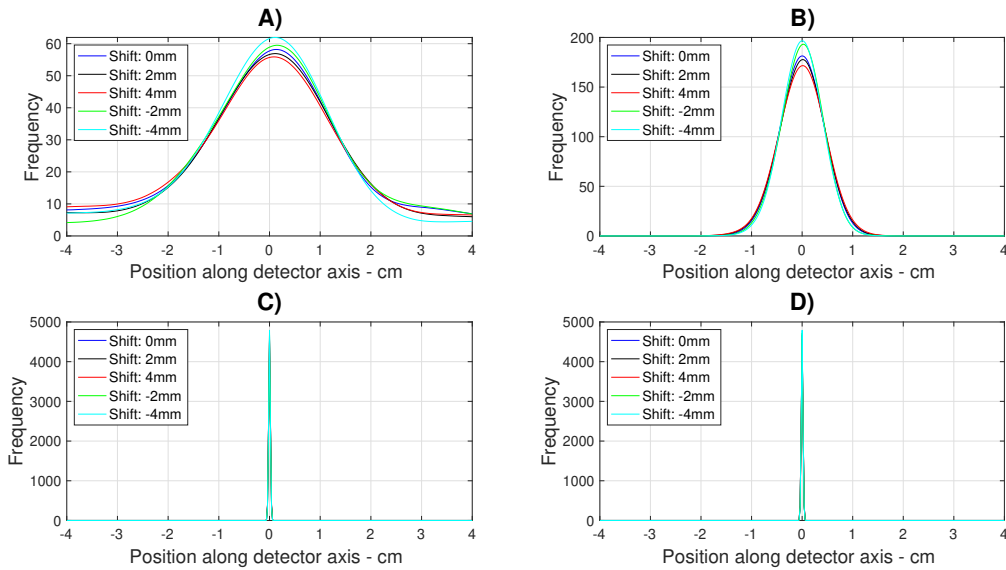


Figure 3.18: Results of Method 1. The frequency distributions pertaining to the various shift of the phantom are presented for different numbers of C-ions: **A)**  $10^6$ ; **B)**  $10^7$ ; **C)**  $10^8$ ; **D)**  $10^{10}$ .

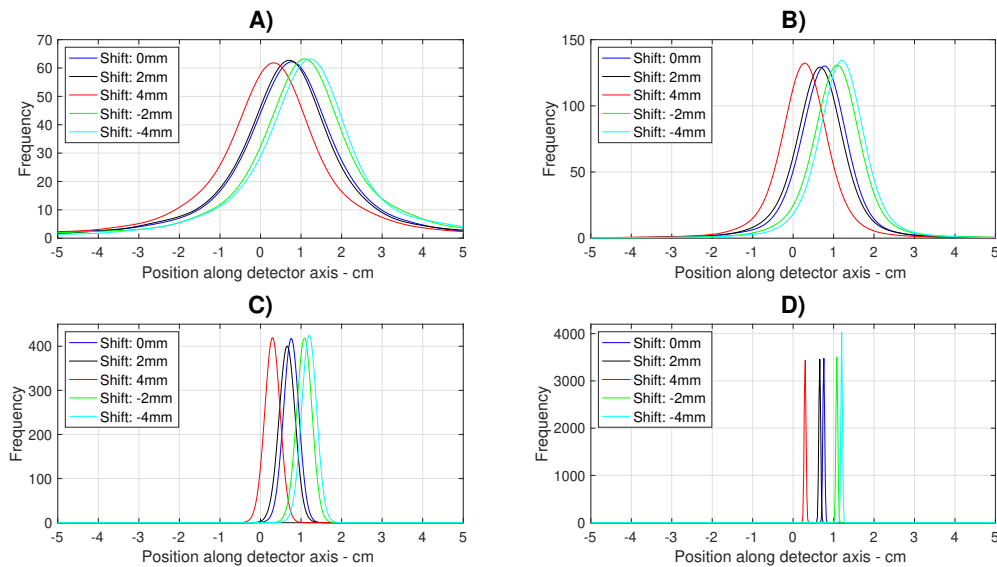


Figure 3.19: Results of Method 2. The frequency distributions pertaining to the various shift of the phantom are presented for different numbers of C-ions: **A)**  $10^6$ ; **B)**  $10^7$ ; **C)**  $10^8$ ; **D)**  $10^{10}$ . Unlike for Method 1, the centroids of the Gaussian curves shift together with the phantom position.

Table 3.2:  $2\sigma$  of the Gaussian frequency distributions resulting from the data analysis of the first set of simulations. Results are reported in mm, for the various numbers of C-ions: **A)**  $10^6$ ; **B)**  $10^7$ ; **C)**  $10^8$ ; **D)**  $10^{10}$ .

<b>A)</b>					
	No shift	2mm shift	-2mm shift	4mm shift	-4mm shift
Method 1	30,571	29,515	28,666	30,865	27,858
Method 2	27,084	27,165	26,754	27,963	26,996
Method 3	26,691	27,147	27,355	26,529	27,897
<b>B)</b>					
	No shift	2 mm shift	-2mm shift	4mm shift	-4mm shift
Method 1	7,724	8,002	7,480	8,385	7,243
Method 2	13,571	13,295	13,347	13,070	13,614
Method 3	12,235	12,228	12,256	11,471	12,411
<b>C)</b>					
	No shift	2 mm shift	-2mm shift	4mm shift	-4mm shift
Method 1	2,320	2,491	2,311	2,518	2,238
Method 2	3,380	3,508	3,337	3,274	3,293
Method 3	3,484	3,668	3,509	3,470	3,415
<b>D)</b>					
	No shift	2mm shift	-2mm shift	4mm shift	-4mm shift
Method 1	0,261	0,271	0,258	0,273	0,252
Method 2	0,354	0,359	0,358	0,368	0,369
Method 3	0,361	0,373	0,367	0,364	0,352

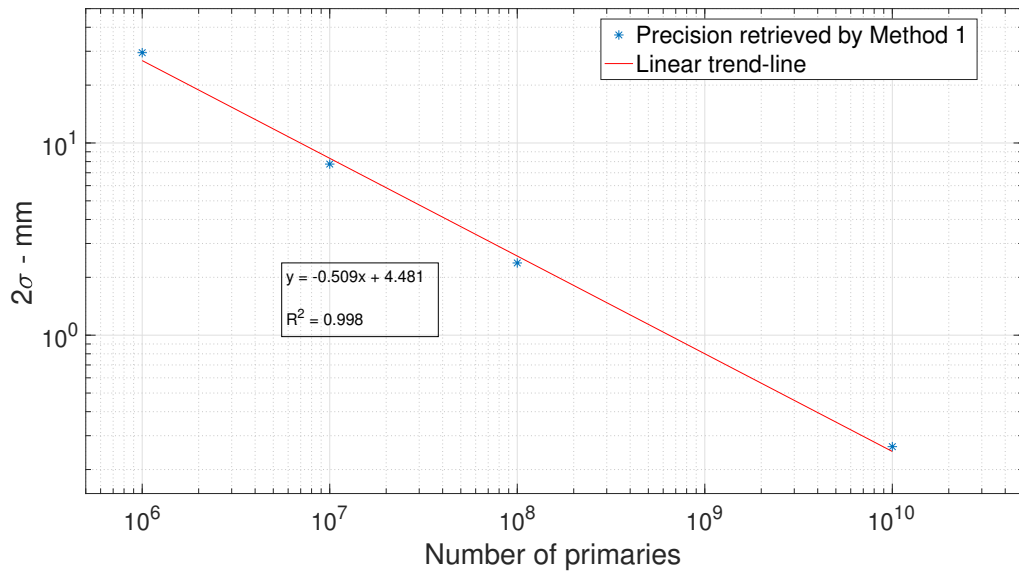


Figure 3.20: Range retrieval precision (blue) obtained by Method 1 plotted against the number of incident C-ions on a log-log scale. The precision is averaged over the shifts of the phantom. The linear interpolation (red) has a slope of about  $-1/2$ .

millimeter precision is achievable.

Table 3.3: Linear trend-line fitting parameters of the retrieved precision for all the three methods and different amount of C-ions.

	Slope	Y-intercept	$R^2$
Method 1	-0,509	4,481	0,998
Method 2	-0,482	4,397	0,992
Method 3	-0,477	4,353	0,996
Global	-0,498	4,495	0,996

### Delivery of multiple irradiation spots at constant energy

Figure 3.21 illustrates the results of the second set of simulations. The profiles of the signal per unit of incident C-ion are represented for the nine selected spots. The curves appear grouped in subsets of curves pertaining to a specific shift of the beam along the x-axis. Indeed, since the detector was only pixelated on the z-axis, the signal was almost independent on the shift of the beam along the y-axis. In contrast, moving the

beam along the x-axis, the distance between the beam and detector was varied, thus changing the geometric efficiency without affecting too much the shape of the curve. This is further demonstrated in Figure 3.22, in which the curves were compared after a peak normalization, showing that the normalized profiles are very similar for all the curves.

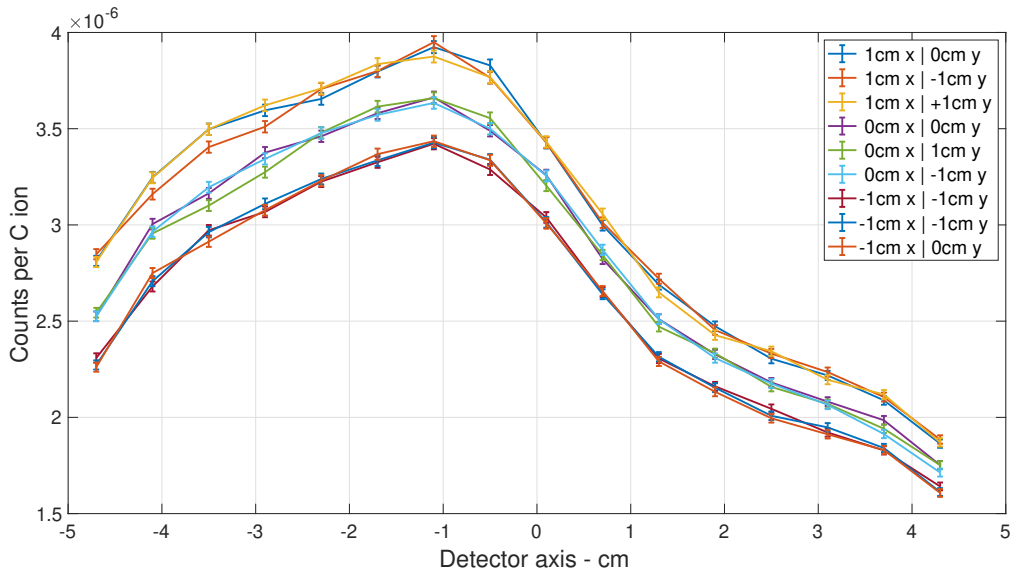


Figure 3.21: Graphical results of simulations for the nine selected spots (see Figure 3.10). The signal is varied only by a shift in the x-direction.

As stated in Section 3.3.2, an aspect of interest was the signal coming from the delivery of an accelerator spill, to study the feasibility of applying PGI on a layer-by-layer basis. Thus, I summed the curves corresponding to the nine spots, obtaining a reference signal curve for the whole spill. I, then, performed the analysis described in subsection 3.3.2 on the reference curve with a total incident number of ions equal to  $5 \times 10^7$ , assuming that these ions were delivered homogeneously in the nine selected spots. The results of the analysis are shown in Figure 3.23. The accuracy was given again by twice the standard deviation of the frequency distribution. In this case, I could state that the accuracy was referred to the capability of retrieving the range of a given energy layer covered by the beam, in the simplifying hypothesis of a perfectly planar transverse layer. The estimated theoretical accuracy given by the average of the three methods resulted of  $4.2 \pm 0.6\text{mm}$ .

### Tilted target simulations to account for non-planar shape of patient surface

In this subsection, I present the results of the simulations of C-ion irradiation on the tilted phantom. The detected profiles are plotted in Figure 3.24. As for the previous set,

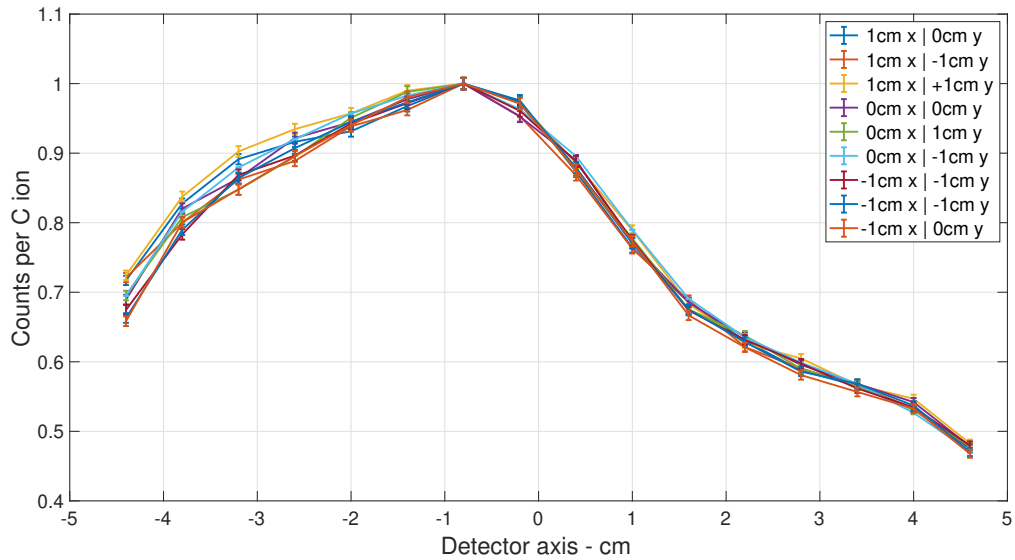


Figure 3.22: Peak normalization of detection profiles presented in Figure 3.21.

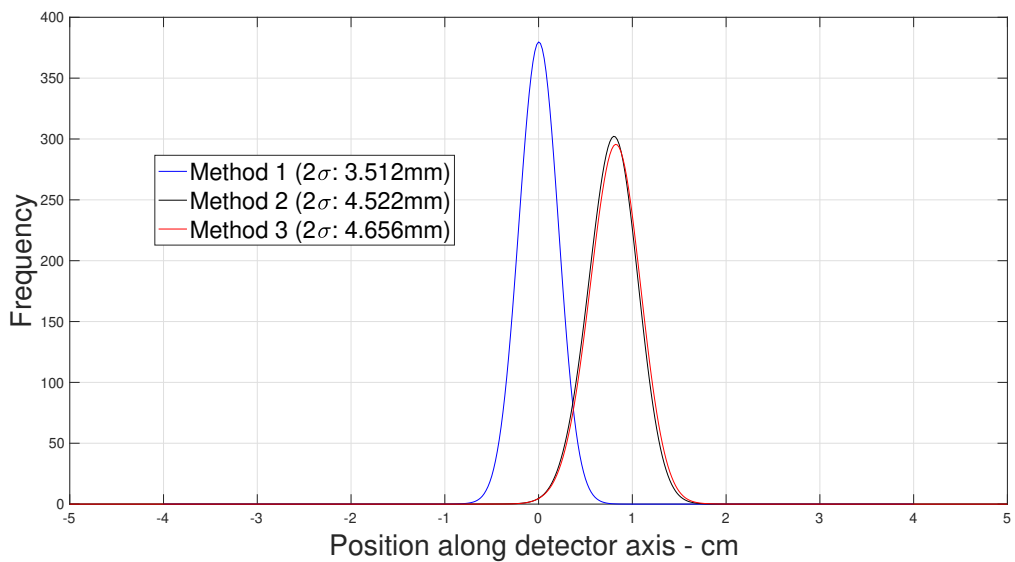


Figure 3.23: Results from range retrieval precision analysis. The Gaussian distributions are found applying the aforementioned methods, whose precision is resumed in the legend.

### 3| Monte Carlo feasibility study of a prompt gamma slit camera in carbon

96

ion therapy

I calculated the integral signal of all the considered spots, for a total number of  $5 \times 10^7$  incident ions. I, then, performed the analysis, whose results are shown in Figure 3.25. The frequency distributions of Method 2 and 3 are shifted with respect to the previous case, because of the target tilt. However, the theoretical accuracy was not worsened in the case of a tilted layer, as the average precision derived from the three methods was  $4.4 \pm 0.5\text{mm}$ .

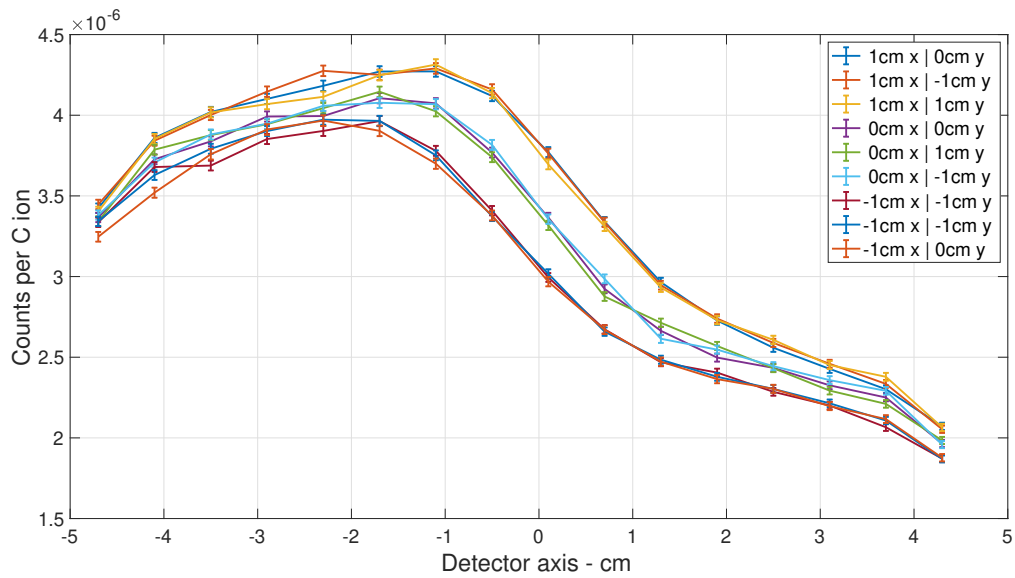


Figure 3.24: Signal curves obtained with FLUKA for the nine selected spots, in the case of the tilted target.

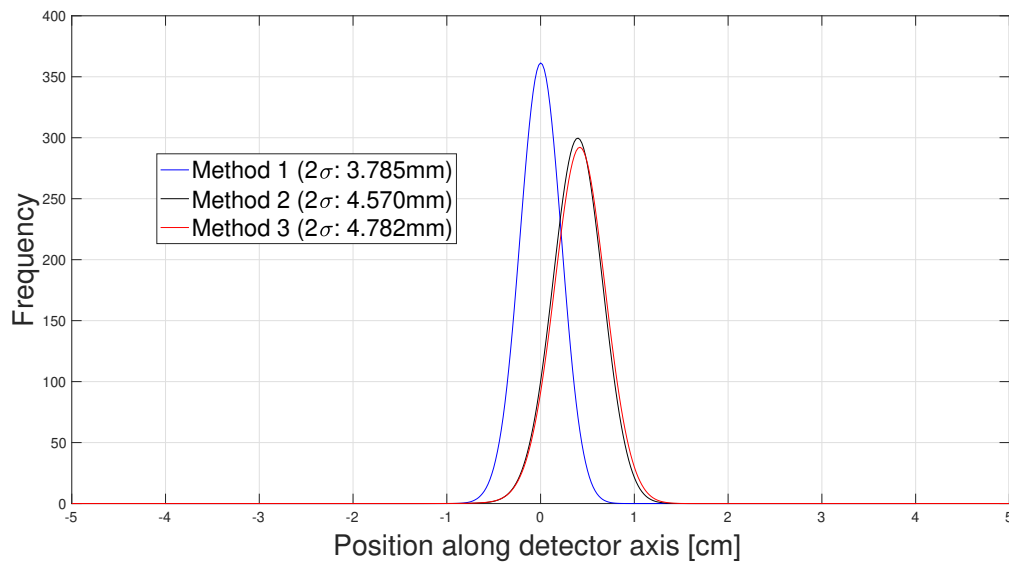


Figure 3.25: Results from range retrieval precision analysis in the case of the tilted phantom. The Gaussian distributions are found applying the aforementioned methods, whose precision is resumed in the legend.



# 4 | Proposal of an experimental set-up for future measurements

*The main purpose of this thesis was to investigate the possibility to apply the PGI-technique in carbon ion irradiation. In Chapter Three, it was demonstrated that, at least on a simulation level in case of a spill irradiation, it was feasible to consider prompt gammas as a useful tool to retrieve the Bragg peak fall-off, reducing range uncertainties. The subsequent step is the experimental validation of what was obtained in numerical simulations: indeed, Chapter Four will propose of an experimental set-up to prove the results obtained in the previous Chapter.*

*In the first section, focusing on the electronics readout, I will show a general architecture of the detection system that will take part in future measurements: starting from the features of LYSO crystals, I will end up with the description of the data acquisition system. Finally, in the second section, I will report the design choices of the front-end printed circuit board (PCB), an important part of the readout chain, whose purpose is to transmit the signal from the application-specific integrated circuits (ASICs) to the data acquisition system. The components of this board will be described in detail and all the design choices will be justified.*

## 4.1. The experimental set-up

Future measurements will consider as much as possible the simulation geometry of FLUKA input file: a cylindrical phantom of tissue equivalent material will be irradiated, inside an air-filled room, while a knife-edge collimator will be positioned before the detection system.

What really misses to pursue this task is a novel detection system, under development at Politecnico di Milano, which will allow the measurement of high energy gamma-rays, produced downstream C-ion irradiation. The therapy center that will provide the C-ion beam will be the CNAO, in Pavia [104].

### 4.1.1. The architecture of the detection system

#### Detection stage

Due to the good properties described in Section 1.5, the scintillation crystal material chosen for MC simulations was cerium cerium-doped lutetium orthosilicate  $\text{Lu}_{1.8}\text{Y}_{0.2}\text{SiO}_5:\text{Ce}$  (LYSO:Ce), which will also be employed in measurements. As depicted in Figure 4.1, each LYSO crystal will be composed by a matrix of 16 pixels with side of 6.25mm, for the total dimension of  $(1 \times 1)\text{in}^2$ .

In the set-up, two of such crystals will be put one next to the other in the amount of 32 pixels. Each LYSO crystal will be read by a  $4 \times 4$  tile of SiPM, which are supposed to collect the gamma signal that was first converted into visible photons inside the scintillator. The selected SiPM tiles will adopt a SPAD cell size of  $(15 \times 15)\mu\text{m}^2$ , a choice dictated by two parameters characterizing the final performances of the readout chain: linearity and speed. With such a high density of cells, the response of the system will be fast enough, and saturation will not constitute a problem.

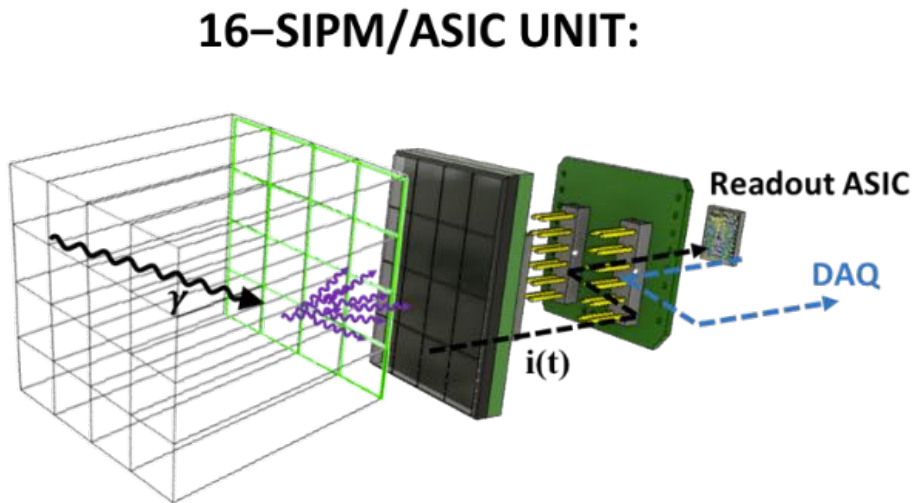


Figure 4.1: Schematic drawing of a single detection module of  $4 \times 4$  SiPMs followed by a readout ASIC. A gamma-ray, interacting with a LYSO crystal, produces visible photons which are collected by the represented tile of SiPM. Beyond the readout ASIC, the signal reaches the data acquisition system which quantitatively takes track of photon interactions.

## Readout electronics

The gamma-ray energy is firstly split by means of the scintillation crystals into visible photons, which are then converted into electronic charges inside the SiPM tiles constituting the useful analog signal. By a one-on-one coupling between the 16 pixels of a SiPM tile and the 16 analog channels of an ASIC, signals are then managed by an FPGA (field-programmable gate array) after being digitized through ADCs (analog to digital converters) mounted on a front-end PCB. To cover the entire area of the gamma camera, one FPGA is necessary. At last, the collected data will be sent to a host PC through the USB 3.0 connection, as shown by a more complete representation of the readout electronics in Figure 4.2.

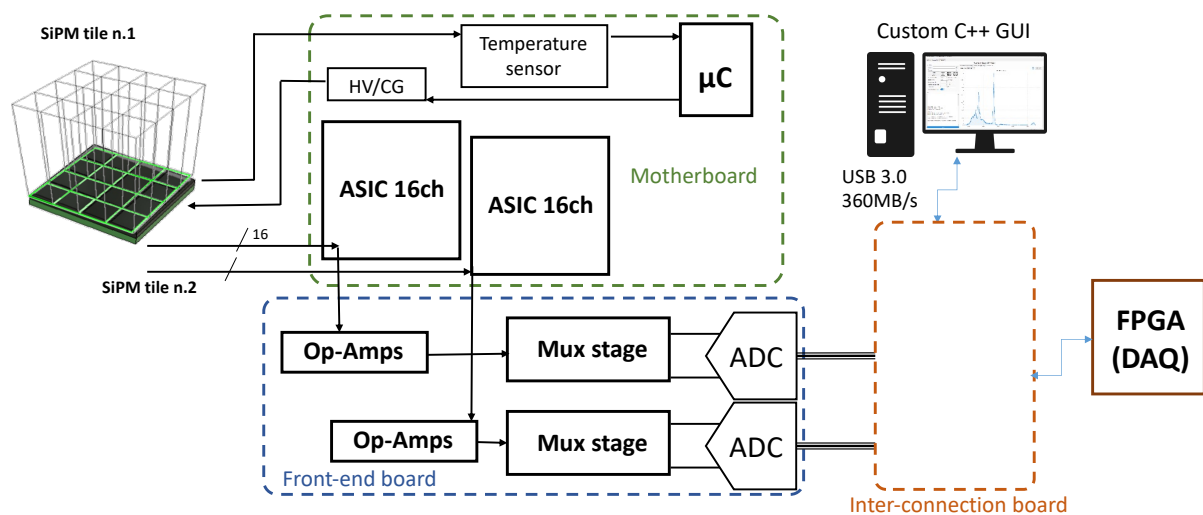


Figure 4.2: Architecture of the readout electronics, including the motherboard with two ASICs and a micro-controller for gain stabilization, a front-end PCB with a dedicated MUX stage and ADCs; the inter-connection board puts in contact the front-end board with the FPGA-based DAQ and a PC reached by a USB 3.0 connection.

Beyond the scintillator and SiPM layers, the chain will continue with the motherboard and the so-called front-end (FE) board, up to the DAQ stage. The two SiPM tiles will provide the signal to be processed to the motherboard, which will dispose of temperature sensors and a dedicated high voltage power supply controlled by a micro-controller for gain stabilization. Most importantly, the motherboard will contain two custom ASICs developed at Politecnico di Milano, called "SITH" (Spectroscopy Imaging Timing Hadrontherapy). SITH was designed to have 16 channels both for analog and trigger signals and will be used to manage a SiPM tile of 16 pixels: it will read the current supplied by the photodetector; moreover, it will output both a trigger signal for the arrival time information and an analog voltage signal representing the energy of the gamma-ray in a specific channel.

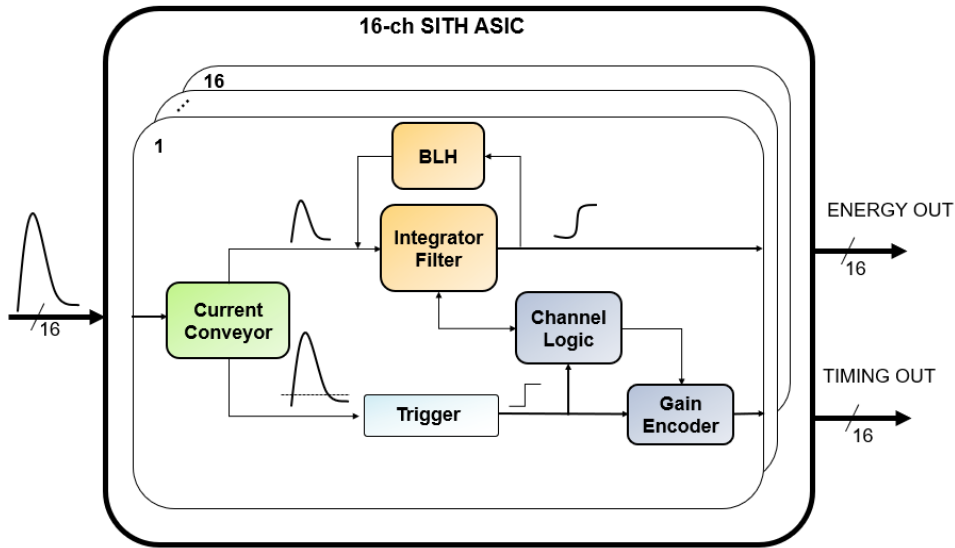


Figure 4.3: Schematic representation of the SITH ASIC. In each of the 16 channels, a current conveyor drives the current into two separated branches: the first is composed by a baseline holder (BLH) and an integration filter to produce the energy output; the other possesses a trigger and a gain encoder to output a timing signal.

Its block diagram is shown in Figure 4.3.

For the PGI-technique, only the analog signals will be utilized, but SITH does not preclude future studies where the timing information will be useful (for instance, for pulse shape discrimination using CLYC scintillator).

The motherboard will be directly linked to the FE board by means of suitable connectors, while the inter-connection, DAQ and USB boards will be remotely connected using selected cables. Once the signals are digitized by the ADCs (Figure 4.2), they will reach the inter-connection board which is needed to connect independent boards, i.e., the evaluation board of the FPGA, front-end board and the one hosting the USB 3.0 connection. Otherwise, it would not be feasible to connect all these boards together.

The front-end PCB has the purpose of digitizing the analog signals coming from the ASICs and to provide them to the FPGA. The latter is used as a control system for the front-end PCB: it gathers timing information directly from the trigger signals coming from the SITHs, and manages all the data stream to be sent to the inter-connection board before coming to a custom  $C^{++}$  GUI, by means of a USB 3.0 connection with a maximum speed of  $360 \frac{MB}{s}$ . Finally, on the host PC, the information about the gamma detection is associated to the pixel in which the photon was detected, so that the distribution of secondary emissions due to the primary C-ion beam irradiation will be imaged.

## 4.2. Design of the front end PCB

The front-end circuit will be developed to read the 32 analog channels (plus the 32 trigger lines) coming from the two SITH ASICs, and to convert them into digital data to be provided to the FPGA. The trigger lines will provide the information about the arrival time of gamma-rays impinging on the camera and will be directly routed from the ASICs to the FPGA. It is worth saying that their routing length should be matched to the maximum extent possible, to minimize the skew error between them. On the other hand, the 32 analog signals will be buffered, multiplexed with four parallel multiplexers, and converted into digital values through a differential ADC.

This board is designed starting from the assumption that the gamma camera will adopt a pixelated LYSO crystal, whose light yield is of  $3.32 \times 10^4 \frac{ph}{MeV}$  and the emitted light has a decay time of 36ns with a shape similar to an exponential decay [105]. Neglecting pile-up effects, the camera can detect a gamma-ray at most every 200ns, a time during which most of the generated charge will be integrated. Anyway, pile-up is a real problem and solutions can be adopted to reduce its impact. For instance, a small time window of detection could be used, so that the probability that two gamma-rays impinge on the same pixel will be low. The problem of this approach is that the integrated energy will be lower too: a tradeoff between integrated energy and pile-up probability is established, where the optimal condition will be given by the specific application.

Nonetheless, according to the physical properties of LYSO crystals, it is reasonable to size the detection system in such a way to sustain, for each channel,  $5 \times 10^6$  counts per second as maximum input rate. This number will drive the choices about the components of the FE board. For example, given a single multiplexer managing 8 channels, a minimum switching frequency of 40 MHz will be necessary to meet the desired input rate. Hence, a clock frequency of 50 MHz is chosen for both the ADC and the multiplexer, and it is not casual that the value is the same for the two components. Referring to the ADC, every data conversion starts at each clock cycle with a working frequency of 50 MHz, so that multiplexer is forced to the same switch frequency allowing the ADC to read the next value. The reading mechanism, along with the channel selection, is managed by the FPGA, selecting the multiplexer's input signal corresponding to the triggered channel.

In Figure 4.4, a schematic representation of the main blocks composing the present PCB are reported. The analog signals, first, are buffered into an Op-Amp stage; then, they move to a MUX stage before being converted into digital signals by the ADCs. In the following subsections, more details about the design of the cited single stages will be given.

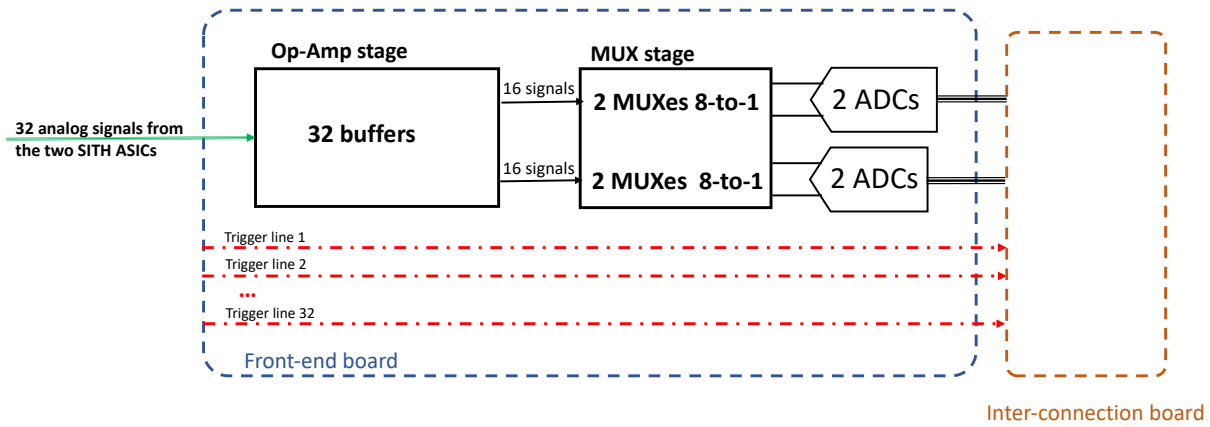


Figure 4.4: Schematic representation of the main blocks composing the FE PCB: an Op-Amp stage to buffer the analog signals, a MUX stage to select each of them which are then converted into digital signals by the ADCs. Trigger lines reach the FPGA board with no manipulations.

#### 4.2.1. Analog signal path

##### Buffering signals

The input Op-Amp stage with 32 buffers will be utilized to read the 32 analog signals from the two SITH ASICs. Even though they could appear as simple components, a careful choice must be done owing to the selected clock frequency of the system, 50MHz, and conditions under worst-case scenario must be met (for instance, considering the minimum time to distinguish two events of 200ns in a single channel). It is decided to orderly read channels with the FPGA, one after the other, independently on the arrival order of the events, which means that the generic channel  $N$  is selected once every 8 clock cycles. Following the procedure of considering the worst-case scenario, a time constant of approximately 32ns is chosen, which forces selecting a gain bandwidth product (GBWP) larger than 5MHz and a stable closed-loop configuration with a unitary gain.

Another important parameter of the buffers to carefully check is the slew rate (SR). From simple calculations, it results that a component with SR larger than  $825 \frac{V}{\mu s}$  should be selected, avoiding to be the bottleneck of the buffer speed and to lose signal stability.

##### Selection of channels

The parameters of the multiplexers (MUXes) are easier to choose, even if the choice may be guided by the availability of components on the electronic market. For each ASIC, two

8-to-1 multiplexers will be used in parallel, arranging the system clock to work at 50MHz. It is worth mentioning that a single 16-to-1 MUX could be used, with the drawback of choosing a component with at least 80MHz of switch frequency, which is quite difficult to find on the market.

Two are the principal characteristics of a multiplexer. The first is the resistance, which should be the lowest possible to avoid changes in the differential Op-Amp impedance: such a variation would introduce an offset caused by the impedance mismatch. The bandwidth is the second important parameter. Selecting a work frequency of 50MHz, the MUX switches every 20ns, so that the transition time, defined as the time during which the output signal moves from 10% to 90% of its maximum amplitude, should be smaller than this time, which brings to a bandwidth of at least 50MHz.

## The differential Op-Amp

A differential Op-Amp is introduced to convert the single-ended signal at the output of the MUXes to a differential signal at the input of the ADC. To avoid the introduction of further delays to the incoming signal, a GBWP larger than the working frequency of the system, 50 MHz, is requested. Moreover, the sum of all delays from buffers to the ADC must be lower than 20ns since the transition time of the MUX is the most stringent factor.

A unitary gain and an offset of 1.65V is set in order to translate the 3.3 peak-to-peak voltage,  $V_{p-p}$ , from  $[0V, 3.3V]$  to  $[-1.65V, 1.65V]$ . Next to the Op-amp, there is a voltage partition to transform the  $3.3V_{p-p}$  into  $2V_{p-p}$  in such a way that the input dynamic range of the ADC will be respected. The circuit behavior is depicted in Figure 4.5. These voltage values represent a variation around the common-mode (CM) voltage.

The ADC is supplied from 0V to 3.3V and has an input dynamic range of two times the peak-to-peak voltage around the CM value of 1.5V, which means that the input ADC signal ranges from 0.5V to 2.5V. To generate such CM voltage with the differential amplifier, the input CM voltage is set to 2.475V, while the CM gain is set to one. Thus, the output CM voltage is 2.475V and it will be 1.5V as required by the ADC, after the voltage partition.

## Digital conversion

The chosen ADC as the best fit for the circuitry is reported in Ref. [18], i.e., the LTC2288 which is a 10-bit pipeline ADC. It consists of 5 pipeline stages with a latency of 5 clock cycles: data will be read at each clock cycle and, due to the pipeline structure, it may

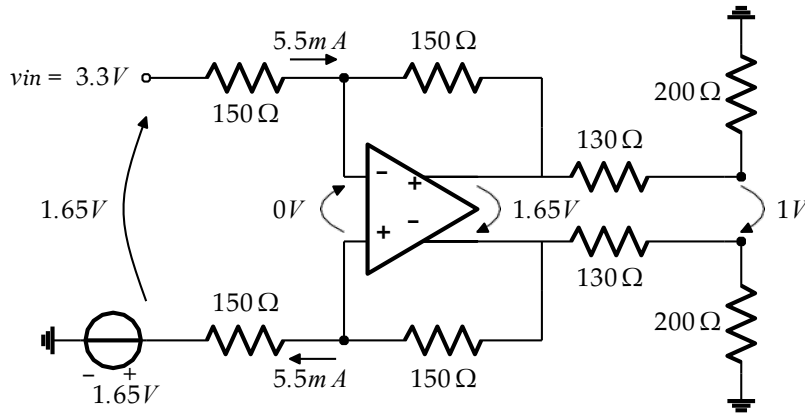


Figure 4.5: Schematic representation of the differential Op-Amp circuit analysis:  $V_{in}$  ranges from 0V to 3.3V and  $V_{out}$  ranges from -1V to 1V.

reach the desired throughput of  $50 \times 10^6$  samples per second, with both 10-bit resolution and clock frequency of 50MHz.

One disadvantage of ADCs with parallel output data lines is the huge number of pins that must be linked to the FPGA. Since 2 MUXes 8-to-1 are used for 16 channels, 2 ADCs should be used and 20 data lines will be present; for 32 channels, the number rises to 40. To reduce these number of lines, a possible solution could be exploiting serial output ADCs. However, both in single-ended and in low-voltage differential signaling, these components work at a very high throughput, which complicates the PCB and FPGA design.

The solution that will be effectively used lies in the nature of the LTC2288, which is a dual ADC, as its internal structure shows (Figure 4.6). Having a pin called "MUX" which allows multiplexing the input channels A and B to work in double data rate (DDR), the number of output data lines will be halved, enabling to use just 20 pins, for 32 channels, instead of 40.

## Sampling and holding signals

A sample and hold (S&H) stage is not reported in Figure 4.4, because it will not be useful for PGI-technique. However, the detection system described in this Chapter could be used in future applications where the sampling and holding of a signal may be essential (for instance, in pulse shape discrimination). Thus, in Figure 4.7 it is proposed a slight variation with respect to the previous block diagram, in which it is also implemented a sample and hold stage.

As one can see, the upper branch is just composed by a MUX stage, while the lower also contains a S&H stage. According to this concept, once the application of the detec-

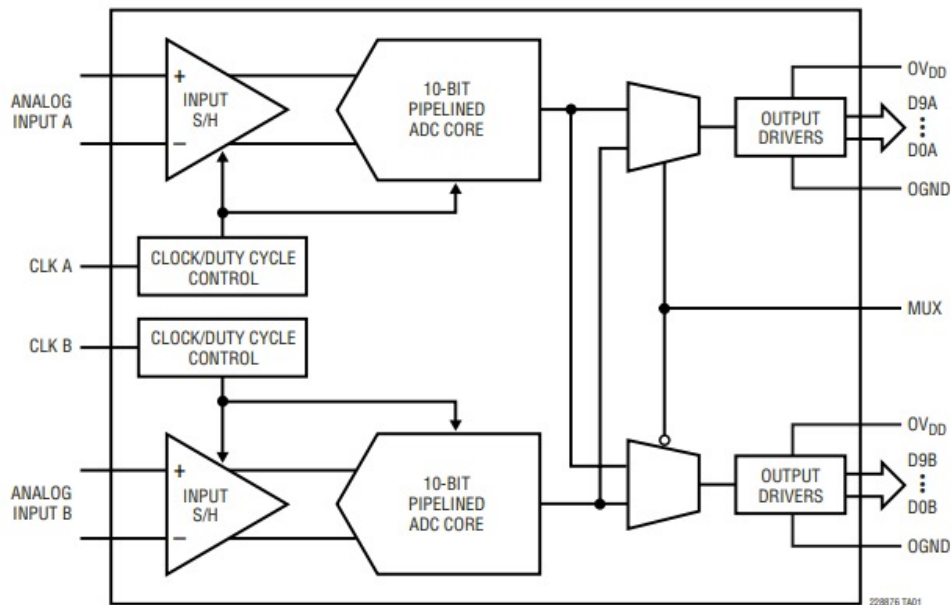


Figure 4.6: Schematic representation of the internal structure of the LTC2288CUP ADC. Being a dual differential 10-bit pipeline ADC, it can work in double data rate, halving the number of output data lines.

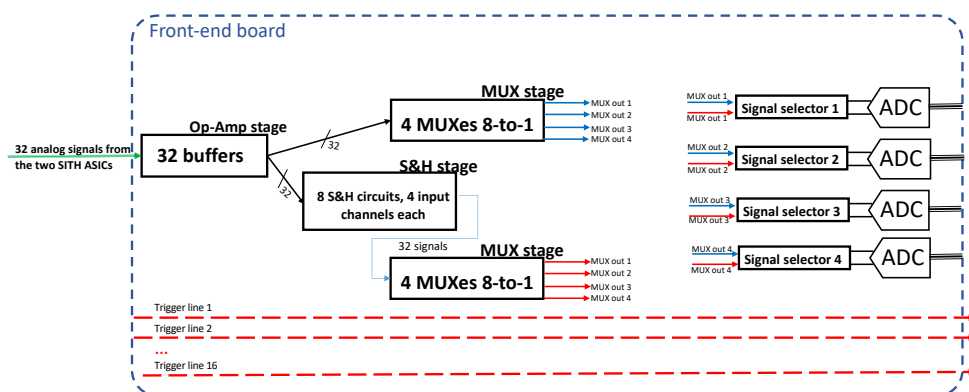


Figure 4.7: Schematic representation of the main blocks composing the FE PCB with the possibility to sample and hold signals: an Op-Amp stage, a MUX stage, a S&H stage, ADCs. The blue or the red signals will be chosen by means of specific switches (signal selectors), to select the preferred branch for the user application. Trigger lines reach the FPGA board with no manipulations.

tion system is fixed, the user will choose whether to utilize the four blue or red signals (Figure 4.7) coming the MUX stages of the two different branches. On the board, the signal selectors will be simple switches, allowing to select the preferred branch for the specific experimental campaign. For instance, in case of testing the PGI-technique for carbon ions, the S&H stage will not be required and so not used. Instead, considering the technique of pulse shape discrimination for which the sampling and subsequent holding of the signal is essential, the switch will select the branch comprising the S&H stage. About the choice of the sample and hold component, the main parameters should be accounted having in mind the numbers referred to the specific application. A first parameter to consider is the SR, which should be bigger than the rise edge of the analog signal coming from the chip. The user will have to find a compromise between performance and cost. As an example, let us consider an application in which the rising time,  $\tau$ , of the signal is of the order of  $1\mu s$ . This forces to look for a component with the following requirement on the SR (Eq. 4.1):

$$SR \geq \frac{\Delta V}{\tau} = \frac{3.3V}{1\mu s} = 3.3 \frac{V}{\mu s} \quad (4.1)$$

where  $\Delta V$  is the maximum voltage for the dynamic of the system (3.3V in the present set-up);  $\tau$  is the rising time of the detected signal.

Considering the present proposal of readout electronics with 32 channels, it would be rather difficult to place 32 S&H circuits in a compact board. Hence, it is necessary to search for a component which incorporates more S&Hs in just one circuitry. Searching on market, it is not simple to find circuits with more than one channel, with high slew rate (supposed larger than  $3.3 \frac{V}{\mu s}$ ).

Another important feature to consider is the bandwidth, BW, which should be of the order of (Eq. 4.2):

$$BW \approx \frac{1}{2\pi\tau} \quad (4.2)$$

where  $\tau$  is still the rising time of the detected signal.

Considering a rising time of  $1\mu s$ , a bandwidth of the order of 0.16MHz is needed, which does not constitute a problem in terms of availability on the market.

Considering the aforementioned values for SR and BW, which are typical for a detected signal in pulse shape discrimination of the secondary emission following carbon ion irradiation, the component SMP04ESZ could be a valid option [52].

### 4.2.2. Trigger lines

The SITH ASIC has also 16 trigger channels, which bring the information about the channel that is triggered, the time of triggering, and the gain value of the automatic gain control (AGC) inside the chip. As these signals do not need to be manipulated, they will simply be routed from the motherboard, through the front-end PCB, up to the FPGA where the control system will understand and decide which channel must be read. As already mentioned, traces' length of trigger lines must be very well matched to avoid the introduction of a big skew error.



# 5 | Conclusions and future developments

*In this conclusive Chapter, I will first summarize what was carried out in each Chapter. A final discussion on the results of the feasibility study will follow, in which I will illustrate the expected consequences.*

*In the last section, I will show what could be the future developments succeeding the present work. Starting from its limitations, I will propose further studies to continue and optimize the investigation of the PGI-technique in carbon ion radiation therapy.*

## 5.1. Conclusions

### 5.1.1. Summary

In Chapter 1, I discussed the importance and future role of particle therapy in fighting cancer. In particular, I showed its advantages over conventional radiation therapy from a physical, radiobiological standpoint. Also, the main disadvantages were faced, which are today limiting the spread of this technology as one of the leading weapons to tackle tumoral diseases.

One of the main drawbacks of hadrotherapy is the problem of range uncertainties, which restrict the beneficial effects of charged hadrons. This was the topic of Chapter 2, where I firstly described the sources of these uncertainties. Then, the solutions under investigation were treated in detail and I mainly focused on the PGI-technique, which was the range verification method selected for the simulation study present in this thesis.

After an exhaustive introduction, whose themes were really inspiring and helpful in the first months of the adventure that has brought to these words, the heart of the thesis was reported in Chapter 3. Here, I presented the first simulation study using the Monte Carlo code FLUKA to explore the feasibility of applying prompt gamma imaging with a knife-slit camera to carbon ion radiation therapy. I showed that, for a typical treatment energy of C-ions,  $150 \frac{MeV}{u}$ , a spot-by-spot range verification is unfeasible with the considered set-

up. However, combining the signal of various spots covering a single tumor layer, a fall-off precision of about 4mm can be theoretically retrieved.

In the nearly future, measurements will be planned to confirm the simulation results found in this work. For this, a proposal of the experimental set-up that will realize the simulation geometry was described in Chapter 4. An experimental validation of the theoretical findings would open the possibility of using PGI monitoring in CIRT on a layer-by-layer basis.

### 5.1.2. Final discussion on the obtained results

In recent years, there has been a substantial progress in the application of PGI mostly for what concern proton therapy. On the other hand, fewer studies have been made in the use of PGI verification for carbon ion radiation therapy. To solve this clear gap in knowledge, the expected objective of this work was to explore the PG fall-off retrieval capability with a well-established slit camera configuration, already tested clinically with proton irradiation.

Results on the PGI fall-off determination downstream C-ion irradiation were obtained using MC simulations with the FLUKA code, which is now considered a reliable tool for simulations in hadrontherapy, both for the prediction of dose delivery and PG emission. As stated in [5], the most recent FLUKA models for PG production showed a good reproduction of the relative shapes of experimental photon profiles as a function of depth as well as the absolute photon yield per primary C-ion, with an accuracy of about 15÷20%. MC simulations showed that, for the beam energy and the detection system of interest, the signal profile due to the secondary particles emitted from the delivery of a single spot to the phantom was correlated with the BP. Moreover, I demonstrated that the shape of the profile was clearly determined by the prompt-gamma signal over an almost uniform neutron background.

To probe the theoretical limitations of our gamma camera, a numerical experiment was reproduced for the measurement of the sensitivity in particle range retrieval. From 2mm shifts of the cylindrical target along its longitudinal axis, the signal curves were clearly distinguishable, opening the possibility to detect 2mm shifts of the BP with a sufficiently high number of incident ions. Indeed, in accordance with Krimmer *et al.* [64], I obtained that the accuracy of the system in range retrieval scales with the number of incident ions  $N_i$  as  $\sim 1/\sqrt{N_i}$ . However, the number of ions delivered in a single spot has proved to be too small for reaching that level of precision. From the trend-line of data fitting, it was found that at least around  $3 \times 10^8$  particles were needed to go below a 2mm accuracy with the present set-up (without considering additional factors that may reduce

the detection efficiency or additional sources of experimental error). This number was too high for a beam spot in a standard treatment with C-ions, so that this technique is not expected to be effective on a spot-by-spot basis, at least in the considered knife-edge camera configuration. Nonetheless,  $4 \times 10^8$  particles is, for instance, the maximum amount used in an irradiation spill at CNAO [13], delivered by their synchrotron to cover a given energy layer of the tumor volume. Thus, I proceeded to verify whether the distal position of the beam in an energy layer could be retrieved with a good accuracy. For this,  $5 \times 10^7$  ions were used, i.e., the average number of primary particles of a spill according to the interval found in Ref. [13]. Consequently, I combined the PGs signals obtained from 9 spots covering a  $2 \times 2 \text{ cm}^2$  area, assuming that the  $5 \times 10^7$  ions were divided equally among the selected spots. It was found that a 4mm accuracy is theoretically achievable with the present camera. Even with the introduction in the same layer of a  $\pm 4\text{mm}$  beam range variation by tilting the phantom, the accuracy was not worsened.

Although our results suggested that range verification on a spot-by-spot basis seems not to be feasible, it may be worth to further investigate the PGI technique in CIRT, at least on single spill basis. Even though a layer-by-layer approach in range verification is not strictly a real-time technique, it could still be useful to reduce the uncertainties during the treatment and for post-treatment verification. Differently, having in mind that the present results were dominated by the counting statistics, for the number of primary particles used in a single spot of FLASH therapy [128], there could be a chance to use real-time PGI during a FLASH therapy treatment. Finally, the conclusions drawn in the present work will be tested in a future experimental campaign, which is currently under organization.

## 5.2. Future developments

Following the present work, future developments may be found in the limitations of the feasibility study.

First, the simulations did not consider additional sources of neutron background, like the contribution of scattered neutrons from walls in the room. However, simulations performed including a 2m thick spherical concrete wall with a 4m inner radius did not show a significant loss of accuracy in range retrieval. Hence, the presence of the wall should not be considered as an essential aspect and can be neglected in future simulations.

Regarding the selected beam energy, a higher neutron background is expected for irradiation at higher ion energies, which could affect the capability to distinguish a PG fall-off. Therefore, forthcoming simulation studies will be necessary to explore the feasibility in the whole interval of therapeutic energies and, for the upper part of such interval, an

additional effort to adopt gamma-neutron discrimination techniques might be useful and decisive. This is the reason why in the design of the front-end PCB (Section 4.2) the S&H stage was implemented, and the pulse shape discrimination was often cited.

Concerning the detector signal, I did not include the coupling between the scintillator and the readout system, which may reduce the detection efficiency, for instance due to count rate limits. Moreover, a 4keV energy resolution was assumed for the detector, which is much better than the one of the real system, but having considered the events in an energy range of  $3 \div 7$  MeV, I do not expect this to play a critical role. Finally, in this work I have considered only a homogeneous phantom. Therefore, further simulations with inhomogeneities in the composition of the phantom should be carried out, in order to compare the results with the accuracy found in the homogeneous case. Regarding this topic, some ideas were elaborated for proton therapy, which could be inspiring for the same aim in CIRT [99] [42].

## Bibliography

- [1] K. Ando and Y. Kase. Biological characteristics of carbon-ion therapy. *International journal of radiation biology*, 85(9):715–728, 2009.
- [2] K. Ando, M. Yamaguchi, S. Yamamoto, T. Toshito, and N. Kawachi. Development of a low-energy x-ray camera for the imaging of secondary electron bremsstrahlung x-ray emitted during proton irradiation for range estimation. *Physics in Medicine & Biology*, 62(12):5006, 2017.
- [3] N. Bassler, J. Toftegaard, A. Lühr, B. S. Sørensen, E. Scifoni, M. Krämer, O. Jäkel, L. S. Mortensen, J. Overgaard, and J. B. B. Petersen. Let-painting increases tumour control probability in hypoxic tumours. *Acta Oncologica*, 53:25 – 32, 2014.
- [4] G. Battistoni, T. T. Boehlen, F. Cerutti, P. W. Chin, L. Esposito, A. Fasso, A. Ferrari, A. Mereghetti, P. G. Ortega, J. Ranft, S. Roesler, P. Sala, and V. Vlachoudis. Overview of the FLUKA code. In *ICS 2014*, 2014.
- [5] G. Battistoni, J. Bauer, T. T. Boehlen, F. Cerutti, M. P. Chin, R. Dos Santos Augusto, A. Ferrari, P. G. Ortega, W. Kozłowska, G. Magro, et al. The fluka code: an accurate simulation tool for particle therapy. *Frontiers in oncology*, 6:116, 2016.
- [6] M. G. Bisogni, A. Attili, G. Battistoni, N. Belcari, P. Cerello, S. Coli, A. Del Guerra, A. Ferrari, V. Ferrero, E. Fiorina, et al. Inside in-beam positron emission tomography system for particle range monitoring in hadrontherapy. *Journal of medical imaging*, 4(1):011005, 2016.
- [7] M. Blann. Preequilibrium decay. *Annual Review of Nuclear Science*, 25(1):123–166, 1975.
- [8] A. Bodek and J. Ritchie. Fermi-motion effects in deep-inelastic lepton scattering from nuclear targets. *Physical Review D*, 23(5):1070, 1981.
- [9] N. Bohr and J. A. Wheeler. The mechanism of nuclear fission. *Physical Review*, 56(5):426, 1939.

- [10] T. R. Bortfeld, M. F. de Viana, and S. Yan. The societal impact of ion beam therapy. *Zeitschrift fur medizinische Physik*, 31(2):102, 2021.
- [11] W. H. Bragg and R. Kleeman. Lxxiv. on the ionization curves of radium. *The London, Edinburgh, and Dublin Philosophical Magazine and Journal of Science*, 8(48):726–738, 1904.
- [12] A. Brahme. Recent advances in light ion radiation therapy. *International Journal of Radiation Oncology\* Biology\* Physics*, 58(2):603–616, 2004.
- [13] E. Bressi. Operation and patient treatments at cnao facility. *Energy*, 5(C6):O8.
- [14] L. Burigo, I. Pshenichnov, I. Mishustin, and M. Bleicher. Comparative study of dose distributions and cell survival fractions for 1h, 4he, 12c and 16o beams using geant4 and microdosimetric kinetic model. *Physics in Medicine & Biology*, 60(8):3313, 2015.
- [15] J. R. Castro. Results of heavy ion radiotherapy. *Radiation and environmental biophysics*, 34(1):45–48, 1995.
- [16] W. Chu, J. W. Staples, B. Ludewigt, T. Renner, R. Singh, M. Nyman, J. Collier, I. Daftari, P. Petti, J. Alonso, et al. Performance specifications for proton medical facility. Technical report, Lawrence Berkeley Lab., CA (United States), 1993.
- [17] S. E. Combs, O. Jäkel, T. Haberer, and J. Debus. Particle therapy at the heidelberg ion therapy center (hit)–integrated research-driven university-hospital-based radiation oncology service in heidelberg, germany. *Radiotherapy and Oncology*, 95(1):41–44, 2010.
- [18] L. T. Corporation. Dual 10-bit, 65/40/25msps low noise 3v adcs, note = <https://www.mouser.it/datasheet/2/609/228876fa-1271829.pdf>, cited 13-06-22 (pag. 24),.
- [19] R. Dal Bello, P. Magalhaes Martins, J. Graça, G. Hermann, T. Kihm, and J. Seco. Results from the experimental evaluation of cebr scintillators for he prompt gamma spectroscopy. *Medical physics*, 46(8):3615–3626, 2019.
- [20] R. Dal Bello, P. M. Martins, S. Brons, G. Hermann, T. Kihm, M. Seimetz, and J. Seco. Prompt gamma spectroscopy for absolute range verification of 12c ions at synchrotron-based facilities. *Physics in Medicine & Biology*, 65(9):095010, 2020.
- [21] A. Degiovanni and U. Amaldi. History of hadron therapy accelerators. *Physica medica*, 31(4):322–332, 2015.

- [22] E. Draeger, D. Mackin, S. Peterson, H. Chen, S. Avery, S. Beddar, and J. Polf. 3d prompt gamma imaging for proton beam range verification. *Physics in Medicine & Biology*, 63(3):035019, 2018.
- [23] M. Durante and H. Paganetti. Nuclear physics in particle therapy: a review. *Reports on Progress in Physics*, 79(9):096702, 2016.
- [24] M. Durante, R. Orecchia, and J. S. Loeffler. Charged-particle therapy in cancer: clinical uses and future perspectives. *Nature Reviews Clinical Oncology*, 14(8):483–495, 2017.
- [25] M. Durante, J. Debus, and J. S. Loeffler. Physics and biomedical challenges of cancer therapy with accelerated heavy ions. *Nature Reviews Physics*, 3(12):777–790, 2021.
- [26] W. Enghardt, P. Crespo, F. Fiedler, R. Hinz, K. Parodi, J. Pawelke, and F. Poenisch. Charged hadron tumour therapy monitoring by means of pet. *Nuclear Instruments and Methods in Physics Research Section A: Accelerators, Spectrometers, Detectors and Associated Equipment*, 525(1-2):284–288, 2004.
- [27] E. Fermi. Angular distribution of the pions produced in high energy nuclear collisions. *Physical Review*, 81(5):683, 1951.
- [28] A. Ferrari and P. R. Sala. The physics of high energy reactions. Technical report, CERN-ATL-PHYS-97-113, 1997.
- [29] V. Ferrero, E. Fiorina, M. Morrocchi, F. Pennazio, G. Baroni, G. Battistoni, N. Belcari, N. Camarlinghi, M. Ciocca, A. Del Guerra, et al. Online proton therapy monitoring: clinical test of a silicon-photodetector-based in-beam pet. *Scientific Reports*, 8(1):1–8, 2018.
- [30] F. Fiedler, D. Kunath, M. Priegnitz, and W. Enghardt. Online irradiation control by means of pet. In *Ion beam therapy*, pages 527–543. Springer, 2012.
- [31] J. Flanz. Accelerators for charged particle therapy. *Modern Physics Letters A*, 30(17):1540020, 2015.
- [32] M. Fontana, J.-L. Ley, D. Dauvergne, N. Freud, J. Krimmer, J. M. Létang, V. Maxim, M.-H. Richard, I. Rinaldi, and É. Testa. Monitoring ion beam therapy with a compton camera: Simulation studies of the clinical feasibility. *IEEE Transactions on Radiation and Plasma Medical Sciences*, 4(2):218–232, 2019.
- [33] R. Gartia, T. T. Singh, and T. B. Singh. Optically stimulated luminescence (osl) of lu<sub>2</sub>sio<sub>5</sub>: Ce powder: A preliminary study. *Nuclear Instruments and Methods in*

- Physics Research Section B: Beam Interactions with Materials and Atoms*, 269(1): 30–33, 2011.
- [34] M. F. Gensheimer, T. I. Yock, N. J. Liebsch, G. C. Sharp, H. Paganetti, N. Madan, P. E. Grant, and T. Bortfeld. In vivo proton beam range verification using spine mri changes. *International Journal of Radiation Oncology\* Biology\* Physics*, 78(1): 268–275, 2010.
- [35] S. Giordanengo, M. Donetti, F. Marchetto, A. Ansarinejad, A. Attili, F. Bourhaleb, F. Burini, R. Cirio, P. Fabbriatore, F. Voelker, et al. Performances of the scanning system for the cnao center of oncological hadron therapy. *Nuclear Instruments and Methods in Physics Research Section A: Accelerators, Spectrometers, Detectors and Associated Equipment*, 613(2):317–322, 2010.
- [36] M. L. Goldberger. The interaction of high energy neutrons and heavy nuclei. *Physical Review*, 74(10):1269, 1948.
- [37] C. Golnik, F. Hueso-González, A. Müller, P. Dendooven, W. Enghardt, F. Fiedler, T. Kormoll, K. Roemer, J. Petzoldt, A. Wagner, et al. Range assessment in particle therapy based on prompt  $\gamma$ -ray timing measurements. *Physics in Medicine & Biology*, 59(18):5399, 2014.
- [38] B. Gottschalk. Physics of proton interactions in matter. *Proton Therapy Physics*, pages 19–60, 2012.
- [39] J. J. Griffin. Statistical model of intermediate structure. *Physical review letters*, 17(9):478, 1966.
- [40] P. Henriquet, E. Testa, M. Chevallier, D. Dauvergne, G. Dedes, N. Freud, J. Krimmer, J. Létang, C. Ray, M. Richard, et al. Interaction vertex imaging (ivi) for carbon ion therapy monitoring: a feasibility study. *Physics in Medicine & Biology*, 57(14):4655, 2012.
- [41] Y. Hirano, S. Kinouchi, Y. Ikoma, E. Yoshida, H. Wakizaka, H. Ito, and T. Yamaya. Compartmental analysis of washout effect in rat brain: in-beam openpet measurement using a 11c beam. *Physics in Medicine & Biology*, 58(23):8281, 2013.
- [42] F. Hueso-González, M. Rabe, T. A. Ruggieri, T. Bortfeld, and J. M. Verburg. A full-scale clinical prototype for proton range verification using prompt gamma-ray spectroscopy. *Physics in Medicine & Biology*, 63(18):185019, 2018.
- [43] J. Hüfner, K. Schäfer, and B. Schürmann. Abrasion-ablation in reactions between relativistic heavy ions. *Physical Review C*, 12(6):1888, 1975.

- [44] D. Hymers, E. Kasanda, V. Bildstein, J. Easter, A. Richard, A. Spyrou, C. Höhr, and D. Mücher. Intra-and inter-fraction relative range verification in heavy-ion therapy using filtered interaction vertex imaging. *Physics in Medicine & Biology*, 66(24):245022, 2021.
- [45] IBA (Ion Beam Application). <https://iba-worldwide.com/>.
- [46] Y. Iseki, T. Kanai, M. Kanazawa, A. Kitagawa, H. Mizuno, T. Tomitani, M. Suda, and E. Urakabe. Range verification system using positron emitting beams for heavy-ion radiotherapy. *Physics in Medicine & Biology*, 49(14):3179, 2004.
- [47] M. L. Jensen, J. S. Nyemann, L. P. Muren, B. Julsgaard, P. Balling, and R. M. Turtos. Optically stimulated luminescence in state-of-the-art lyso: Ce scintillators enables high spatial resolution 3d dose imaging. *Scientific Reports*, 12(1):1–11, 2022.
- [48] Y. Jongen, M. Abs, A. Blondin, W. Kleeven, S. Zaremba, D. Vandeplassche, V. Alexandrov, S. Gursky, O. Karamyshev, G. Karamysheva, et al. Compact superconducting cyclotron c400 for hadron therapy. *Nuclear Instruments and Methods in Physics Research Section A: Accelerators, Spectrometers, Detectors and Associated Equipment*, 624(1):47–53, 2010.
- [49] T. Kamada. Twenty years of carbon ion radiation therapy at the national institute of radiological sciences: accomplishments and prospects. *International Journal of Particle Therapy*, 2(3):459–463, 2015.
- [50] T. Kamada, H. Tsujii, E. A. Blakely, J. Debus, W. De Neve, M. Durante, O. Jäkel, R. Mayer, R. Orecchia, R. Pötter, et al. Carbon ion radiotherapy in japan: an assessment of 20 years of clinical experience. *The Lancet Oncology*, 16(2):e93–e100, 2015.
- [51] M. Kanazawa, A. Kitagawa, S. Kouda, T. Nishio, M. Torikoshi, K. Noda, T. Murakami, M. Suda, T. Tomitani, T. Kanai, et al. Application of an ri-beam for cancer therapy: in-vivo verification of the ion-beam range by means of positron imaging. *Nuclear Physics A*, 701(1-4):244–252, 2002.
- [52] D. key electronics. Smp04esz, note = <https://www.digikey.it/it/products/detail/analog-devices-inc/smp04esz/820394>, cited 13-06-22,.
- [53] J.-W. Kim. Pinhole camera measurements of prompt gamma-rays for detection of beam range variation in proton therapy. *Journal of the Korean Physical Society*, 55(4):1673–1676, 2009.
- [54] G. Knoll. *Radiation Detection and Measurement*. 01 2000. ISBN 0-471-07338-5.

- [55] A. Knopf, K. Parodi, H. Paganetti, E. Cascio, A. Bonab, and T. Bortfeld. Quantitative assessment of the physical potential of proton beam range verification with pet/ct. *Physics in Medicine & Biology*, 53(15):4137, 2008.
- [56] A. Knopf, K. Parodi, T. Bortfeld, H. A. Shih, and H. Paganetti. Systematic analysis of biological and physical limitations of proton beam range verification with offline pet/ct scans. *Physics in Medicine & Biology*, 54(14):4477, 2009.
- [57] A.-C. Knopf and A. Lomax. In vivo proton range verification: a review. *Physics in Medicine & Biology*, 58(15):R131, 2013.
- [58] A. Koehler, R. Schneider, and J. Sisterson. Range modulators for protons and heavy ions. *Nuclear Instruments and Methods*, 131(3):437–440, 1975.
- [59] B. Kozlovsky, R. J. Murphy, and R. Ramaty. Nuclear deexcitation gamma-ray lines from accelerated particle interactions. *The Astrophysical Journal Supplement Series*, 141(2):523, 2002.
- [60] A. C. Kraan. Range verification methods in particle therapy: underlying physics and monte carlo modeling. *Frontiers in oncology*, 5:150, 2015.
- [61] G. Kraft. Radiotherapy with heavy ions: radiobiology, clinical indications and experience at gsi, darmstadt. *Tumori Journal*, 84(2):200–204, 1998.
- [62] M. Krämer, W. Weyrather, and M. Scholz. The increased biological effectiveness of heavy charged particles: from radiobiology to treatment planning. *Technology in cancer research & treatment*, 2(5):427–436, 2003.
- [63] S. C. Krejcarek, P. E. Grant, J. W. Henson, N. J. Tarbell, and T. I. Yock. Physiologic and radiographic evidence of the distal edge of the proton beam in craniospinal irradiation. *International Journal of Radiation Oncology\* Biology\* Physics*, 68(3): 646–649, 2007.
- [64] J. Krimmer, D. Dauvergne, J. Létang, and É. Testa. Prompt-gamma monitoring in hadrontherapy: A review. *Nuclear Instruments and Methods in Physics Research Section A: Accelerators, Spectrometers, Detectors and Associated Equipment*, 878: 58–73, 2018.
- [65] B. Larsson, L. Leksell, B. Rexed, P. Sourander, W. Mair, and B. Andersson. The high-energy proton beam as a neurosurgical tool. *Nature*, 182(4644):1222–1223, 1958.
- [66] A. A. Lazar, R. Schulte, B. Faddegon, E. A. Blakely, and M. Roach III. Clinical

- trials involving carbon-ion radiation therapy and the path forward. *Cancer*, 124 (23):4467–4476, 2018.
- [67] P. Lecoq, C. Morel, J. O. Prior, D. Visvikis, S. Gundacker, E. Auffray, P. Križan, R. M. Turtos, D. Thers, E. Charbon, et al. Roadmap toward the 10 ps time-of-flight pet challenge. *Physics in Medicine & Biology*, 65(21):21RM01, 2020.
- [68] Y.-S. Lin, T.-C. Chao, J.-H. Hong, and C.-J. Tung. Comparisons of longitudinal and lateral dose profiles and relative biological effectiveness for dna double strand breaks among 1h, 4he and 12c beams. *Radiation Physics and Chemistry*, 137:169–172, 2017.
- [69] J. S. Loeffler and M. Durante. Charged particle therapy—optimization, challenges and future directions. *Nature reviews Clinical oncology*, 10(7):411–424, 2013.
- [70] H.-M. Lu. A potential method for in vivo range verification in proton therapy treatment. *Physics in Medicine & Biology*, 53(5):1413, 2008.
- [71] W. Luo, Y. F. Ali, C. Liu, Y. Wang, C. Liu, X. Jin, G. Zhou, and N.-A. Liu. Particle therapy for breast cancer: Benefits and challenges. *Frontiers in Oncology*, page 1425, 2021.
- [72] P. Magalhaes Martins, R. Dal Bello, M. Seimetz, G. Hermann, T. Kihm, and J. Seco. A single-particle trigger for time-of-flight measurements in prompt-gamma imaging. *Frontiers in Physics*, 8:169, 2020.
- [73] A. Mairani, S. Mein, E. A. Blakely, J. Debus, M. Durante, A. Ferrari, H. Fuchs, D. Georg, D. R. Grosshans, F. Guan, et al. Roadmap: helium ion therapy. *Physics in Medicine & Biology*, 2022.
- [74] T. D. Malouff, A. Mahajan, S. Krishnan, C. Beltran, D. S. Seneviratne, and D. M. Trifiletti. Carbon ion therapy: a modern review of an emerging technology. *Frontiers in oncology*, page 82, 2020.
- [75] I. Mattei, F. Bini, F. Collamati, E. De Lucia, P. M. Frallicciardi, E. Iarocci, C. Mancini-Terracciano, M. Marafini, S. Muraro, R. Paramatti, et al. Secondary radiation measurements for particle therapy applications: prompt photons produced by 4he, 12c and 16o ion beams in a pmma target. *Physics in Medicine & Biology*, 62(4):1438, 2017.
- [76] C.-H. Min, C. H. Kim, M.-Y. Youn, and J.-W. Kim. Prompt gamma measurements for locating the dose falloff region in the proton therapy. *Applied physics letters*, 89 (18):183517, 2006.

- [77] C. H. Min, J. G. Park, and C. H. Kim. Development of an array-type prompt gamma detection system for the online measurement of the range of the proton beam in a patient: a monte carlo feasibility study. *Journal of the Korean Physical Society*, 52(3 PART 1):888–891, 2008.
- [78] C. H. Min, H. R. Lee, C. H. Kim, and S. B. Lee. Development of array-type prompt gamma measurement system for in vivo range verification in proton therapy. *Medical physics*, 39(4):2100–2107, 2012.
- [79] H. Mizuno, T. Tomitani, M. Kanazawa, A. Kitagawa, J. Pawelke, Y. Iseki, E. Urakabe, M. Suda, A. Kawano, R. Iritani, et al. Washout measurement of radioisotope implanted by radioactive beams in the rabbit. *Physics in Medicine & Biology*, 48(15):2269, 2003.
- [80] O. Mohamad, H. Makishima, and T. Kamada. Evolution of carbon ion radiotherapy at the national institute of radiological sciences in japan. *Cancers*, 10(3):66, 2018.
- [81] L. Nenoff, M. Priegnitz, G. Janssens, J. Petzoldt, P. Wohlfahrt, A. Trezza, J. Smeets, G. Pausch, and C. Richter. Sensitivity of a prompt-gamma slit-camera to detect range shifts for proton treatment verification. *Radiotherapy and Oncology*, 125(3):534–540, 2017.
- [82] W. G. Oldham, R. R. Samuelson, and P. Antognetti. Triggering phenomena in avalanche diodes. *IEEE Transactions on electron devices*, 19(9):1056–1060, 1972.
- [83] OncoRay: National Center for Radiation Research in Oncology Dresden. <http://doi.wiley.com/10.1002/mp.12670>.
- [84] R. Orecchia, S. Rossi, and P. Fossati. Indications of carbon ion therapy at cnao. In *AIP Conference Proceedings*, volume 1099, pages 399–404. American Institute of Physics, 2009.
- [85] N. Otte. The silicon photomultiplier—a new device for high energy physics, astroparticle physics, industrial and medical applications. In *Proceedings of the IX International Symposium on Detectors for Particle, Astroparticle and Synchrotron Radiation Experiments*, pages 1–9, 2006.
- [86] H. Owen, A. Lomax, and S. Jolly. Current and future accelerator technologies for charged particle therapy. *Nuclear Instruments and Methods in Physics Research Section A: Accelerators, Spectrometers, Detectors and Associated Equipment*, 809:96–104, 2016.

- [87] H. Paganetti. Significance and implementation of rbe variations in proton beam therapy. *Technology in cancer research & treatment*, 2(5):413–426, 2003.
- [88] H. Paganetti. Range uncertainties in proton therapy and the role of monte carlo simulations. *Physics in Medicine & Biology*, 57(11):R99, 2012.
- [89] Particle Therapy Co-Operative Group. Facilities under construction, . <https://www.ptcog.ch/index.php/facilities-under-construction>, cited 03-31-2022.
- [90] Particle Therapy Co-Operative Group. Facilities in operation, . <https://www.ptcog.ch/index.php/facilities-in-operation>, cited 03-31-2022.
- [91] G. Pausch, J. Petzoldt, M. Berthel, W. Enghardt, F. Fiedler, C. Golnik, F. Hueso-González, R. Lentering, K. Römer, K. Ruhnau, et al. Scintillator-based high-throughput fast timing spectroscopy for real-time range verification in particle therapy. *IEEE Transactions on Nuclear Science*, 63(2):664–672, 2016.
- [92] G. Pausch, J. Berthold, W. Enghardt, K. Römer, A. Straessner, A. Wagner, T. Werner, and T. Kögler. Detection systems for range monitoring in proton therapy: Needs and challenges. *Nuclear Instruments and Methods in Physics Research Section A: Accelerators, Spectrometers, Detectors and Associated Equipment*, 954:161227, 2020.
- [93] F. Pennazio, G. Battistoni, M. G. Bisogni, N. Camarlinghi, A. Ferrari, V. Ferrero, E. Fiorina, M. Morrocchi, P. Sala, G. Sportelli, et al. Carbon ions beam therapy monitoring with the inside in-beam pet. *Physics in Medicine & Biology*, 63(14):145018, 2018.
- [94] I. Perali, A. Celani, L. Bombelli, C. Fiorini, F. Camera, E. Clementel, S. Henrotin, G. Janssens, D. Prieels, F. Roellinghoff, et al. Prompt gamma imaging of proton pencil beams at clinical dose rate. *Physics in Medicine & Biology*, 59(19):5849, 2014.
- [95] J. Petzoldt, K. Roemer, W. Enghardt, F. Fiedler, C. Golnik, F. Hueso-Gonzalez, S. Helmbrecht, T. Kormoll, H. Rohling, J. Smeets, et al. Characterization of the microbunch time structure of proton pencil beams at a clinical treatment facility. *Physics in Medicine & Biology*, 61(6):2432, 2016.
- [96] M. Pinto, D. Dauvergne, N. Freud, J. Krimmer, J. M. Létang, C. Ray, F. Roellinghoff, and E. Testa. Design optimisation of a tof-based collimated camera prototype for online hadrontherapy monitoring. *Physics in Medicine & Biology*, 59(24):7653, 2014.

- [97] G. Poludniowski, N. Allinson, and P. Evans. Proton radiography and tomography with application to proton therapy. *The British journal of radiology*, 88(1053):20150134, 2015.
- [98] A. Pompos, M. Durante, and H. Choy. Heavy ions in cancer therapy. *JAMA oncology*, 2(12):1539–1540, 2016.
- [99] M. Priegnitz, S. Helmbrecht, G. Janssens, I. Perali, J. Smeets, F. Vander Stappen, E. Sterpin, and F. Fiedler. Measurement of prompt gamma profiles in inhomogeneous targets with a knife-edge slit camera during proton irradiation. *Physics in Medicine & Biology*, 60(12):4849, 2015.
- [100] T. Rackwitz and J. Debus. Clinical applications of proton and carbon ion therapy. In *Seminars in oncology*, volume 46, pages 226–232. Elsevier, 2019.
- [101] M. Raju. Particle radiotherapy: historical developments and current status. *Radiation research*, 145(4):391–407, 1996.
- [102] C. Richter, G. Pausch, S. Barczyk, M. Priegnitz, I. Keitz, J. Thiele, J. Smeets, F. Vander Stappen, L. Bombelli, C. Fiorini, et al. First clinical application of a prompt gamma based in vivo proton range verification system. *Radiotherapy and Oncology*, 118(2):232–237, 2016.
- [103] F. Roellinghoff, A. Benilov, D. Dauvergne, G. Dedes, N. Freud, G. Janssens, J. Krimmer, J. M. Létang, M. Pinto, D. Priels, et al. Real-time proton beam range monitoring by means of prompt-gamma detection with a collimated camera. *Physics in Medicine & Biology*, 59(5):1327, 2014.
- [104] S. Rossi. The status of cnao. *The European Physical Journal Plus*, 126(8):1–39, 2011.
- [105] Saint-Gobain. Lyso scintillation crystal - cerium doped lutetium. <https://www.crystals.saint-gobain.com/radiation-detection-scintillators/crystal-scintillators/lyso-scintillation-crystals,>.
- [106] D. Schardt, I. Schall, H. Geissel, H. Irnich, G. Kraft, A. Magel, M. Mohar, G. Münzenberg, F. Nickel, C. Scheidenberger, et al. Nuclear fragmentation of high-energy heavy-ion beams in water. *Advances in Space Research*, 17(2):87–94, 1996.
- [107] U. Schneider, E. Pedroni, and A. Lomax. The calibration of ct hounsfield units for radiotherapy treatment planning. *Physics in Medicine & Biology*, 41(1):111, 1996.
- [108] E. Scifoni, W. Tinganelli, W. Weyrather, M. Durante, A. Maier, and M. Krämer.

- Including oxygen enhancement ratio in ion beam treatment planning: model implementation and experimental verification. *Physics in Medicine & Biology*, 58(11):3871, 2013.
- [109] E. Scifoni, W. Tinganelli, W. K. Weyrather, M. Durante, A. Maier, and M. Krämer. Including oxygen enhancement ratio in ion beam treatment planning: model implementation and experimental verification. *Physics in medicine and biology*, 58 11:3871–95, 2013.
- [110] K. S. Seo, C. H. Kim, and J. W. Kim. Comparison of titanium hydride ( $\text{TiH}_2$ ) and paraffin as neutron moderator material in a prompt gamma scanning system. *JOURNAL-KOREAN PHYSICAL SOCIETY*, 48(4):855, 2006.
- [111] J. Smeets. *Prompt gamma imaging with a slit camera for real time range control in particle therapy*. PhD thesis, Université Libre de Bruxelles, 2012.
- [112] J. Smeets, F. Roellinghoff, D. Prieels, F. Stichelbaut, A. Benilov, C. Fiorini, R. Peloso, M. Basilavecchia, T. Frizzi, J. Dehaes, et al. Prompt gamma imaging with a slit camera for real-time range control in proton therapy. *Physics in Medicine & Biology*, 57(11):3371, 2012.
- [113] A. R. Smith. Proton therapy. *Physics in Medicine & Biology*, 51(13):R491, 2006.
- [114] P. Solevi, E. Munoz, C. Solaz, M. Trovato, P. Dendooven, J. E. Gillam, C. Lacasta, J. F. Oliver, M. Rafecas, I. Torres-Espallardo, et al. Performance of macaco compton telescope for ion-beam therapy monitoring: first test with proton beams. *Physics in Medicine & Biology*, 61(14):5149, 2016.
- [115] F. Stichelbaut and Y. Jongen. Verification of the proton beam position in the patient by the detection of prompt gamma-rays emission. In *39th Meeting of the Particle Therapy Co-Operative Group*, volume 16, 2003.
- [116] S. Tang, S. Both, H. Bentefour, J. J. Paly, Z. Tochner, J. Efstathiou, and H.-M. Lu. Improvement of prostate treatment by anterior proton fields. *International Journal of Radiation Oncology\* Biology\* Physics*, 83(1):408–418, 2012.
- [117] T. Tessonier, A. Mairani, S. Brons, T. Haberer, J. Debus, and K. Parodi. Experimental dosimetric comparison of  $^1\text{H}$ ,  $^4\text{He}$ ,  $^{12}\text{C}$  and  $^{16}\text{O}$  scanned ion beams. *Physics in Medicine & Biology*, 62(10):3958, 2017.
- [118] E. Testa, M. Bajard, M. Chevallier, D. Dauvergne, F. Le Foulher, N. Freud, J.-M. Létang, J.-C. Poizat, C. Ray, and M. Testa. Monitoring the bragg peak location of

- 73 mev/ u carbon ions by means of prompt  $\gamma$ -ray measurements. *Applied physics letters*, 93(9):093506, 2008.
- [119] M. Testa, M. Bajard, M. Chevallier, D. Dauvergne, N. Freud, P. Henriquet, S. Karkar, F. Le Foulher, J. Letang, R. Plescak, et al. Real-time monitoring of the bragg-peak position in ion therapy by means of single photon detection. *Radiation and environmental biophysics*, 49(3):337–343, 2010.
- [120] P. Thirolf, C. Lang, S. Aldawood, H. vd Kolff, L. Maier, D. Schaart, and K. Parodi. Development of a compton camera for online range monitoring of laser-accelerated proton beams via prompt-gamma detection. In *EPJ Web of Conferences*, volume 66, page 11036. EDP Sciences, 2014.
- [121] F. Tommasino, E. Scifoni, and M. Durante. New ions for therapy. *International journal of particle therapy*, 2(3):428–438, 2015.
- [122] H. Tsujii and T. Kamada. A review of update clinical results of carbon ion radiotherapy. *Japanese journal of clinical oncology*, 42(8):670–685, 2012.
- [123] H. Tsujii, T. Kamada, T. Shirai, K. Noda, H. Tsuji, and K. Karasawa. Carbon-ion radiotherapy. *Carbon-ion radiotherapy*. Springer, 2014.
- [124] M. Van Goethem, R. Van Der Meer, H. Reist, and J. Schippers. Geant4 simulations of proton beam transport through a carbon or beryllium degrader and following a beam line. *Physics in Medicine & Biology*, 54(19):5831, 2009.
- [125] J. M. Verburg and J. Seco. Proton range verification through prompt gamma-ray spectroscopy. *Physics in Medicine & Biology*, 59(23):7089, 2014.
- [126] J. M. Verburg, H. A. Shih, and J. Seco. Simulation of prompt gamma-ray emission during proton radiotherapy. *Physics in Medicine & Biology*, 57(17):5459, 2012.
- [127] J. M. Verburg, K. Riley, T. Bortfeld, and J. Seco. Energy-and time-resolved detection of prompt gamma-rays for proton range verification. *Physics in Medicine & Biology*, 58(20):L37, 2013.
- [128] U. A. Weber, E. Scifoni, and M. Durante. Flash radiotherapy with carbon ion beams. *Medical Physics*, 49(3):1974–1992, 2022.
- [129] V. Weisskopf and D. Ewing. On the yield of nuclear reactions with heavy elements. *Physical Review*, 57(6):472, 1940.
- [130] T. Werner, J. Berthold, F. Hueso-González, T. Koegler, J. Petzoldt, K. Roemer, C. Richter, A. Rinscheid, A. Straessner, W. Enghardt, et al. Processing of prompt

- gamma-ray timing data for proton range measurements at a clinical beam delivery. *Physics in Medicine & Biology*, 64(10):105023, 2019.
- [131] R. R. Wilson. Radiological use of fast protons. *Radiology*, 47(5):487–491, 1946.
- [132] A. J. Wojtowicz, W. Drozdowski, D. Wisniewski, J.-L. Lefaucheur, Z. Galazka, Z. Gou, T. Lukasiewicz, and J. Kisielewski. Scintillation properties of selected oxide monocrystals activated with ce and pr. *Optical Materials*, 28(1-2):85–93, 2006.
- [133] A. Wrońska and D. Dauvergne. Range verification by means of prompt-gamma detection in particle therapy 1. In *Radiation Detection Systems*, pages 139–160. CRC Press, 2021.
- [134] XGLab - X and Gamma Ray Electronics. <https://www.xglab.it/>.
- [135] Y. Xie, E. H. Bentefour, G. Janssens, J. Smeets, F. Vander Stappen, L. Hotoiu, L. Yin, D. Dolney, S. Avery, F. O’Grady, et al. Prompt gamma imaging for in vivo range verification of pencil beam scanning proton therapy. *International Journal of Radiation Oncology\* Biology\* Physics*, 99(1):210–218, 2017.
- [136] M. Yamaguchi, Y. Nagao, K. Ando, S. Yamamoto, M. Sakai, R. K. Parajuli, K. Arakawa, and N. Kawachi. Imaging of monochromatic beams by measuring secondary electron bremsstrahlung for carbon-ion therapy using a pinhole x-ray camera. *Physics in Medicine & Biology*, 63(4):045016, 2018.
- [137] M. Yang, G. Virshup, J. Clayton, X. Zhu, R. Mohan, and L. Dong. Does kv–mv dual-energy computed tomography have an advantage in determining proton stopping power ratios in patients? *Physics in Medicine & Biology*, 56(14):4499, 2011.
- [138] J. Yap, A. De Franco, and S. Sheehy. Future developments in charged particle therapy: Improving beam delivery for efficiency and efficacy. *Frontiers in Oncology*, page 5159, 2021.
- [139] C. Ying, D. Bolst, A. Rosenfeld, and S. Guatelli. Characterization of the mixed radiation field produced by carbon and oxygen ion beams of therapeutic energy: A monte carlo simulation study. *Journal of medical physics*, 44(4):263, 2019.
- [140] M. Zarifi, S. Guatelli, Y. Qi, D. Bolst, D. Prokopovich, and A. Rosenfeld. Characterization of prompt gamma ray emission for in vivo range verification in particle therapy: A simulation study. *Physica Medica*, 62:20–32, 2019.

- [141] J. F. Ziegler and J. P. Biersack. The stopping and range of ions in matter. In *Treatise on heavy-ion science*, pages 93–129. Springer, 1985.

## List of Figures

- |     |   |    |
|-----|---|----|
| 1.1 | (a) Estimated number of new cases in 2020, worldwide, both sexes, all ages.; (b) Estimated number of deaths in 2020, worldwide, both sexes, all ages. . . . .   | 3  |
| 1.2 | Statistics of patients treated in particle therapy facilities worldwide: in 2020, around 250.000 patients were treated with protons and close to 40000 with C-ions. . . . .   | 9  |
| 1.3 | Schematic illustration of a charged particle therapy facility with isocentric gantry. The gantry consists of a number of dipole and quadrupole magnets that all rotate around the patient; in this example the magnets that scan the spots across the treatment field are located downstream of the final dipole, which is often but not always what is implemented. Figure from Ref. [86]. . . . .   | 13 |
| 1.4 | Illustration of the operation of a classical cyclotron. The generated dipole field $B$ is static, and within it the protons are gradually accelerated (after injection from an ion source) within the vacuum vessel due to the alternating voltage applied across the gap between the dees, which may be as much as 100 kV per turn or more. . . . .  | 15 |
| 1.5 | The CNAO horizontal beam line setup. The beam is deflected by horizontal and vertical scanning magnets to reach the desired spatial coordinates. Downstream the magnets, a set of monitor chambers are used to measure the beam fluence and position. Figure from Ref. [35]. . . . .  | 17 |
| 1.6 | Schematic representation of spot, raster and continuous line scanning patterns for PBS delivery. Spots and solid lines indicate beam-on irradiation and dashed lines indicate movement with beam-off. For spot scanning, the beam is turned off between movement to the next spot but remains on for the whole delivery in raster scanning. For continuous line scanning, the dose is delivered across a linear path (rather than as spots) and may be turned off between movement to subsequent lines. Figure from Ref. [138]. . | 18 |

1.7 Beam current trend over time for a clinical treatment. A spill last about 1s and covers energy layer with a certain number of spots. The time to change energy in a synchrotron is about 2s. On the right, the time structure of a proton beam spill is represented, and the figure was taken from Ref. [13] . 19

1.8 **a)** Depth-dose distributions showing the Bragg peak for different ions. The X-ray depth-dose curve is calculated for a 21MeV linac, while the energies of the ions correspond approximately to the same range: 148MeV for protons,  $170\frac{MeV}{u}$  for  $^3\text{He}$ -ions and  $270\frac{MeV}{u}$  for  $^{12}\text{C}$ -ions. **b)** Lateral broadening (full-width-at-half-maximum of the Gaussian distribution) for the same ions. The widening of the beam should be compared with typical entrance spot sizes of proton and ion beams of  $\sim 5 \div 10$  mm. Figure from Ref. [25]. 20

1.9 Stopping power, S, in  $\frac{MeVcm^2}{g}$ , for protons in water as function of kinetic energy. The total, electronic, and nuclear stopping power are shown, as well as the characteristic regions. Figure from Ref. [60]. . . . . 22

1.10 Schematic display of stages in a nucleon-nucleus interaction relevant for radiotherapy, together with time scale and energy of interacting particle. Figure from Ref. [60]. . . . . 29

1.11 Top: sketch of a possible nucleon-nucleus reaction in proton therapy, whereby a neutron is created. Bottom: sketch of nucleus-nucleus reaction in heavy ion therapy, with creation of light fragments. Figure from Ref. [60]. . . . . 30

1.12 Relative probability of the three major types of gamma-ray interaction in matter as function of the impinging photon energy and the target atomic number. Figure from Ref. [54]. . . . . 35

1.13 Band gap diagram for LYSO:Ce. (a) illustrates the scintillation process: Ionizing radiation generates electrons and holes, which are subsequently trapped by  $\text{Ce}^{3+}$  centers with a life time of  $\sim 40\text{ns}$  and give rise to prompt light emission. (b) A fraction of electrons are stored in auxiliary OSL traps, which are readout on request through the same  $\text{Ce}^{3+}$  centers using optical stimulation. Solid lines illustrate excitations, dashed lines illustrate capture processes, dash-dotted lines illustrate radiative decays and wavy lines illustrate optical photons. . . . . 37

1.14 Simplified schematic representation of a silicon photomultiplier circuit. Each micro-cell consists of a SPAD, quench resistor and fast output capacitor. . . . . 39

1.15 The SiPM output signal saturation for three different numbers of micro-cells, namely 576, 1024 and 4096. The number of fired micro-cells is proportional to the number of impinging photons when this is well below the total number of cells; when this is not the case, saturation of the output signal shows up. Figure from Ref. [85]. . . . . 41

2.1 Safety margins used in different clinical proton therapy facilities: (3.5% + 3mm) at Loma Linda University Medical Center (LLUMC), (3.5% + 2mm) at Universitats Protonen Therapie Dresden (UPTD), (3.5% + 1mm) at Massachusetts General Hospital (MGH) and (2.5% + 1.5mm) at University of Florida Health Proton Therapy Institute (UFH). The term "range bonus" refers to the margin applied to the specified range to ensure maximum tumor coverage even in the case of an undershoot. Under certain treatment scenarios, these centers may use larger margins. . . . . 46

2.2 Schematic view of an *in-vivo* range verification with diode detectors (yellow dots) for a patient whose prostate (red delineation) is treated by an anterior proton field (yellow arrows) with an endorectal balloon (white curve). Figure from Ref. [116]. . . . . 50

2.3 Gamma production cross sections from proton reactions with  $^{12}\text{C}$  (a) and  $^{16}\text{O}$  (b). Cross sections are drawn in the same color when they use the same data multiplied by different factors. For  $^{12}\text{C}$ , the 4.438MeV and 4.444MeV peaks are merged as the 4.44MeV peak. Figure from Ref. [111]. . . . . 51

2.4 (a) Emission vertices of secondaries with energies larger than 1MeV emerging from a water target (cylinder with 15cm diameter, 40cm length) irradiated by a 160MeV proton beam; (b) emission vertices of secondaries with energies larger than 1MeV emerging from a water target (cylinder with 15cm diameter, 40cm length) irradiated by  $310 \frac{\text{MeV}}{u}$  carbon ion beam. Figures from Ref. [64]. . . . . 56

2.5 A particle beam of given initial energy irradiates a target and, consequently, a PG-ray is emitted along the beam track at position  $x_p$ . The time  $t_p$  has elapsed from the entrance of particle into the target up to the gamma emission, which is assumed to be instantaneous. The PG-ray time of flight,  $t_{\gamma TOF}$ , is necessary for the radiation to reach the detector, which is situated outside of the target and measures the whole time difference between the time of the particle entering the target and the arrival time of the PG-ray at the detector. The measured distribution is denoted as PG-ray timing (PGT) spectrum. Figure from Ref. [37] . . . . . 61

2.6	An example of a passive collimated system for PG detection is depicted. The collimation hole gives the name to this particular set up, which is mounted on a moving system. Figure from Ref. [76] . . . . .	63
2.7	The slit camera's conceptual design: a slit collimation produces a 1D projection of PG emissions along the beam path on a pixelated scintillation detector. Figure from Ref. [94] . . . . .	64
2.8	Scheme of the array of collimated scintillators to detect PG rays emitted from a water target after proton irradiation. Figure from Ref. [77]. . . . .	65
2.9	PG profiles acquired with a multi-slit camera and fitted with a sigmoidal curve for 80, 150, and 220 MeV proton beams. The measured proton dose distributions are shown for comparison. Figure from Ref. [78]. . . . .	66
3.1	Representation of the simulation geometry for the investigation of the secondary emission from a tissue-equivalent target. The target was cut in 16 slices, 7 of which were 3cm-thick while the remaining ones 1cm-thick (around the Bragg peak). The room hosting the target was air-filled and the walls were made of Portland cement. . . . .	72
3.2	Graphical representation of the scoring features for the investigation of secondary emission. Only photons and neutrons emitted within 85° and 90° with respect to the beam axis were scored. . . . .	73
3.3	The depth-dose distributions, determined by the FLUKA estimator "USRBIN", are here reported. In particular, one can distinguish: <b>A)</b> curves from all the beams in a single plot for a direct comparison; <b>B)</b> 200 $\frac{MeV}{u}$ proton curve; <b>C)</b> 200 $\frac{MeV}{u}$ He-ion curve; <b>D)</b> 385 $\frac{MeV}{u}$ C-ion curve. . . . .	74
3.4	From preliminary manipulations, the secondary particle counts per primary following C-ion irradiation are summed for each slice from the 8 <sup>th</sup> to the 16 <sup>th</sup> . The photon (black) and neutron (blue) profiles are reported over the depth-dose curve. . . . .	75
3.5	Double differential photon spectra in energy and solid angle, plotted against the energy. The secondary emissions from the 9 <sup>th</sup> slice to the 12 <sup>th</sup> are reported for the three different beams. . . . .	76
3.6	Double differential photon spectra in energy and solid angle, plotted against the energy. The secondary emissions from the 13 <sup>th</sup> slice to the 16 <sup>th</sup> are reported for the three different beams. . . . .	76
3.7	Lethargic double differential neutron spectra in energy and solid angle, plotted against the energy. The secondary emissions from the 9 <sup>th</sup> slice to the 12 <sup>th</sup> are reported for the three different beams. . . . .	77

3.8	Lethargic double differential neutron spectra in energy and solid angle, plotted against the energy. The secondary emissions from the 13 <sup>th</sup> slice to the 16 <sup>th</sup> are reported for the three different beams. . . . .	77
3.9	Schematic representation of the simulation geometry employed in this work: (a) 2D representation on the xz-plane; the depicted position of the phantom is labelled as the "no-shift" position; (b) 3D representation. . . . .	80
3.10	Illustration of the irradiation spots (red) selected for the second set of simulations. The spots have the same z-coordinate, and cover an $2 \times 2 \text{ cm}^2$ area on the xy-plane inside the soft-tissue phantom (yellow). The pitch between the spots is 1cm. . . . .	83
3.11	Simulation geometry of the third set of simulations: the target was inclined by a $22^\circ$ angle with respect to the z-axis, so that the spots of Figure 3.10 have a different z-coordinate. This considers the variations of the beam range in a patient for the different selected spots, even with the beam at constant energy. . . . .	84
3.12	Graphical representation of the generated noisy curves for different phantom shifts and numbers of C-ions: <b>A)</b> $10^6$ , <b>B)</b> $10^7$ , <b>C)</b> $10^8$ , <b>D)</b> $10^{10}$ . . . . .	85
3.13	Graphical explanation of Method 1: the signal curve (blue) obtained by MC simulations is shifted up to 1cm, in 0.02cm steps, on the forward (green) and backward (purple) direction of the z-axis. The shifted curves are then compared with the investigated noisy curve, and the best match is found by a minimization of the RMSE. . . . .	86
3.14	Graphical explanation of the Method 2: a generic noisy curve (yellow) is interpolated in the expected fall-off region (purple line), which is then crossed by the y-coordinate of the reference curve inflection point (blue line). The difference between the x-coordinates of the crossing point (green line) and of the inflection point is chosen as the error in the fall-off estimation. . . . .	87
3.15	Graphical explanation of Method 3: the algorithm finds the x-coordinate (pink) corresponding to the interception between a generic noisy curve (yellow) and the y-coordinate (blue) of the inflection point of the reference curve (red). The error in the fall-off estimation was defined as the distance between the x-coordinates of the interception and of the reference curve inflection point. . . . .	88

3.16	Graphical representation of the correlation between the PG detection profile and the Bragg peak profile (orange), obtained with FLUKA simulations for the phantom in the "no-shift" position: (a) Total detection profile (blue); (b) Photon contribution to the detection profile (black) and neutron contribution to the detection profile (blue). . . . .	89
3.17	Range shift sensitivity: ideal signal curves obtained by MC simulations for various shifts of the phantom along the z-axis. . . . .	90
3.18	Results of Method 1. The frequency distributions pertaining to the various shift of the phantom are presented for different numbers of C-ions: <b>A)</b> $10^6$ ; <b>B)</b> $10^7$ ; <b>C)</b> $10^8$ ; <b>D)</b> $10^{10}$ . . . . .	91
3.19	Results of Method 2. The frequency distributions pertaining to the various shift of the phantom are presented for different numbers of C-ions: <b>A)</b> $10^6$ ; <b>B)</b> $10^7$ ; <b>C)</b> $10^8$ ; <b>D)</b> $10^{10}$ . Unlike for Method 1, the centroids of the Gaussian curves shift together with the phantom position. . . . .	91
3.20	Range retrieval precision (blue) obtained by Method 1 plotted against the number of incident C-ions on a log-log scale. The precision is averaged over the shifts of the phantom. The linear interpolation (red) has a slope of about $-1/2$ . . . . .	93
3.21	Graphical results of simulations for the nine selected spots (see Figure 3.10). The signal is varied only by a shift in the x-direction. . . . .	94
3.22	Peak normalization of detection profiles presented in Figure 3.21. . . . .	95
3.23	Results from range retrieval precision analysis. The Gaussian distributions are found applying the aforementioned methods, whose precision is resumed in the legend. . . . .	95
3.24	Signal curves obtained with FLUKA for the nine selected spots, in the case of the tilted target. . . . .	96
3.25	Results from range retrieval precision analysis in the case of the tilted phantom. The Gaussian distributions are found applying the aforementioned methods, whose precision is resumed in the legend. . . . .	97
4.1	Schematic drawing of a single detection module of $4 \times 4$ SiPMs followed by a readout ASIC. A gamma-ray, interacting with a LYSO crystal, produces visible photons which are collected by the represented tile of SiPM. Beyond the readout ASIC, the signal reaches the data acquisition system which quantitatively takes track of photon interactions. . . . .	100

- 4.2 Architecture of the readout electronics, including the motherboard with two ASICs and a micro-controller for gain stabilization, a front-end PCB with a dedicated MUX stage and ADCs; the inter-connection board puts in contact the front-end board with the FPGA-based DAQ and a PC reached by a USB 3.0 connection. . . . . 101
- 4.3 Schematic representation of the SITH ASIC. In each of the 16 channels, a current conveyor drives the current into two separated branches: the first is composed by a baseline holder (BLH) and an integration filter to produce the energy output; the other possesses a trigger and a gain encoder to output a timing signal. . . . . 102
- 4.4 Schematic representation of the main blocks composing the FE PCB: an Op-Amp stage to buffer the analog signals, a MUX stage to select each of them which are then converted into digital singals by the ADCs. Trigger lines reach the FPGA board with no manipulations. . . . . 104
- 4.5 Schematic representation of the differential Op-Amp circuit analysis:  $V_{in}$  ranges from 0V to 3.3V and  $V_{out}$  ranges from -1V to 1V. . . . . 106
- 4.6 Schematic representation of the internal structure of the LTC2288CUP ADC. Being a dual differential 10-bit pipeline ADC, it can work in double data rate, halving the number of output data lines. . . . . 107
- 4.7 Schematic representation of the main blocks composing the FE PCB with the possibility to sample and hold signals: an Op-Amp stage, a MUX stage, a S&H stage, ADCs. The blue or the red signals will be chosen by means of specific switches (signal selectors), to select the preferred branch for the user application. Trigger lines reach the FPGA board with no manipulations. 107



## List of Tables

2.1	Estimated proton range uncertainties and their sources and the potential of Monte Carlo for reducing the uncertainty. The estimations are average numbers based on 1.5 standard deviations. Extreme cases, such as lung treatments, might show bigger uncertainties. . . . .	46
2.2	Partial cross sections $\sigma$ of the reactions of proton and carbon ion beams with the most abundant nuclei of human tissue. From Ref. [111]. . . . .	54
3.1	Composition and density of the materials assigned in FLUKA to the various regions of the simulation volume. Percentages in the compositions refer to atomic percentage. . . . .	82
3.2	$2\sigma$ of the Gaussian frequency distributions resulting from the data analysis of the first set of simulations. Results are reported in mm, for the various numbers of C-ions: <b>A)</b> $10^6$ ; <b>B)</b> $10^7$ ; <b>C)</b> $10^8$ ; <b>D)</b> $10^{10}$ . . . . .	92
3.3	Linear trend-line fitting parameters of the retrieved precision for all the three methods and different amount of C-ions. . . . .	93



# Acknowledgements

Thanks.

